Summer 2010

Fluid Budget of Metasedimentary Rocks from a Tertiary Accretionary Prism and Connections to Seismicity, Olympic Peninsula, Northwest Washington State

Holly Makena MacFadden Rotman
Central Washington University

Recommended Citation

Rotman, Holly Makena MacFadden, "Fluid Budget of Metasedimentary Rocks from a Tertiary Accretionary Prism and Connections to Seismicity, Olympic Peninsula, Northwest Washington State" (2010). *All Master's Theses*. 1460.
https://digitalcommons.cwu.edu/etd/1460

FLUID BUDGET OF METASEDIMENTARY ROCKS FROM A TERTIARY ACCRETIONARY PRISM AND CONNECTIONS TO SEISMICITY, OLYMPIC PENINSULA, NORTHWEST WASHINGTON STATE

A Thesis
Presented to
The Graduate Faculty
Central Washington University

In Partial Fulfillment
of the Requirements for the Degree
Master of Science
Geology

---

by
Holly Makana MacFadden Rotman
July 2010

CENTRAL WASHINGTON UNIVERSITY

Graduate Studies

We hereby approve the thesis of

Holly Makana MacFadden Rotman

Candidate for the degree of Master of Science

APPROVED FOR THE GRADUATE FACULTY

______________ ______________________________
Dr. Chris Mattinson, Committee Chair

______________ ______________________________
Dr. Carey Gazis

______________ ______________________________
Dr. Tim Melbourne

______________ ______________________________
Dr. Audrey Huerta

______________ ______________________________
Dean of Graduate Studies

ABSTRACT

FLUID BUDGET OF METASEDIMENTARY ROCKS FROM A TERTIARY ACCRETIONARY PRISM AND CONNECTIONS TO SEISMICITY, OLYMPIC PENINSULA, NORTHWEST WASHINGTON STATE

by

Holly Makana MacFadden Rotman

July 2010

Metamorphic dehydration reactions and fluid movement in accretionary prisms have been linked to the recently discovered episodic tremor and slip (ETS) earthquake events along subduction zones, but prior studies lack the detail to effectively test the hypothesis that fluid flow triggers ETS events. I conducted field work along a 52.5 km transect on the Olympic Peninsula metasedimentary accretionary prism of the Cascadia subduction zone, and collected approximately 40 representative samples of sandstone and mudrock that were buried to 6–15 km. This depth range intersects the 10–50 km depth range of ETS events. My objectives are to quantify the water flow recorded in rocks of the Olympic Peninsula via petrographic, whole rock, and isotopic analyses to test the prediction that water release increases at ~10 km depth, creating fluid overpressure needed to trigger seismicity.

I calculated that on the Olympic Peninsula 1 km^3 of 50% sandstone and 50% mudrock loses ~10^5 kg H_2O/yr during burial from 6–14 km depth, comparable to the values expected from large-scale fluid budget models. Quartz veins that compose

0.5–1% of the Obstruction Peak site (~14 km burial depth) are important records of fluid flow quantity and origin. $\delta^{18}O$ values of +11.8‰ to +15.2‰ indicate that vein H_2O originated from metamorphic reactions. Flow recorded by 1 km^3 of rock containing 0.5–1% quartz veins is $>10^6$ kg H_2O/yr, comparable to the values 2×10^7 to 2×10^8 kg H_2O/yr modeled at compositionally similar subduction zones to produce fluid overpressure conditions. I observed fibrous quartz veins, which also indicate fluid overpressure conditions were reached and support my H_2O flow estimates. Therefore, Olympic Peninsula rocks at depths of ~10–14 km record dehydration and fluid overpressure large enough to trigger subduction zone seismicity.

ACKNOWLEDGMENTS

Thank goodness the Geology Club held a Faculty Appreciation Day this year; otherwise these acknowledgments might be longer than my thesis text. I still owe many, many thanks to many people. My primary advisor, Dr. Chris Mattinson, has for the past two years walked me patiently through how scientific research works, and has taught me many invaluable lessons about research and writing. I am indebted to Dr. Carey Gazis not only for her input on the stable isotope component of this project but for helping me get through the stressful times of graduate school. Of course I am also grateful to Dr. Tim Melbourne for his interest in a project on the Olympic Peninsula, and to Dr. Charlie Rubin for saying 'You may hate this idea, but….' as I was searching for a project my first weeks here at Central. Dr. Audrey Huerta's input has always been invaluable for going to the core of the matter in such a way that I take constructive criticism well. Dr. Marie Ferland (among many invaluable deeds) helped me get started on understanding accretionary prisms, a subject about which I knew very little when I began this project. I think I still owe Nick Zentner a beer for his assistance. As I was editing my thesis this spring, Brad Pitcher posted hundreds of pictures from the Italy research group's fieldwork, which served as a very welcome break from the editing fishbowl.

I also want to thank Dr. Jeff Lee for the opportunity to take a course in field mapping in California last year, during which I learned and reviewed many necessary field skills. Many thanks also to Dr. Wendy Bohrson for permitting me to go on the Hawaii trip this year; as a graduate student, I felt especially fortunate to be included in what is normally an undergraduate experience. I saw some wonderful geology on both trips and broke up the home-office-class routine, which I would otherwise likely persist in indefinitely with no break instead of taking a break and coming back with a new perspective!

Abbreviated honorable mentions (hoping to keep this to two pages) go to my fellow grads: Emily, Maureen, Clay, Travis, Michelle, Tom, Pat, Mack, Sarah, Caitlin, Tina, Matt, Chris, Aaron, Rachel, Ben, Zoe^2, Katie, Tabitha, Rodger, & Jim; the Hawaii crew: Chris, Becky, Greg, Brittany, Jessica, Angela, Amara, Jake, Kayla, Mike, Jim, Sarah, & Seth; and lots of undergrads in the Geology Club: Rosa, Anna, Eliya, Levi, Brienn, the Lady Den, Clarissa, Laura, and everyone whose names escape me!

I am also grateful to Jocelyn, Linda, and Craig for their respective assistance and patience with my various questions. The staff of Graduate Studies has been very helpful as well. I would also like to thank the Geological Society of America, Puget Sound Energy, and the Faculty Development & Research Committee for financial support, the faculty and staff at Washington State University Geology for their assistance with analyses, and R.W. Tabor for the loan of ~90 of his thin sections.

To all the faculty I haven't thanked specifically here: thank you. You have made a difference to me, and you have helped make my two years here at Central unforgettable, educational, and inspiring. Thanks to all of you I have figured out, and decided, a lot of things here that are not directly connected to my thesis, but have influenced my progress and where I plan to go after this. I will miss all of you.

Last but not least: I wish to thank my parents, who after their visit to Ellensburg understand why their girl went so far away to study geology!

TABLE OF CONTENTS

TABLE OF CONTENTS (continued)

Chapter Page

LIST OF TABLES

LIST OF TABLES (continued)

LIST OF FIGURES

LIST OF FIGURES (continued)

CHAPTER I

INTRODUCTION

Experimental, modeling, and observational studies show that fluid release and movement from diverse sources in rocks contributes to seismicity (e.g., White, 1976; Miller et al., 1999). Subduction zones are associated with large volumes of fluid and diverse seismicity, from episodic tremor and slip (ETS) events, detectable only by instruments, to the largest earthquakes in the world. Experimental and observational evidence indicates sedimentary accretionary prism rocks experience dehydration reactions throughout the subduction process (Vrolijk, 1987, 1990; Sample et al., 1993; Jarrard, 2003; Rowe & Screaton, 2009). Furthermore, seismologic and petrologic evidence suggest fluids released by metamorphic dehydration reactions play an important role in subduction zone seismicity (Hacker et al., 2003b; Shelly et al., 2006) including fluid imaged as a velocity anomaly within the 10–50 km depths of the recently discovered ETS process (Rogers & Dragert, 2003; Kao et al., 2005; Shelly et al., 2006). Fluid released at depths <50 km in the subduction zone will preferentially flow updip toward lower final pressure, ideally the Earth's surface. As it flows updip, the fluid passes through sedimentary accretionary prism rocks and causes high fluid pressure because of relatively slow fluid flow rates and because of permeability contrasts between lithologies (Hyndman et al., 1993; Saffer & Bekins, 1998). Veins formed by high fluid pressures (Vrolijk, 1987; Davis & Hyndman, 1989; Hyndman et al., 1993) in exhumed sedimentary accretionary prism rocks can record H_2O flow volume in the subduction zone. Because burial depth of exhumed sedimentary accretionary prisms commonly increase with distance landward from the trench (Tabor & Cady, 1978a; Sisson & Hollister, 1988; Breeding & Ague, 2002), an across-strike transect can record metamorphic dehydration reactions and extent of dehydration with depth. The fluids released during dehydration can contribute to seismicity (e.g., Hacker et al., 2003b) and/or vein formation (Vrolijk, 1987). Cascadia's Olympic Peninsula (Fig. 1) exposes metasedimentary accretionary prism rocks exhumed from depths of 6–15 km (Snavely & Kvenvolden, 1989; Brandon et al., 1998), overlapping with the depth constraints (10–50 km) of ETS (Kao et al., 2005). Thus, the fluid flow potentially responsible for ETS is likely to have been recorded in the Olympic Peninsula metasedimentary accretionary prism rocks.

Episodic tremor and slip events and megathrust earthquakes (discussed in Chapter II) are both well-documented in the Cascadia subduction zone (Atwater, 1987; Satake et al., 1996; Rogers & Dragert, 2003; Chapman & Melbourne, 2009) and ETS events are thought to increase stress on the subduction zone segment responsible for large megathrust earthquakes (Rogers & Dragert, 2003). Modern analogues to a Cascadia subduction zone megathrust quake include the 2004 Sumatra $M_w = 9.3$ event that caused >250 000 deaths. The last great Cascadia subduction zone quake was in 1700 (Satake et al., 1996), and the recurrence interval of these megathrust earthquakes is 300–500 years (Atwater & Hemphill-Haley, 1997). A similar event now would cause widespread devastation in the Pacific Northwest metropolitan areas and the crucial I-5 transportation corridor from the ground shaking alone. Given the destructive potential of the Cascadia

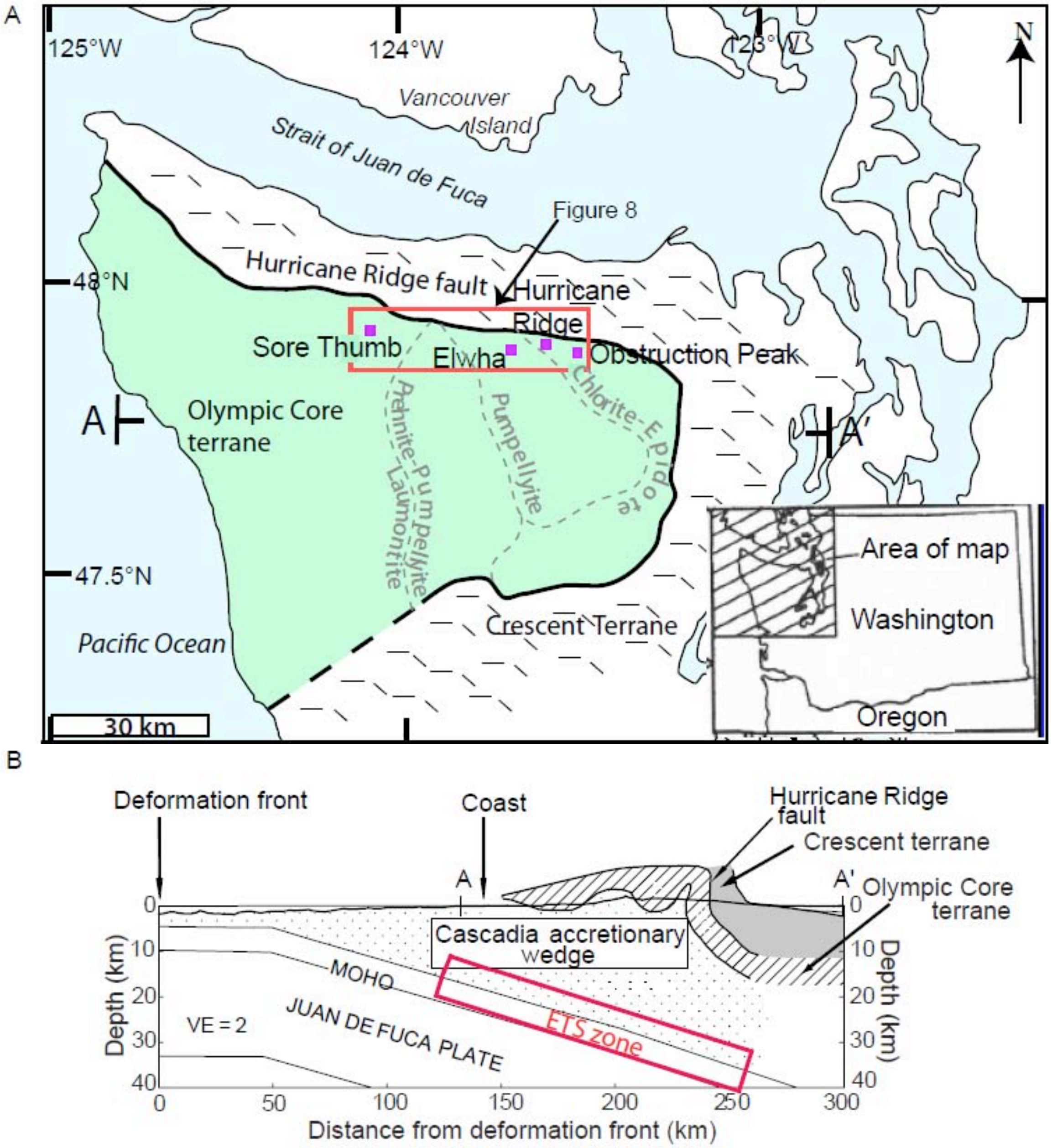

Figure 1. Overview of Olympic Peninsula and primary sample locations. (A) Map view of Olympic Peninsula. Metasedimentary rocks of my study area are green and labeled Olympic core terrane; Crescent terrane is patterned. Red box is area of Figure 8. Base map modified from Hirsch and Babcock (2009); isograds after Tabor and Cady (1978a). (B) Cross section of A-A'. ETS zone is indicated in the box. Major features of Olympic Peninsula are shown. Modified from Brandon et al. (1998).

subduction zone, it is important to fully understand the role of fluids in subduction zone seismicity. However, the connection between H_2O and ETS events is a minimally investigated aspect of subduction zone hazards.

Current models of subduction zone fluid budgets are focused on determining the volume and bulk fluid composition reaching mantle depths (e.g., Jarrard, 2003). These current models give a total flux from ~0–50 km depth, but do not specify the amount of dehydration as a function of depth within the 10–50 km depths (e.g., Kao et al., 2005) relevant to ETS events. Observations and analysis of modern sedimentary accretionary prisms confirm expulsion of relatively fresh H_2O that may originate from shallow depths (<2 km) to ≥14 km depths (Speed, 1990; Sample et al., 1993; Orange et al., 1997). These studies leave a spatial and temporal gap in our knowledge of fluid in subduction zones.

Therefore, an investigation to quantify the extent of metamorphic dehydration, possible rate of dehydration, and rate and volume of fluid flow at depths intersecting the 10-km upper boundary of the ETS zone is necessary to examine connections between H_2O and ETS events. Burial depth of exposed Olympic Peninsula rocks increases from 6 km in the west, to 15 km in the east (Tabor & Cady, 1978a; Snavely & Kvenvolden, 1989; Brandon et al., 1998). Therefore, I based my study sampling scheme on an east-west transect in the northern Olympic Peninsula (Fig. 1) to document dehydration and fluid flow, as explained above. The maximum burial depth at my sites is within the modern updip limit of ETS events, so my study transect also tests whether dehydration increases at 10 km depth and therefore can contribute fluid that can cause ETS seismicity. I use field observations, petrography, whole rock geochemistry, and oxygen isotope analysis to find evidence of dehydration and high volume fluid flow in metasedimentary rocks of the Olympic Peninsula.

CHAPTER II

BACKGROUND

Olympic Peninsula Geology

The exhumed rocks of the Olympic Peninsula are a combination of basaltic oceanic crust and offshore turbidite sequences. Most workers divide the rocks into two main categories (Fig. 1): the Crescent or Coast Range terrane, consisting of basalt and overlying marine sedimentary rocks, and the Olympic core or Olympic subduction complex, composed of metasedimentary accretionary prism rocks (Tabor & Cady, 1978a; Brandon & Calderwood, 1990; Brandon et al., 1998). The rocks have undergone low-grade regional metamorphism at zeolite facies in the western Olympic Peninsula core rocks to epidote zone in the eastern Olympic Peninsula core rocks and blueschist facies metamorphism in the basalt of the Crescent terrane (Tabor & Cady, 1978a; Brandon & Calderwood, 1990; Babcock et al., 1992). The Crescent basalt is dated at 48–59 Ma (Babcock et al., 1992), and the overlying sedimentary rocks, known as the Peripheral sequence, are contiguous with Crescent basalt (e.g., Tabor & Cady, 1978a). On the Olympic Peninsula, and particularly adjacent to my study area, the Crescent terrane has been steeply tilted to near vertical (Tabor & Cady, 1978a, b; Brandon et al., 1998). The Crescent and Olympic core are separated by the Hurricane Ridge fault, a thrust-sense fault that has sedimentary units on both sides in parts of my field area.

The metasedimentary accretionary prism rocks of the Olympic core, deposited 25–35 Ma, are predominantly sandstone and mudrock with minor basalt and conglomerate (Tabor et al., 1972; Tabor & Cady, 1978a; Brandon et al., 1998). Tabor and Cady (1978a) observed that metamorphic grade increases from west to east, and divided the core into five lithologic units based on field and petrographic observations. Four of the units are included in my study, and the fifth, Hoh lithic assemblage, is west of my study transect. The four relevant assemblages are briefly described in Table 1.

TABLE 1. SUMMARY OF GEOLOGIC UNITS

Unit*	Rock types	Other features
Needles-Gray Wolf	~30-50% sandstone ~50-70% siltstone & slate	Pumpellyite and epidote-chlorite zone Sandstone commonly micaceous or calcareous, fine to medium grained, thin to very thick bedded Metamorphic minerals: calcite, sericite, chlorite, leucoxene, albite, local epidote Units grade laterally and vertically
Grand Valley	~50% (foliated) sandstone & semischist ~50% siltstone, slate, & minor phyllite	Epidote-chlorite zone (in study area) Sandstone commonly micaceous or calcareous, fine to medium grained, thin to very thick bedded but may be thick bedded with slate interbeds Volcanic lithics common Local silty marble
Elwha	~30-50% sandstone ~50-70% slate & phyllite	Prehnite-pumpellyite zone Sandstone thick-bedded, may be micaceous Slate & phyllite more dominant in north Slate & phyllite contain graphite, plagioclase, sericite, chlorite, quartz
Western Olympic	~60-80% sandstone ~20-40% siltstone & argillite	Laumontite (zeolite mineral) zone Sandstone medium to thick bedded, graded, may be micaceous and locally calcareous Argillite/sandstone rhythmites Zeolite veins

*From Tabor and Cady (1978a).

Sandstone is ~50% of the Olympic core and siltstone and mudrocks compose the remaining 50% (Tabor & Cady, 1978a). Units in the west (Elwha, Western Olympic) are more thickly bedded and less micaceous than units in the east (Needles-Gray Wolf, Grand Valley). Metamorphic recrystallization varies widely, with no increase or other pattern in abundance from west to east (Tabor & Cady, 1978a). The units all show evidence of shearing, folding, and faulting (Tabor & Cady, 1978a, b).

The pressure and temperature conditions of the Olympic core metasedimentary accretionary prism rocks are not well constrained. Snavely and Kvenvolden (1989) determined via vitrinite reflectance that the western Olympic Peninsula (zeolite facies metamorphism) was buried to ~6 km and reached a temperature of ~135°C; zeolite facies rocks (west of laumontite isograd in Figure 1) are approximately 35% of the exposed metasedimentary accretionary prism. In the remainder of the Olympic Peninsula, paleotemperature gradient reconstructions based on zircon and apatite fission track studies established that maximum temperature and pressure was ~290°C and ~5 kbar, or 15 km depth (Brandon & Calderwood, 1990; Brandon & Vance, 1992; Brandon et al., 1998). Although Tabor and Cady (1978a, b) suggested burial depth on the Olympic Peninsula increases from west to east as evidenced by progression through chlorite-epidote zone metamorphism, Brandon and others (Brandon et al., 1998; Stewart & Brandon, 2004) contend the area of deepest burial, at 15 km depth, is in the geographic center of the Olympic Peninsula. Based on my observations (see Chapters IV, V), the observations of Tabor and Cady (1978a, b) are more representative of my study transect.

The erosional exhumation in Figure 2 suggested by Brandon et al. (1998) does not represent the burial depths from west to east observed in my study transect.

Modern Cascadia Subduction Zone

The current configuration of the Cascadia subduction zone with a convergence rate of ~40 mm/yr initiated ~12–17 Ma, when regional tectonic forces caused a seaward-concave bend in the trench, widening the sedimentary accretionary prism at the bend and causing uplift of the Olympic Mountains due to the shallower dip of the Juan de Fuca plate (Wilson, 1988; Brandon & Calderwood, 1990; Gutscher et al., 2001). Up to 30 km of sedimentary accretionary prism rocks are thought to underlie the present exposure on the Olympic Peninsula (Fig. 1B; Brandon et al., 1998). The modern offshore prism is

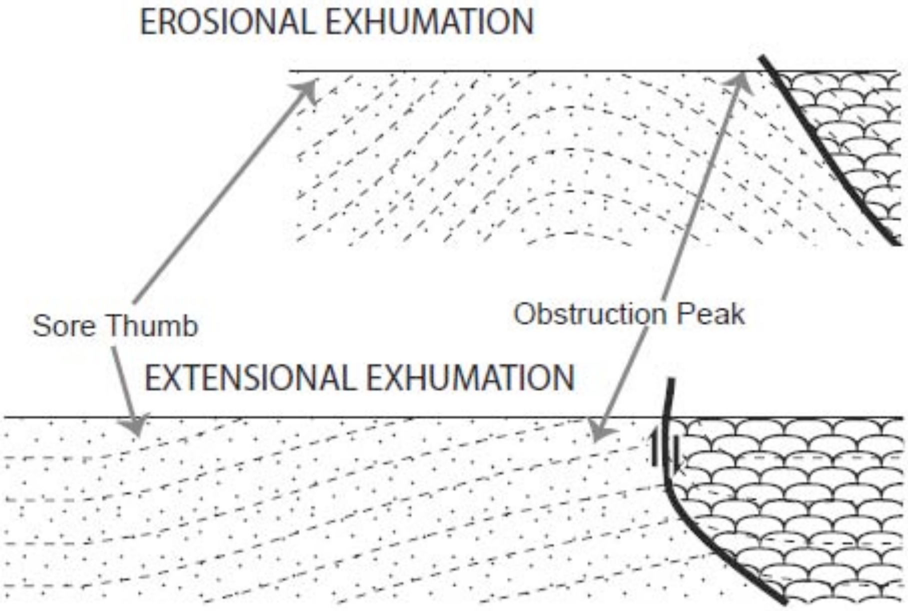

Figure 2. Two theorized exhumation scenarios for the Olympic Peninsula. Cross section is approximately A-A' of Figure 1. Erosional exhumation fits the fission track data of Brandon et al. (1998), while extensional exhumation fits the observations of Tabor and Cady (1978a). My study is based on the observations applicable to extensional exhumation being correct. Modified from Brandon et al. (1998).

1.5–3.5 km thick ~40 kilometers landward of the trench (Hyndman et al., 1993; Sample et al., 1993; Plank & Langmuir, 1998; Jarrard et al., 2003) in part due to extensive sediment deposition via the Columbia River and Strait of Juan de Fuca (Orange et al., 1997). The composition of the modern sedimentary accretionary prism is mostly turbidite sequences and pelagic mud in equal proportions (Normark & Reid, 2003), similar to rocks in the exhumed Olympic core (Hawkins, 1967; Tabor et al., 1972; Tabor & Cady, 1978a, b).

The Cascadia Megathrust

Subduction zone megathrust behavior changes with depth as temperature increases and rocks exhibit a transition from brittle to ductile behavior with increasing depth. At shallow levels in the subduction zone, where rocks primarily exhibit brittle behavior, the Cascadia megathrust is locked (labeled on the subducting Juan de Fuca plate in Figure 3) and is accumulating strain (Rogers & Dragert, 2003; Shelly et al., 2006; Schwartz & Rokosky, 2007; Moore et al., 2007). The locked section is at ~5–20 km depth at temperatures of ~150–300°C, although the subduction megathrust behavior is mostly ductile by 20 km depth and 300°C (Moore et al., 2007). At intermediate depths, the creeping segment of the megathrust moves slowly along weak zones (labeled as ‘transition’ on the subducting Juan de Fuca plate in Figure 3) while temporarily locked sections develop at asperities (see below; Schwartz & Rokosky, 2007). The strain is released during great earthquakes of $M_w \sim 9$ that cause coastal subsidence, tsunamis, and destruction over a large land area (Atwater, 1987; Satake et al., 1996).

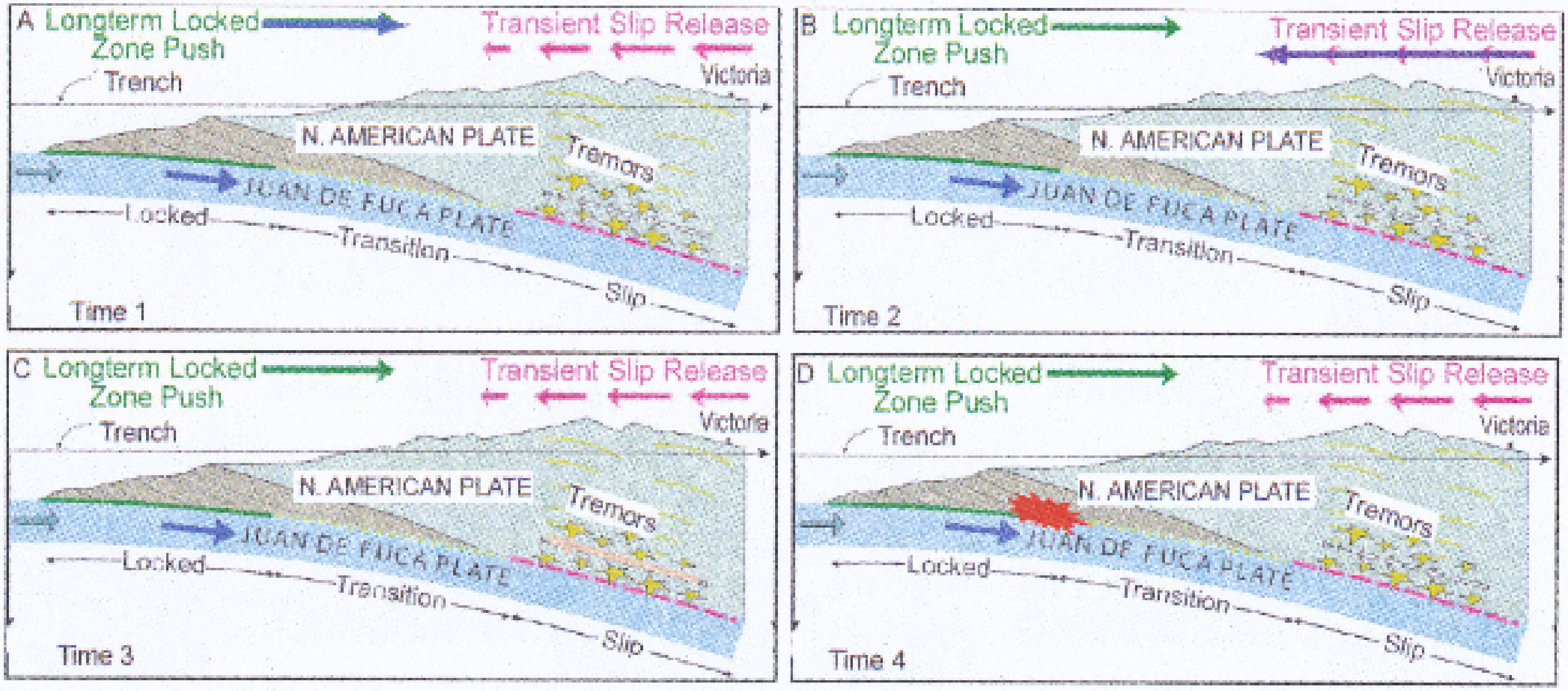

Figure 3. Time progression effect of ETS and progression of fault behavior with depth. (A) Long term landward push of subduction zone, indicated by blue arrow. (B) Short term seaward movement due to ETS event, represented by purple arrow. Land movement during ETS events is measurable by GPS. (C) Seaward land movement is connected to updip push (peach arrow) of both plates, an action that stresses the updip subduction megathrust. Repeated ETS event cycles continue to stress the subduction megathrust until (D) a subduction megathrust earthquake occurs. Modified from Geological Survey of Canada.

Based on prior work there is a possibility the Olympic Peninsula rocks were exhumed from megathrust depths. As noted above, the temperatures estimated for Olympic Peninsula rocks are 135–290°C (Snavely & Kvenvolden, 1989; Brandon et al., 1998), and this range correlates well with the 150–350°C range at which megathrust earthquakes occur (Moore et al., 2007). Furthermore, recent work on Kodiak Island, Alaska, found rocks thought to have recorded megathrust earthquakes at 12–14 km depth and 230–260°C (Rowe et al., 2009; Meneghini et al., 2010). I will return to additional lines of evidence supporting this possibility in greater detail in Chapters IV and V.

Episodic Tremor and Slip

An ETS event consists of tremor generated from depths of 10–50 km (Kao et al., 2005) and the seaward movement (mm scale) of the overriding plate (North America henceforth), an occurrence that takes days to weeks (Rogers & Dragert, 2003; Schwartz & Rokosky, 2007; Chapman & Melbourne, 2009). The westernmost edge of the North American plate is slowly moving landward (east) due to the 'push' of the locked interface with the oceanic Juan de Fuca plate (Fig. 3A), that is subducting to the east relative to a fixed interior North American plate. When an ETS event occurs, it releases the energy of a $M_w \sim 6.5$ earthquake over days to weeks (Fig. 4) in a manner only detectable on instruments (e.g., Chapman & Melbourne, 2009). During an ETS event, the North American plate above the creeping intermediate depth section of the subduction megathrust moves west (Fig. 3B, C) relative to a fixed interior North American plate, but the North American plate at the locked section of the megathrust continues to move east

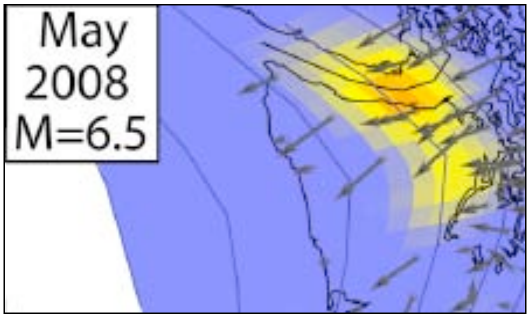

Figure 4. ETS event of May 2008. Yellow and orange indicates relative intensity of tremor with orange being greater intensity and arrows represent land movement recorded by GPS stations. After Chapman and Melbourne (2009).

with the Juan de Fuca plate, against the overall North American plate motion. This causes stress to increase on the locked updip section of the subduction megathrust (Rogers & Dragert, 2003). Earthquakes release stress, so a buildup of stress on the subduction megathrust increase the likelihood of a subduction megathrust earthquake (Fig. 3D; Rogers & Dragert, 2003; Kao et al., 2005; Schwartz & Rokosky, 2007). The exact cause of ETS events is unknown, but many hypotheses involve fluid: channelized fluid movement, decrease of shear stress in the presence of fluid, or serpentinization reactions (Bostock et al., 2002; Shelly et al., 2006).

Fluid Movement

Fluid release and movement in rocks is an important aspect of rock behavior, particularly in subduction zones where fluid may weaken rock and contribute to great earthquakes. Fluids moving through sedimentary accretionary prisms at shallow depths are primarily sourced from pore space compaction. At greater depths within the sedimentary accretionary prism, fluids are produced by metamorphic dehydration reactions in oceanic crust or within the sedimentary accretionary prism. Fluid flow is important because sufficient fluid quantity can lead to fluid overpressure (e.g., Fisher & Brantley, 1992), which weakens rocks and contributes to seismicity. Quartz veins can record the quantity of fluid that passes through the sedimentary accretionary prism rock.

Fluid from Shallow Depths in the Sedimentary Accretionary Prism

Pervasive and channelized fluid movement on the scale of m to km is widely documented in sedimentary accretionary prism toes and surfaces (Fig. 5). Sediments <10 m from the surface are commonly ~50% H_2O (Moore & Vrolijk, 1992; Sample et al., 1993; Schacht et al., 2008), and these fluids may be rapidly expelled from channelized seeps at the sedimentary accretionary prism toe (Sample et al., 1993); the fluid is commonly relatively fresh by comparison to seawater (Sample et al., 1993; Orange et al., 1997). Smaller seeps of fresh, pervasively flowing fluid landward of the deformation front are also common (e.g., Moore & Vrolijk, 1992). The high rate and volume of fluid expulsion via pervasive and channelized flow occurs primarily because 90% of sediment pore space is closed by 5 km depth, and horizontal compression via thrust faulting forces out pore space within 20 km of the sedimentary accretionary prism deformation front (Hyndman et al., 1993; Gutscher et al., 2001). Much of the fluid expelled from sedimentary accretionary prisms comes from this shallow expulsion and proximal to deformation front expulsion prior to and in the early stages of lithification.

Fluid from >5 km Depths in the Sedimentary Accretionary Prism

Fluid sourced from depths >5 km also moves though sedimentary accretionary prisms in pervasive or channelized manner (Fig. 5; Vrolijk, 1987; Speed, 1990), and

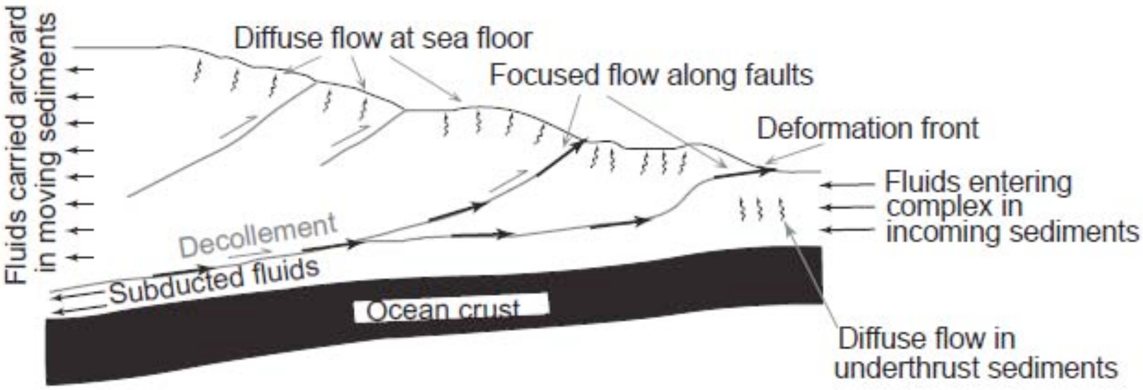

Figure 5. Fluid movement in sedimentary accretionary prisms. Pervasive, or diffuse flow, is dominant in the majority of the sedimentary accretionary prism. Channelized, or focused flow, is present along faults and the décollement, which drains at the toe or deformation front. After Saffer and Bekins (1999).

contributes to pervasive or channelized flow at depths ≤5 km in the prism. The clay smectite is ~20 wt% H_2O and dehydrates in the transition to illite (12 wt% H_2O) at ~100°C, or ~5 km depth (Bird, 1984; Vrolijk, 1990). At greater depths, lawsonite blueschist (5.4 wt% H_2O) dehydrates to epidote blueschist (3.1 wt% H_2O) (Hacker et al., 2003a). The H_2O expelled by these reactions will flow upward and contribute to the fresh H_2O seeps discussed above.

Hydrocarbons and carbonate- or silica-rich fluids expelled from sedimentary accretionary prisms via décollements or thrust faults may originate from depths up to 14 km, as determined by thermometry, $^{87}Sr/^{86}Sr$, $\delta^{13}C$, and $\delta^{18}O$ analysis (Speed, 1990; Sample et al., 1993). For example, hydrocarbons in the Barbados sedimentary accretionary prism appear to have been produced at depths of 5–15 km (Speed, 1990). Carbonate cements from the toe of the Cascadia sedimentary accretionary prism are depleted in $\delta^{13}C$ and $\delta^{18}O$ relative to marine carbonates and enriched in radiogenic strontium, which Sample et al. (1993) interpret to mean a warm fluid source at ≥5 km depth. Sedimentary accretionary prism décollements and faults serve to channelize fluid flow (Fig. 5), so fluid expelled from these two features is more likely to be from depths greater than fluid escaping via pervasive flow (e.g., Moore & Vrolijk, 1992; Sample et al., 1993).

Metamorphic dehydration reactions also release H_2O, since minerals at the zeolite facies (e.g., lawsonite, 15.3 wt% H_2O) are more hydrous than minerals in the epidote-chlorite zone (e.g., epidote, 1.9 wt% H_2O) and this metamorphic fluid will be available to flow up through the sedimentary accretionary prism (Hacker et al., 2003a). As with models of subduction zone fluid flux, models of dehydration reactions reveal comparatively little detail on reactions occurring at and just above diagenesis conditions at 5–15 km depth within sedimentary accretionary prisms (Hacker et al., 2003b). Consequently, there is a spatial gap for my study to fill by focusing on dehydration over a smaller range in burial depths.

Veins as Records of Fluid Flow

Veins are an extremely important record of fluid movement and rock history because they can record the quantity of H_2O that passed through the rock during formation, and because vein morphology can indicate pressures of formation (see below; Fig. 6; van der Pluijm & Marshak, 2004, p. 160). I will focus on quartz veins, since they are the primary vein type in my study area (see Chapter IV). Fibrous, or crack-seal quartz veins, are formed under high pressures, probably ≥3 kbar (Fisher & Brantley, 1992; van der Pluijm & Marshak, 2004, p. 160) wherein open fractures cannot remain for

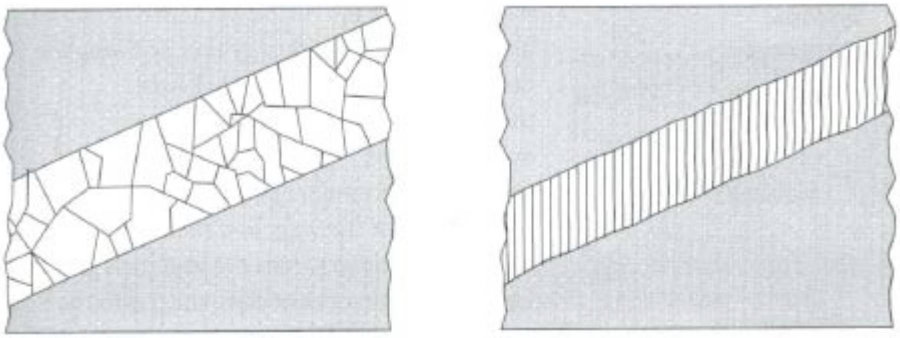

Figure 6. Vein morphologies. Blocky quartz veins (left) form under lower pressure than fibrous quartz veins (right). After van der Pluijm and Marshak (2004, p. 161).

extended periods of time. Blocky quartz veins form close to the surface and/or under lower local confining pressures, probably ≤2 kbar, where void space remains open for relatively free fluid flow (Fisher & Brantley, 1992; van der Pluijm & Marshak, 2004, p. 160). Because they form in open space within the rock, blocky quartz veins may contain characteristic α-quartz hexagonal prisms, which fibrous quartz veins lack (see Chapter IV). Because fibrous veins are filling cracks (representing a zone of weakness), they will preferentially reopen during later high fluid pressure conditions, and therefore it is common for fibrous quartz veins to contain several generations (Fig. 7) of crack-sealing (van der Pluijm & Marshak, 2004, p. 161). Fluid overpressure and fibrous quartz veins are connected to generation of seismicity, and I will return to these implications in Chapter V.

Furthermore, quartz veins are commonly concentrated in comparatively permeable sandstone-rich layers rather than relatively impermeable mudrock (Vrolijk, 1987; Byrne & Fisher, 1990; Fisher & Brantley, 1992; Rotman & Mattinson, 2009), probably as a result of permeability contrasts (e.g., Screaton et al., 1990). The formation

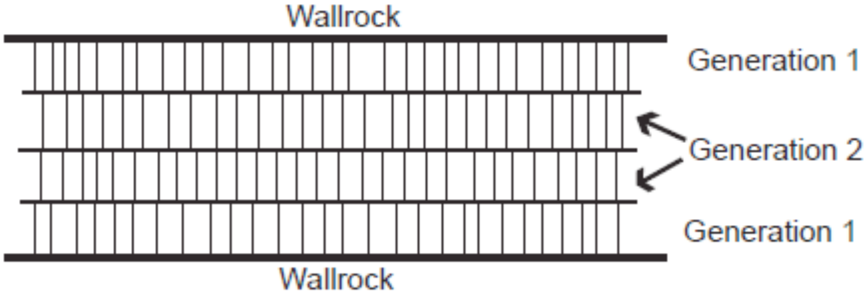

Figure 7. Multi-generation fibrous vein. The first generation forms adjacent to the wallrock, and when the rock fractures again the center fills with the second generation. The process may repeat more times than shown here.

of fibrous veins strongly implies high fluid pressure linked to permeability contrasts between lithologies (Screaton et al., 1990; van der Pluijm & Marshak, 2004, p. 161), and due to relatively low silica solubility a relatively small fraction of quartz veins in outcrop can record large quantities of H_2O flow, as explained in Chapter V.

The Big Picture

Studies of fluid in subduction zones commonly focus on total flux and bulk composition of fluid potentially reaching the mantle at greatest depth in subduction zones (e.g., Plank & Langmuir, 1998), or fluids near the deformation front of modern sedimentary accretionary prisms at shallowest depth in subduction zones (e.g., Sample et al., 1993). These foci are too shallow or too deep to specifically compare to my study results, and furthermore, the bulk flux studies are on a large scale and give relatively little indication as to patterns in dehydration with depth on a km by km basis. However, bulk flux studies are still useful because they can be used in conjunction with literature on H_2O content of oceanic crust and the amount of dehydration at very shallow depths in the accretionary prism (Bird, 1984; Bebout, 1995; Jarrard, 2003) to compare, on an order of magnitude, whether my results are comparable with subduction zone fluid flux models. This is discussed further in Chapter V.

CHAPTER III

METHODS

My project centers around four methods: fieldwork, petrography, X-Ray fluorescence (XRF) and loss on ignition (LOI), and oxygen isotope analysis of vein quartz. I collect samples, make field observations, observe mineral abundances, determine major element composition and volatile content, and verify quartz veins are relevant to my study. The final objective, using all four approaches, is to determine a H_2O budget for rocks in my study transect and determine the quantity of H_2O recorded by quartz veins.

Field Methodology

I conducted fieldwork and sample collection with my advisor, C. Mattinson, October 18–19, 2008 and July 20–24, 2009. All four primary sites on the transect (Fig. 1) had outcrop of at least one rock type (sandstone, mudrock, basalt, or conglomerate), and I collected rock samples at three additional sites. The samples and locations are summarized in Table 2 and Figure 8. I chose my transect and sites to represent burial depths of 6–14 km (Snavely & Kvenvolden, 1989; Brandon et al., 1998) from west to east, representing maximum conditions of ~250°C and ~5 kbar in the east. This approach permits me to examine H_2O content across an 8-km range in burial depths. As much as possible, I collected samples of each rock type at each location to compare mineralogy and major element composition across my study transect. Drastic differences could indicate compositions too diverse to effectively compare H_2O content at different sites. I also collected from as many different units of Tabor and Cady (1978a) as possible to

TABLE 2. SAMPLE DATA

Sample number	Distance east on transect (km)	Coordinates (GPS NAD27)	Site	Rock Type	Unit (Tabor & Cady, 1978a)	Vein	Analyses
OP1	42	0460480E 5314530N	Hurricane Ridge	Sandstone	Needles-Gray Wolf	N/A	Petrography
OP2	42	0461123E 5314128N	Hurricane Ridge	Sandstone	Needles-Gray Wolf	N/A	Petrography
OP3	52.5	0471756E 5307238N	Obstruction Peak	Sandstone/ siltstone	Needles-Gray Wolf	Quartz: fibrous, blocky	Petrography
OP4	41	0471990E 5316770N	Hurricane Road	Basalt	Crescent	Calcite	N/A
OP5	65	0480715E 5311110N	Deer Park	Sandstone	Blue Mountain	N/A	N/A
OP6	37	0456920E 5312345N	Elwha East	Slate	Needles-Gray Wolf	N/A	N/A
OP7	35	0454320E 5314440N	Elwha West	Sandstone	Needles-Gray Wolf?	N/A	Petrography, XRF
OP10	42	0461365E 5313882N	Hurricane Ridge	Slate	Needles-Gray Wolf	N/A	N/A
OP11	42	0461365E 5313882N	Hurricane Ridge	Sandstone	Needles-Gray Wolf	N/A	Petrography, XRF
OP12	42	0461365E 5313882N	Hurricane Ridge	Sandstone	Needles-Gray Wolf	Quartz: blocky	Petrography, stable isotope
OP13	42	0461365E 5313882N	Hurricane Ridge	Sandstone	Needles-Gray Wolf	Calcite	Petrography, stable isotope
OP14	48	0466123E 5311851N	Steeple Rock	Basalt	Needles-Gray Wolf	N/A	N/A

TABLE 2, CONTINUED

Sample number	Distance east on transect (km)	Coordinates (GPS NAD27)	Site	Rock Type	Unit (Tabor & Cady, 1978a)	Vein	Analyses
OP15	48	0466123E 5311851N	Steeple Rock	Basalt	Needles-Gray Wolf	N/A	N/A
OP16	48	0466123E 5311851N	Steeple Rock	Basalt	Needles-Gray Wolf	Calcite	Petrography, XRF, stable isotope
OP17	48	0466123E 5311851N	Steeple Rock	Conglomerate	Needles-Gray Wolf	N/A	Petrography, XRF
OP18	48	0466123E 5311851N	Steeple Rock	Slate	Needles-Gray Wolf	Calcite	XRF, stable isotope
OP19	48	0466123E 5311851N	Steeple Rock	Basalt	Needles-Gray Wolf	N/A	XRF
OP20	52.5	0471699E 5307684N	Obstruction Peak	Sandstone/ slate	Needles-Gray Wolf	Quartz	Petrography, stable isotope
OP21	52.5	0471699E 5307684N	Obstruction Peak	Sandstone	Needles-Gray Wolf	Quartz: blocky; calcite	Petrography, stable isotope
OP22	52.5	0471699E 5307684N	Obstruction Peak	Sandstone	Needles-Gray Wolf	N/A	XRF
OP23	52.5	0471699E 5307684N	Obstruction Peak	Sandstone	Needles-Gray Wolf	N/A	Petrography, XRF, stable isotope
OP24	52.5	0471699E 5307684N	Obstruction Peak	Slate	Needles-Gray Wolf	N/A	Petrography, XRF
OP25	52.5	0471756E 5307238N	Obstruction Peak	Sandstone	Needles-Gray Wolf	Quartz: blocky	N/A

TABLE 2, CONTINUED

Sample number	Distance east on transect (km)	Coordinates (GPS NAD27)	Site	Rock Type	Unit (Tabor & Cady, 1978a)	Vein	Analyses
OP26	52.5	0471756E 5307238N	Obstruction Peak	Sandstone	Needles-Gray Wolf	Quartz: fibrous, blocky	N/A
OP27	52.5	0471756E 5307238N	Obstruction Peak	Sandstone	Needles-Gray Wolf	Quartz: blocky; chlorite	Petrography
OP28	52.5	0471756E 5307238N	Obstruction Peak	Sandstone	Needles-Gray Wolf	Quartz: fibrous, blocky; chlorite	Petrography, stable isotope
OP29	52.5	0471756E 5307238N	Obstruction Peak	Sandstone	Needles-Gray Wolf	Quartz: blocky	N/A
OP30	52.5	0471756E 5307238N	Obstruction Peak	Sandstone	Needles-Gray Wolf	Quartz: fibrous	N/A
OP31	52	0471900E 5306720N	Obstruction Peak	Sandstone	Grand Valley	N/A	Petrography, XRF
OP32	50	0469237E 5307600N	Obstruction Peak	Sandstone	Grand Valley	N/A	XRF
OP33	36	0455041E 5314469N	Elwha West	Basalt	Elwha	Calcite	Petrography, XRF
OP34	36	0455041E 5314469N	Elwha West	Slate	Elwha	Calcite	Petrography, XRF, stable isotope
OP35	30	0448980E 5313910N	Elwha West	Slate	Elwha	N/A	XRF

TABLE 2. CONTINUED

Sample number	Distance east on transect (km)	Coordinates (GPS NAD27)	Site	Rock Type	Unit (Tabor & Cady, 1978a)	Vein	Analyses
OP36	9	0428042E 5315904N	Sore Thumb	Conglomerate	Western Olympic	N/A	Petrography, XRF
OP37	9	0426843E 5316013N	Sore Thumb	Sandstone	Western Olympic	Quartz: blocky	Petrography, XRF
OP38	9	0426843E 5316013N	Sore Thumb	Sandstone	Western Olympic	Quartz: blocky	Petrography, XRF
OP39	9	0426843E 5316013N	Sore Thumb	Shale	Western Olympic	N/A	N/A
OP40	9	0428162E 5316475N	Sore Thumb	Shale	Western Olympic	N/A	Petrography, XRF
OP41	0	0419092E 5321991N	Kugel Creek	Sandstone	Needles-Gray Wolf	N/A	Petrography, XRF

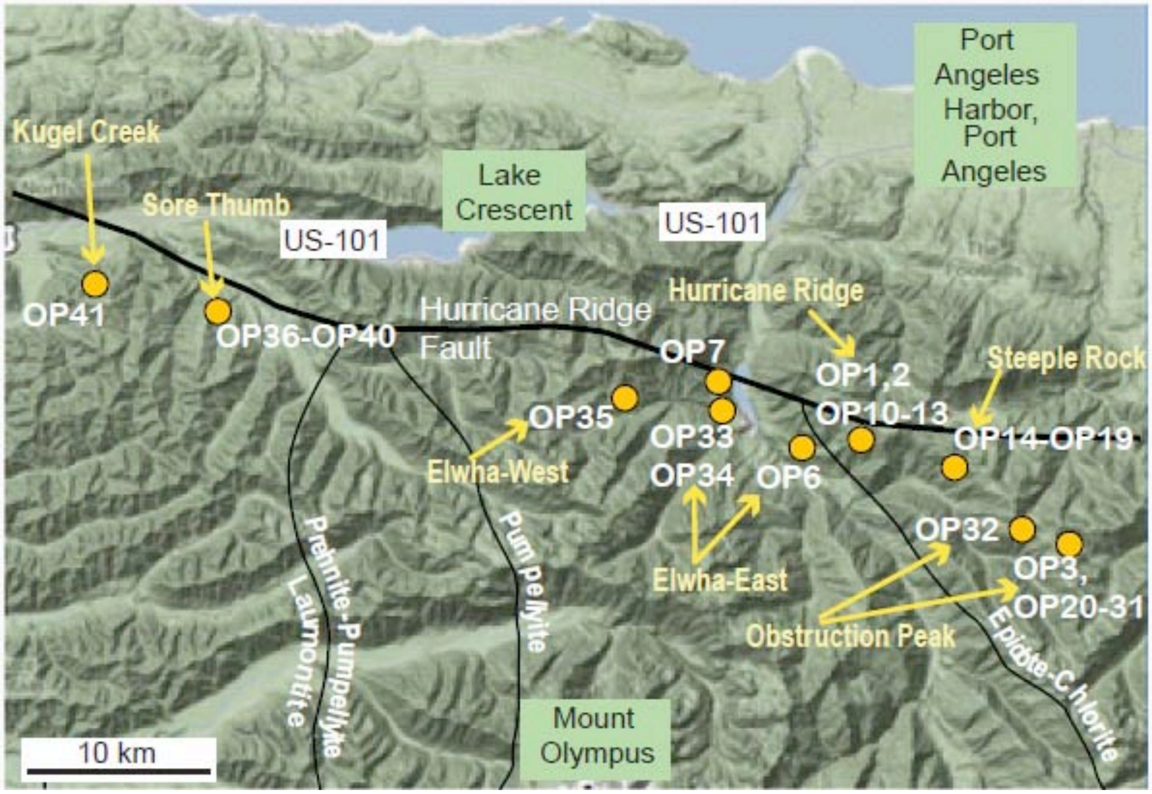

Figure 8. Sample sites, Olympic Peninsula. Close-up of Figure 1a. Samples from Table 2 outside the Olympic core are excluded. Location of Hurricane Ridge fault and metamorphic isograds are marked with black lines, after Tabor and Cady (1978a).

examine changes (or lack thereof) in major element composition and petrography, and four of the five units (Table 1) are represented in my samples.

I collected a total of 39 samples during fieldwork. In addition to selecting the most representative samples of each rock type at every site, I also made observations on the appearance of the outcrop. If veining was present, I estimated the abundance of veins. Vein and bedding orientations, where present, were measured with a Brunton compass.

Fluid movement is important to this study, so I looked specifically for outcrop and samples that contain veins. Quartz ± calcite ± chlorite veins are primarily present at the

Hurricane Ridge and Obstruction Peak locations in the eastern section of my study transect, but they represent a small fraction by volume of the outcrop, as explained in Chapter IV.

Petrography

I cut a total of 24 thin sections from all four rock types and all seven field sites. Bedding is rare in my rock samples, so preferential orientation of the thin section billet was not crucial for most samples. For the sandstones with laminae, bedding, or veins, I cut the thin section billet as close to perpendicular to the feature as possible. Five sections of mudrock and conglomerate were polished for potential analysis by electron microprobe, and the remainder are standard thin sections with cover slips. Sectioning services were provided by Applied Petrographic Services in Pennsylvania. Eighteen of the thin sections were impregnated with blue epoxy to determine the volume of pore space.

In addition to the thin sections I cut from my samples, I have 88 thin sections on loan from R.W. Tabor of the United States Geological Survey. These sections represent samples from many sites I did not reach during this study, since they were collected for Tabor and Cady (1978a, b).

I used a Nikon microscope fitted with 5x, 10x, and 40x objectives in the Central Washington University (CWU) Optical Lab to analyze and photograph my thin sections. I utilized the plane and cross polarized light functions as required to identify minerals and features for a complete thin section description, as elucidated in Chapter IV.

X-Ray Fluorescence

X-Ray fluorescence and LOI analyses were performed on 19 representative, vein-free samples at Washington State University (WSU) GeoAnalytical Lab facilities in Pullman, WA. I selected the samples to represent the maximum number of sites, rock types, and units of Tabor and Cady (1978a) to compare major element composition and rock provenance in samples along my transect.

I coarse chipped my samples with a 20 oz rock hammer in a walled platform in the CWU Geology rock cutting and crushing room with the assistance of Nick Zentner of CWU Geology. Pieces with >50% external (weathered) surfaces and any cut surfaces were set aside, and the remainder were placed in a sample bag for fine chipping. Six samples were fine chipped (~1 cm) and picked at CWU. I traveled to WSU to prepare my samples for analysis. I randomly selected approximately 150 g from each of the 19 samples, and chipped this quantity in the jaw crusher at WSU for sample consistency. With all preparations in this section, I cleaned the equipment between samples with Kimwipes and a compressed air nozzle. I used paper to transfer samples when they could not be poured directly from one container to another.

After fine chipping, I poured a randomly selected 30 g per sample into small cups before grinding to powder in the tungsten carbide mills. Each sample was ground for two min in a ring mill consisting of the mill (~15 cm diameter), the ring (~9 cm diameter), and a solid inner puck (~3 cm diameter). After grinding, the samples were placed back into the sample cups, which were covered at all times to prevent contamination.

In XRF analyses, the pellet is not composed of the sample alone. A flux is added to it at a 2:1 ratio. My next step was to weigh out 3.5 g of each sample, and add 7 ± .05 g of flux. I mixed each sample + flux on a spinning platform for 60–90 s. After this, I poured the sample + flux into graphite crucibles, which I then placed on a silica tray and slid into a muffle furnace. The furnace was set to 1000°C, and the samples remained in the oven for 45 min after this temperature was reached. After 45 min, the silica tray was pulled out with tongs and the newly formed pellets were allowed to cool.

After cooling, I used the mill described above to regrind each sample for 30 s, then transferred the powder back to the crucibles and re-fused each pellet as before. One pellet showed bubbling after this second fusion and was placed back in the oven a third time. After cooling, each sample was engraved for identification, polished against diamond, and then rinsed with alcohol before being transferred to the XRF spectrometer. My samples were run against nine United States Geological Survey standards (PCC-1, BCR-1, BIR-1, DNC-1, W-2, AGV-1, GSP-1, G-2, and STM-1) and two vein quartz internal standards (Johnson et al., 1999) to determine concentration of 27 major and trace elements by comparing X-ray intensities, a process that takes ~65 min per sample. The major elements analyzed were Si, Al, Ti, Fe, Mn, Ca, Mg, K, Na, and P, to an accuracy of ±0.1%. The trace elements analyzed were Sc, V, Ni, Cr, Ba, Sr, Zr, Y, Rb, Nb, Ga, Cu, Zn, Pb, La, Ce, Th, Nd, and U, to an accuracy of ±2% within detection limits (Johnson et al., 1999). The operating conditions of the XRF spectrometer at WSU are such that results can be reproduced over a time period of 10 years or more, leading to a high degree of confidence in the results (Johnson et al., 1999).

Loss on ignition measurements were performed separately from XRF procedures, using the same powder from which the pellets were formed. Approximately 1 g of powder was weighed on a microbalance, then placed in carbon crucibles for 16 h at 900°C in the same muffle furnace as above, and then reweighed (Conrey, 2010, written commun.). Since the oxidizing/reducing environment of the muffle furnace is not controlled, FeO may oxidize to Fe_2O_3, causing a mass gain. However, analytical totals near 100% indicate this problem is not substantial for the Olympic Peninsula samples (see Chapter IV). The samples are not desiccated, so all volatiles are included in the LOI value, including organics and minerals hydrated by near-surface alteration. Consequently, LOI may not accurately reflect the pre-exhumation H_2O content of the rock sample, an uncertainty that was especially noticeable in one slate sample. This will be discussed further in Chapter IV. The sample's loss of mass is reported as a weight percent, and I estimate the relative uncertainty for LOI values at ~10%.

Oxygen Isotopes

Seventeen samples I collected during fieldwork contained veins of quartz or calcite (predominantly quartz; see Table 2). I selected representative samples and chipped off several grams of quartz or calcite with a pocketknife, rock hammer, or a jewelry clamp with a blunt or sharp tip. I then ground or hammered the samples to 1–2 mm diameter pieces and placed each sample in a capped glass vial labeled with the sample number, mineral, and, if the sample was quartz, whether fibrous or blocky. Because only 3 mg at most of each sample is required for analysis, I ground the samples again with a mortar and pestle, using H_2O to keep the sample pieces from bouncing out of the mortar. After drying, I hand-picked each piece of sample for wallrock or other contaminants, so only quartz or calcite would be analyzed.

In order to further assure only the mineral of interest was analyzed and to keep potentially damaging contaminants out of the equipment, I washed the samples in acid and/or alcohol as appropriate to the mineral. I rinsed the calcite samples with distilled H_2O and then washed them briefly (~30 min) in alcohol. I bathed the quartz samples in 8% HCl for ~20 h, the first 45 min of which the samples were on a warmed hot plate to speed the cleaning reactions. After draining the acid, I rinsed the quartz samples with distilled H_2O and then alcohol as with the calcite samples. I marked the top of each vial with an A after acid wash and L after the alcohol wash.

I performed the oxygen isotope ratio analyses at WSU in Pullman, WA in the laboratory of Dr. Peter Larson with the assistance of Dr. Larson and Dr. Charles Knaack. I weighed 1.5 to 3 mg of my quartz samples (usually 2 or 3 grains) into one of 18 holes in a sample holder (or puck). I weighed a MM-1 internal quartz standard to analyze first to clean out the vacuum line, and for every three of my unknowns, which I analyzed in replicate, I also weighed one standard UWG-2 garnet of Valley (1995). After loading the puck into its chamber, I opened the line to two vacuum pumps until a relatively clean vacuum (<5 torr) was achieved; the time in vacuum is to prevent the samples from being contaminated by atmospheric gas.

I ran my samples against the UWG-2 garnet standard of Valley (1995), which has a well-established value of +5.8‰ relative to standard mean ocean water. During the three days of sample analysis on the isotope ratio mass spectrometer, UWG-2 varied from

+4.8 to +7.9‰. This level of variation in the standard is undesirable, and causes uncertainty in the $\delta^{18}O$ values of unknowns presented in Chapter IV. However, the variation in the replicate analyses is not necessarily an artifact of poor standard reproducibility, because a replicate unknown run with two acceptable UWG-2 values also gave heterogeneous $\delta^{18}O$ values. The heterogeneity of $\delta^{18}O$ values may therefore be genuine. I used the changes in UWG-2 values with time to correct the $\delta^{18}O$ values of my unknowns and then calculated the standard deviation of the $\delta^{18}O$ values.

I released the oxygen in each sample by using the BrF_5 laser fluorination technique. I used valves on the vacuum line to release sufficient BrF_5 to analyze 5–6 samples, then released a smaller quantity into the chamber with the sample holder. Then, by a joystick control system attached to a laser above the chamber, I warmed up and then burned off a single sample at a time. I burned multiple pieces rather than a single intact quartz crystal and burned ~95% of each sample. Based on earlier fluorination studies of Taylor (1967, p. 116), yields slightly below 100% are sufficient to accurately determine the $\delta^{18}O$ value of quartz except in cases of unusually isotopically fractionated zoning (Valley, 2001, p. 370). After burning the sample, I used a cold trap for six min to draw the gas into a molecular sieve in a test tube welded to the line, then heated the gas for five min by placing a heating coil around the test tube with the molecular sieve. To move the gas again so I could transfer it to the mass spectrometer, I used a cold trap for five min to draw the gas toward a second test tube with a molecular sieve, and then heated it for five min. During the above process, I closed and opened valves to move the sample gas between traps. I transferred the gas into the mass spectrometer for analysis using computer-controlled valves that moved the sample gas into one of two bellows. The second bellows contained a standard gas. The mass spectrometer is fully automated after the sample is in the first bellows and a sample number has been entered into the computer. Each sample is analyzed 10 times to obtain an accurate average, a process that takes about 20 min. From the start of the laser fluorination burn to the last analysis in the mass spectrometer, each sample takes ~60 min to analyze.

CHAPTER IV

RESULTS

Field Observations

The majority of outcrops on the Olympic Peninsula are weathered, thick to massively bedded or interbedded sandstone and mudrocks (Fig. 9; Tabor & Cady, 1978a, b). Basalt and conglomerate are minor (<1%) rock types. Sandstones are less susceptible to weathering than mudrocks and represent ~65% of the outcrop area I observed during fieldwork October 18–19, 2008 and July 20–24, 2009. Field observations are

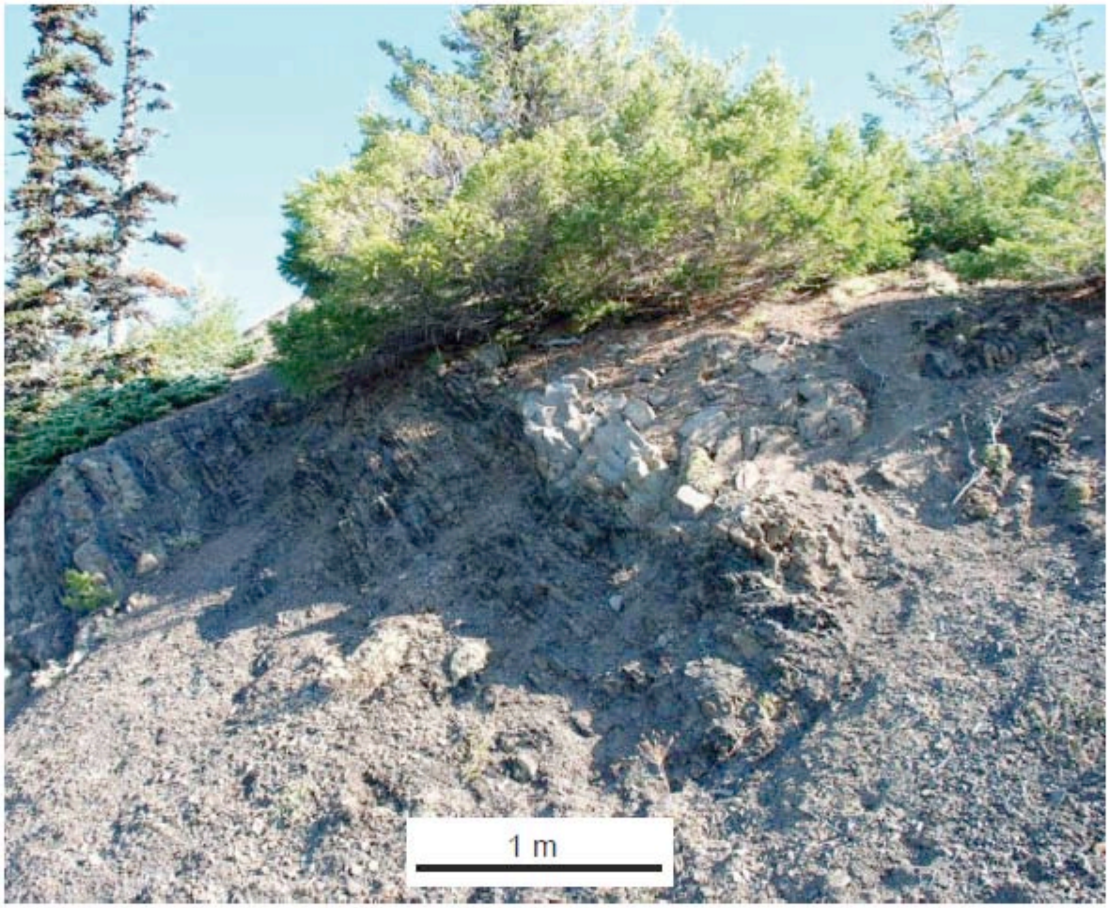

Figure 9. Sandstone and slate turbidite sequence along Hurricane Hill trail. The sandstone is light in color and the slate is dark. Photo C. Mattinson (2008).

summarized in Table 3. With the exception of minor phyllite at Obstruction Peak, all the rocks are identifiable as their respective protoliths; that is, they have undergone burial, deformation and recrystallization, but still fundamentally have the appearance of sandstone or shale. At most sites, bedding is not identifiable due to depositional

TABLE 3. SUMMARY OF FIELD OBSERVATIONS

Site and samples	Observations
Obstruction Peak	Moderately sorted, subangular
OP3, OP20–32	Laminated to thinly bedded sandstone, siltstone & slate common
	Thickly bedded slate & sandstone also present
	Folding
	Brittle & ductile deformation of bedded/laminated units
	Phyllite present: very localized
	Multiple faults, offset >25 cm
Steeple Rock	Minerals weathered out of basalt samples
OP14–19	Lenses of calcite in slate, calcite present in conglomerate
Hurricane Ridge	Turbidite sequences of sandstone and slate
OP1, 2, 10–13	Interbedded sandstone & slate, beds commonly >50 cm thick
	Sandstone micaceous but less so adjacent to veins
Elwha-East	Basalt and slate have greenish cast, calcite veins
OP6, 7, 33, 34	Sandstone from observation point very micaceous
Elwha-West	Very black slate with shearing & weak pencil cleavage
OP35	
Sore Thumb	Possibly graded bedding
OP36–40	Local changes in weathering characteristics
	Small, irregular <1 mm thick quartz veins
	Relatively few micas
Kugel Creek	Micaceous sandstone, especially cloven surface of OP41
OP41	Strongly resembles Elwha-East OP7
	Outcrop in fault-bounded block of Needles-Gray Wolf unit

characteristics and weathering since exhumation. However, at Obstruction Peak bedding ranges from laminated sandstone and shale (Fig. 10) to thickly bedded sandstone and shale, and numerous small faults (Fig. 11) and folds are visible along a ~400 m discontinuous outcrop. I observed pencil cleavage in slate at Obstruction Peak, and poorly developed cleavage at Elwha-West and Sore Thumb. Some of the sandstones at Obstruction Peak have carbonate cement, possibly synonymous with vein formation, and/or are locally calcareous. Veins of quartz ± calcite (Fig. 10, 11) are a minor component of Olympic Peninsula outcrop. The significance of veins and carbonate cement will be explained in detail in Chapter V.

Figure 10. Slate and laminated sandstone with quartz veins, Obstruction Peak. Red arrow points to where a primarily fibrous quartz vein (partially weathered out) ceases abruptly at contact between laminated sandstone and slate. Lens cap for scale. Photo C. Mattinson (2009).

Figure 11. Laminated and interbedded sandstone and slate truncated by fault, Obstruction Peak. Quartz veins (white) are still generally perpendicular to bedding, as in Figure 10. Photo C. Mattinson (2009).

The only locations I observed with measurable bedding and veins are Hurricane Ridge and Obstruction Peak (Fig. 1). At Obstruction Peak, 10 bedding measurements of laminated to thickly bedded sandstone and slate were obtained with a Brunton compass (Fig. 12). The beds have a clustered orientation, with a strike of ~140° and dip of 37° to 78°, all toward the south. Using the same method the orientation of 26 veins at Obstruction Peak and 13 veins at Hurricane Ridge were measured. The veins at Obstruction Peak are generally perpendicular to bedding, but show some variation, possibly due to the timing of folding versus the timing of vein formation. The laterally discontinuous veins and lenses at Hurricane Ridge are mostly shallowly dipping.

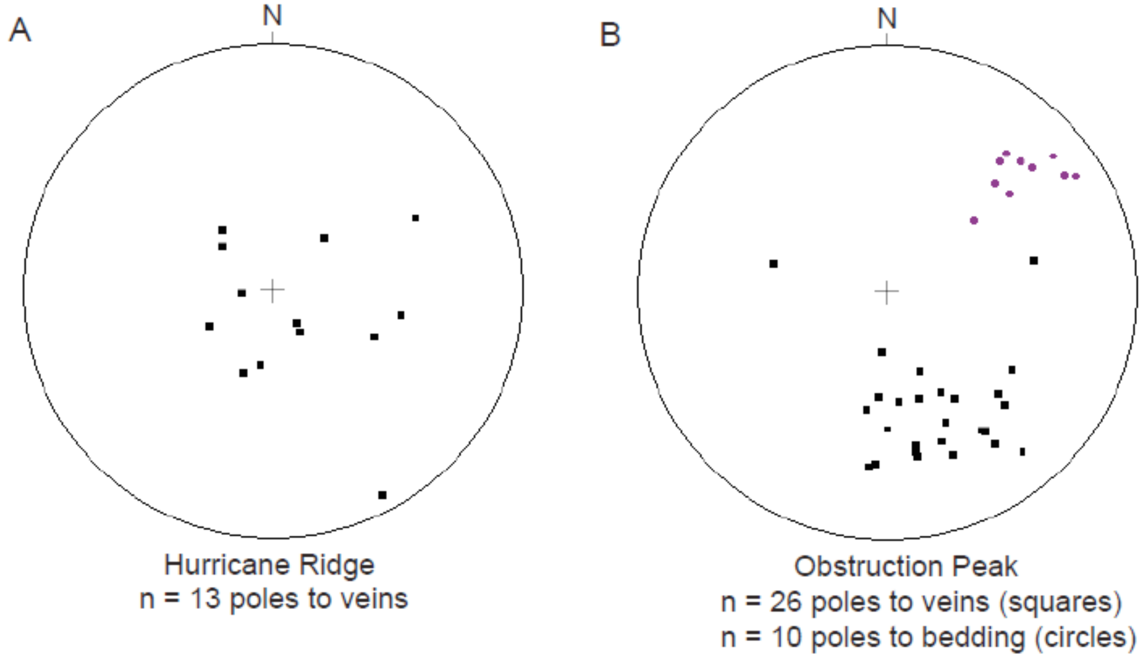

Figure 12. Poles to bedding and vein orientation, Hurricane Ridge and Obstruction Peak. (A) Veins, Hurricane Ridge. (B) Bedding and veins, Obstruction Peak. Full data tables are provided in Appendix A. Plotted using GEOrient (Holcombe, 2009).

Obstruction Peak has the greatest volume percent of veins of any site, but the quartz ± calcite veins are still a minor outcrop component. The majority of the veins are quartz, were deposited in two or more episodes, are 0.1–2 cm thick, are perpendicular to bedding, and stop or possibly deflect at contacts with mudrock (Fig. 10). I used two discontinuous outcrop sequences to estimate the percent of quartz veins at the Obstruction Peak site. The longer of the two outcrop sequences is ~400 m on the east face of Obstruction Peak, where there were several outcrop exposures ≥5 m long at trail level. I walked along the outcrop and visually estimated the percentage of veins for each length exposed, such as 7% veins in 10 m of outcrop (Appendix A). I chose the longest continuous outcrop, which was also immediately adjacent to the trail, and paced it, noting the length with and without veins, and then selecting 1 and 2 m sections with veins for which I measured vein thickness and the number of veins (Appendix A). At the second outcrop, which is ~20 m long, I randomly chose two shorter sections and measured the thickness and number of veins. I combined my observations to determine that veins are 0.5–1% by volume of Obstruction Peak outcrop, which based on field observations I estimate to be applicable to a modern volume of ~700 m by 200 m by 600 m.

Petrography

I made detailed observations (Appendix B) of a representative thin section suite of nine sandstones to identify the mineral assemblages, modal abundances of minerals, and features of interest (e.g., laminations, preferential grain orientation), and examined four more on loan from R.W. Tabor to find minerals and features of interest. The sandstone mineral assemblage is quartz + sericite + muscovite + lithics + plagioclase + opaques ±

calcite ± epidote ± chlorite, and the cements are silica or carbonate with minor iron oxide. The matrix is composed of sericite, carbonate, and material too fine to identify, probably phyllosilicates. In general, sandstones from the eastern sites are calcite-bearing in the form of calcareous matrix and cement, and sandstones from the western sites are rich in polycrystalline quartz and lithics. The rocks are poorly to moderately well sorted, and bedding is uncommon. Some rocks are laminated (Fig. 13). In ~40–50% of sandstones phyllosilicate grains, especially muscovite, show at least a weak preferential orientation (Fig. 13, 14) and/or distort around comparatively rigid grains such as quartz. Metamorphic minerals such as epidote and pumpellyite are rare, making up <1% of the sandstones. Hydrous minerals and components (e.g., lithics) compose up to 40 vol% of the nine sandstones (Table 4).

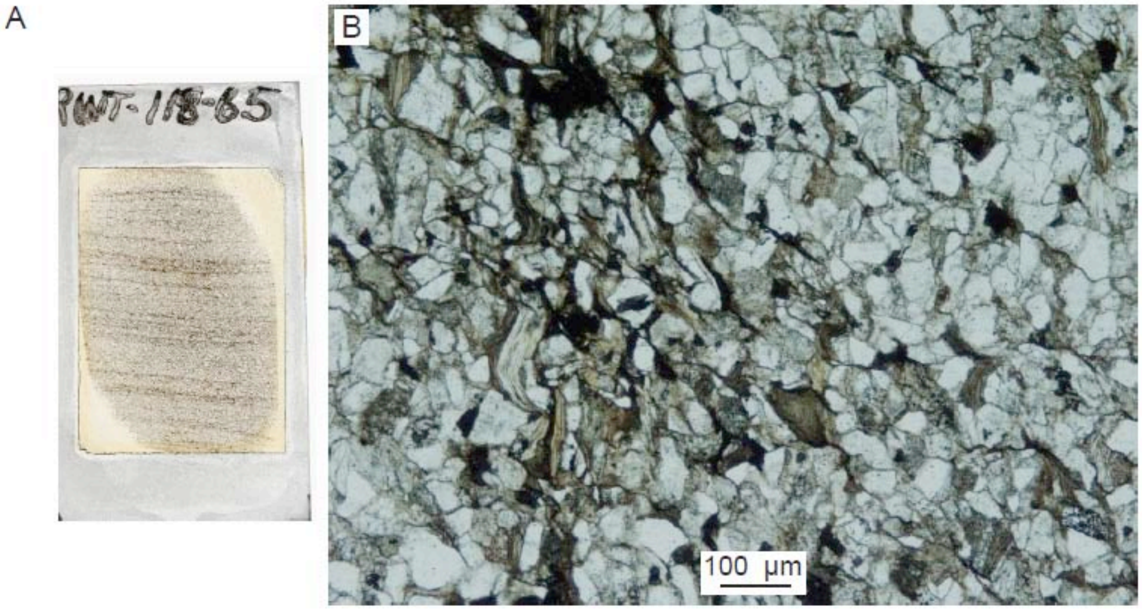

Figure 13. Laminated sandstone, sample RWT-118-65, ~7 km S of Steeple Rock. (A) Thin section scan, clearly showing laminations. (B) Microphotograph, plane polars, 10x, sample RWT-118-65. In the left field of view is a mica-rich lamination and in the right field of view is a quartz-rich lamination. Thin section courtesy R.W. Tabor.

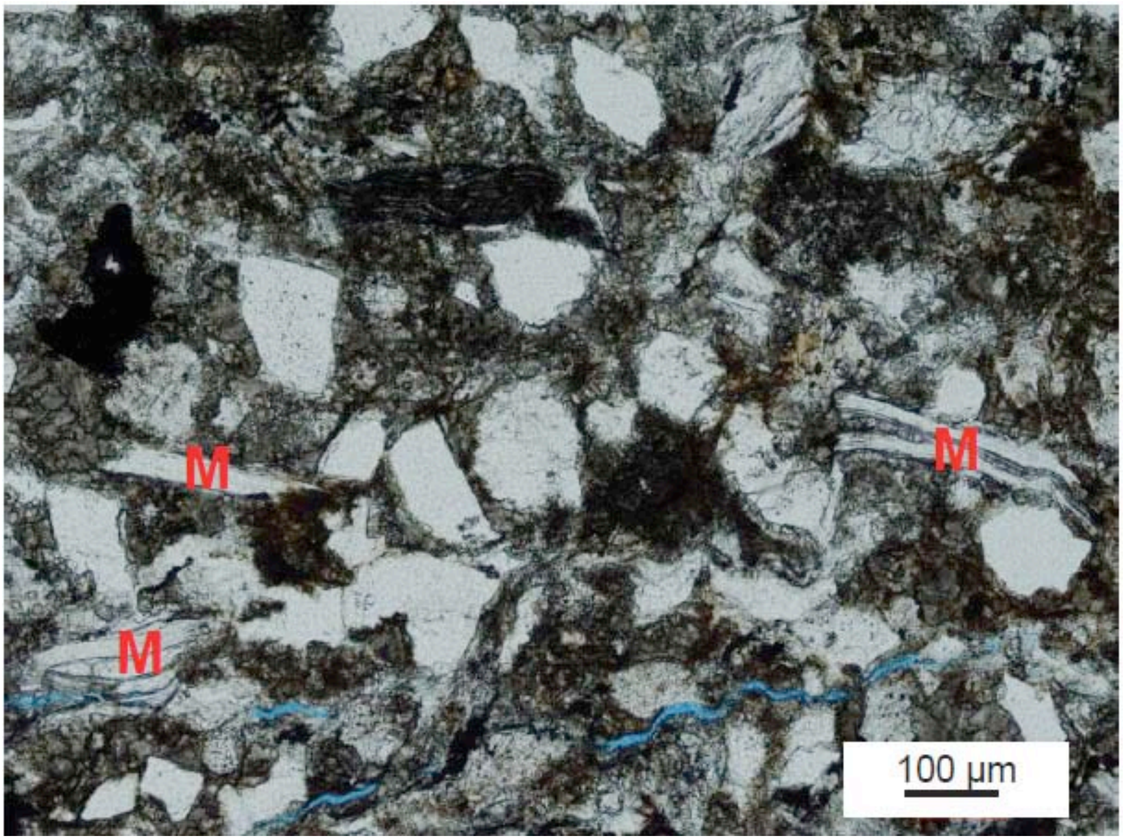

Figure 14. Microphotograph, plane polars, 10x, sample OP21, Obstruction Peak. Micas (M) with a weak preferential orientation approximately parallel to the scale bar are visible to the lower left and center right.

TABLE 4. HYDROUS COMPONENTS OF SELECTED SANDSTONES

Component* ($wt\%H_2O^{\dagger}$)	OP37	OP7	OP13	OP31	OP23
Chlorite (13)	2	1	N/A	trace	trace
Sericite (4.5)	8	20	17	25	17
Muscovite (4.5)	1	8	3	7	8
Kaolinitized mica ($4.5^{\S}$)	N/A	10	5	6	3
Biotite (4.5)	N/A	3	N/A	3	N/A
Lithics[#] (6–3)	30	2	3	8	10
Matrix[#] (6–3)	15	trace	trace	trace	trace
Epidote (1.9)	trace	trace	N/A	N/A	trace
Total H_2O (wt%)	3.4 ± 0.6	2.1 ± 0.5	1.3 ± 0.3	1.9 ± 0.3	1.6 ± 0.3

Note: Uncertainties of abundance estimates are ±15–20% relative.
*Components are given in vol%.
[†] From Hacker et al., 2003a, unless specified otherwise.
[§] Pre-weathering value. See text.
[#] Based on lithics being primarily fine-grained (shale) and the loss on ignition trend for mudrocks, Olympic Peninsula.

Some minerals, such as plagioclase and mica, are prevalently altered. Almost without exception, plagioclase bears fine-grained sericite alteration (Fig. 15), which is a common alteration product of plagioclase. It is common for plagioclase twinning to be preserved and the alteration to cover <50% by area of the plagioclase grain. Some plagioclase alteration may be pumpellyite, as indicated by green pleochroism and high relief, but the grain size is too fine to make the determination with certainty via optical microscopy alone. Micas commonly show signs of low-temperature (<15 m from surface) alteration (DeIvigne, 1998, p. 158). The original mica species (e.g., biotite) of

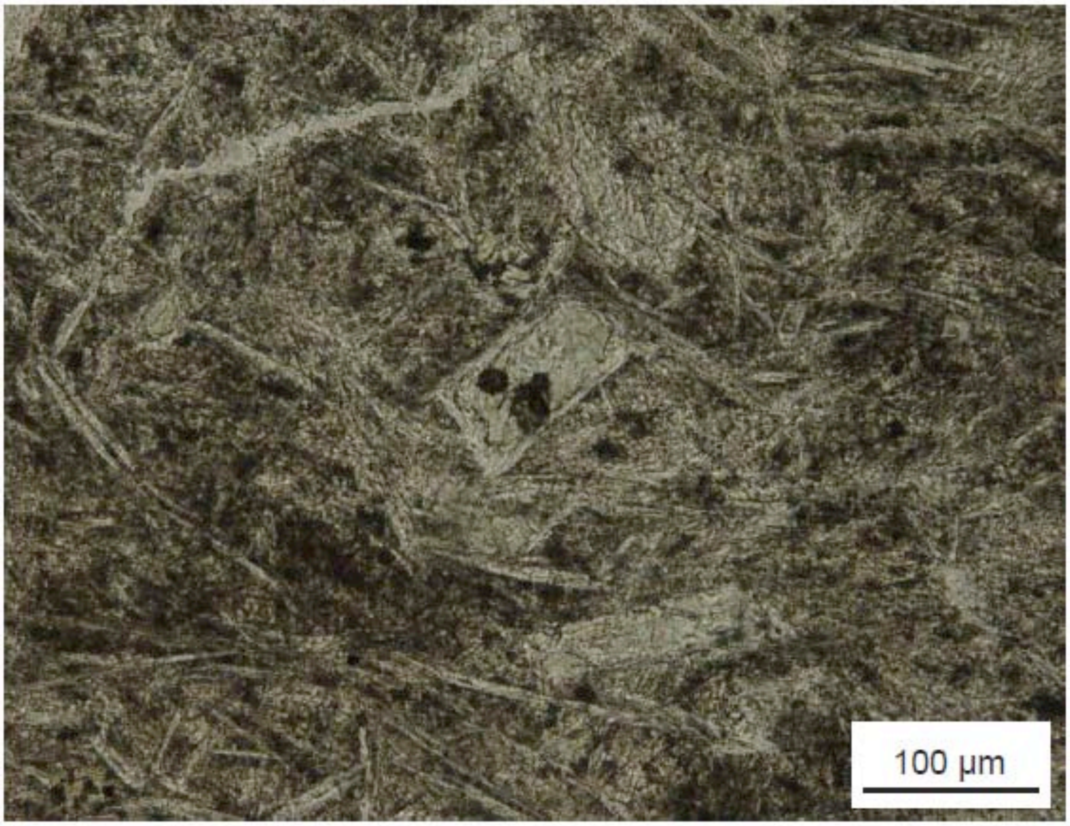

Figure 15. Microphotograph, plane polars, 10x, sample RWT-18-70, 15 km W of Sore Thumb. Abundant in the field of view are plagioclase crystals (white) altered to sericite and chlorite (light green). Section courtesy R.W. Tabor.

these altered grains is unknown, but in most sandstones ~15% of the micaceous minerals demonstrate swollen cleavage, distorted crystal shape, and are brown in both cross- and plane-polarized light with minimal pleochroism (Fig. 16). I therefore interpret that the altered micas have been converted to a clay such as kaolinite via low-temperature weathering processes (DeIvigne, 1998, p. 158) and they are reported as such in Table 4 and Appendix B.

Minerals that are indicative of metamorphism and/or fluid infiltration, such as chlorite and calcite, are for the most part minor but compose ~40–60% of a few samples, particularly at Steeple Rock and Elwha East. Calcite is extensive in slate, basalt, and

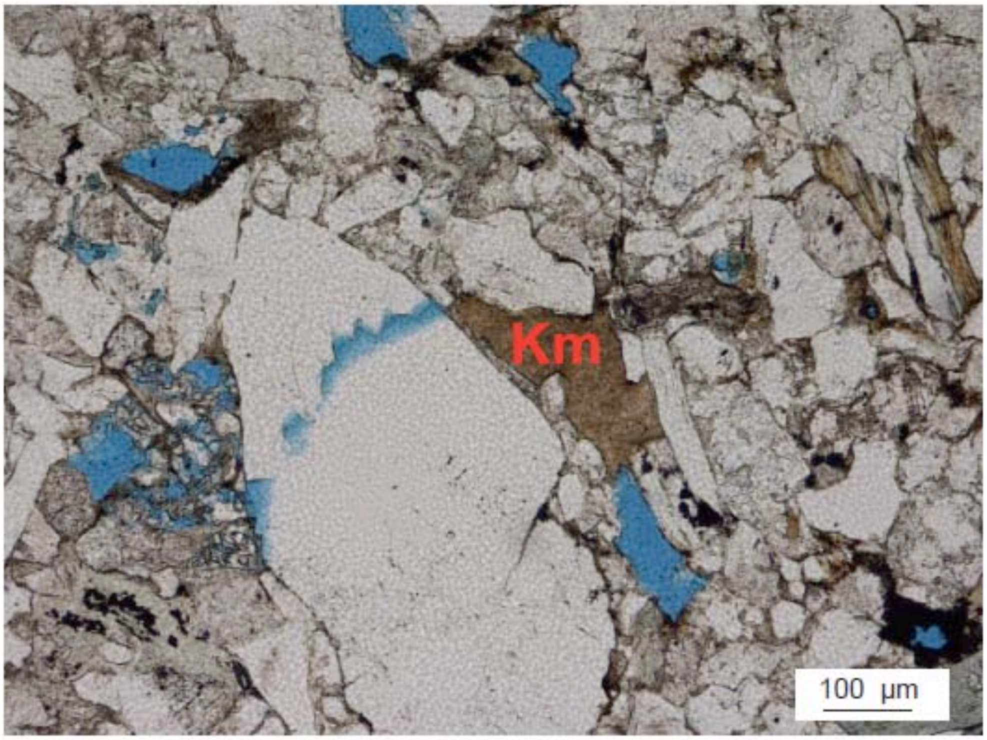

Figure 16. Microphotograph, plane polars, 10x, sample OP41, Kugel Creek. The brown mineral (Km) is swollen mica, possibly turned to kaolinite by low-temperature alteration. The blue areas are epoxy filling space where minerals have weathered out.

conglomerate at Steeple Rock, and chlorite is widespread in conglomerate at Steeple Rock (Fig. 17). Calcite and chlorite is also prevalent in basalt from Elwha East; the slate from the same location is too fine-grained to identify any minerals in thin section. I will return to the importance of these observations later this chapter. In addition, sample RWT-18-70 from ~15 km west of Sore Thumb contains calcite veins and chlorite overgrowth around lithic fragments and other grains (Fig. 18).

Veins are an important feature and exhibit diverse appearance in thin section. Veins in my Olympic Peninsula samples are quartz ± calcite ± chlorite (Table 3); the chlorite can only be identified in thin section and in hand sample is visible as an indeterminate green mineral. Quartz veins at Obstruction Peak are fibrous to blocky.

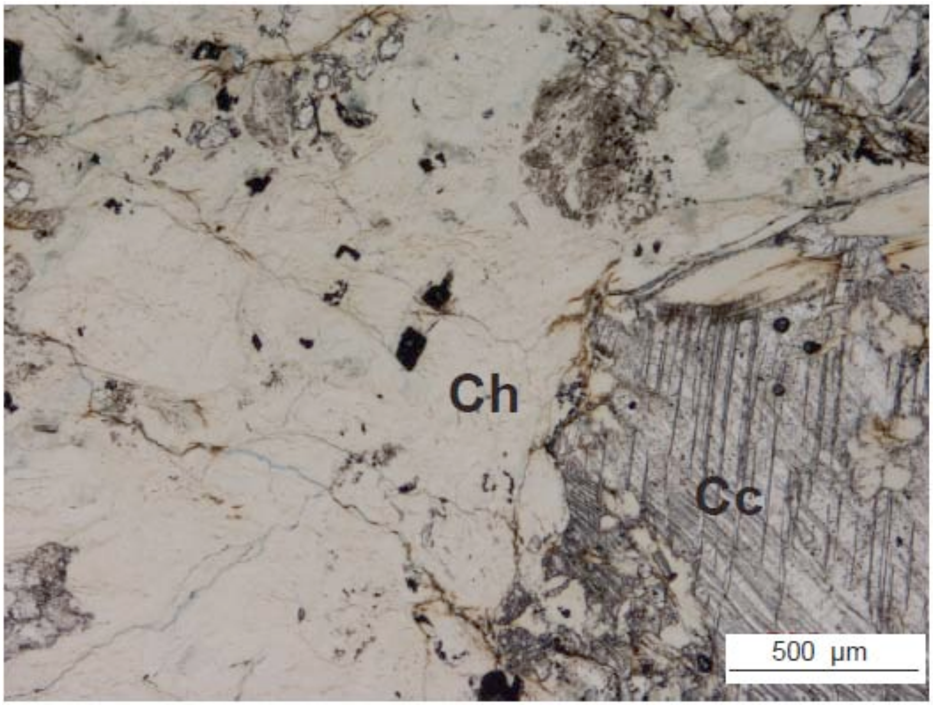

Figure 17. Microphotograph, plane polars, 5x, sample OP17, Steeple Rock. Chlorite (Ch) is pale yellow and is the left two-thirds of the photo. Calcite (Cc) is distinguished by twin lamellae in the lower right.

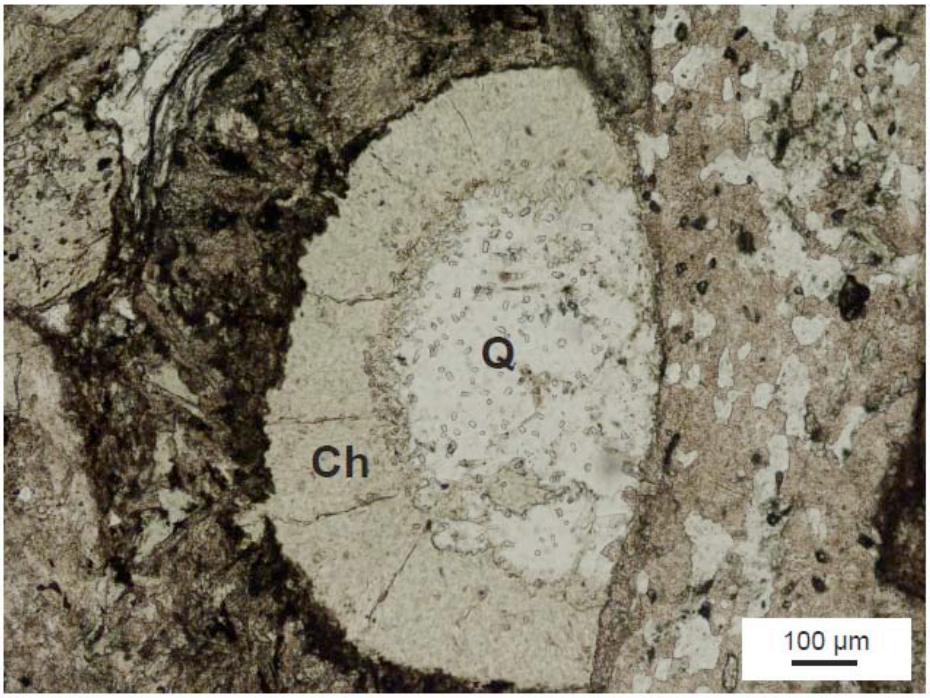

Figure 18. Microphotograph, plane polars, 10x, sample RWT-18-70, 15 km W of Sore Thumb. Chlorite (Ch) and quartz (Q) have grown within a dark volcanic lithic. Section courtesy R.W. Tabor.

Blocky quartz may coexist with chlorite or calcite or bear fluid inclusions (Fig. 19). Fibrous quartz veins at Obstruction Peak may show multiple generations of formation (Fig. 19C). I observed blocky quartz veins in samples from Obstruction Peak, Hurricane Ridge, and Sore Thumb, and overall the vein thickness and size of quartz crystals decreases from east to west.

Some samples at Obstruction Peak also bear indicators of brittle or ductile deformation. There are microfaults, crenulation cleavage, and evidence of shearing and quartz stretching on the thin section scale (Fig. 20).

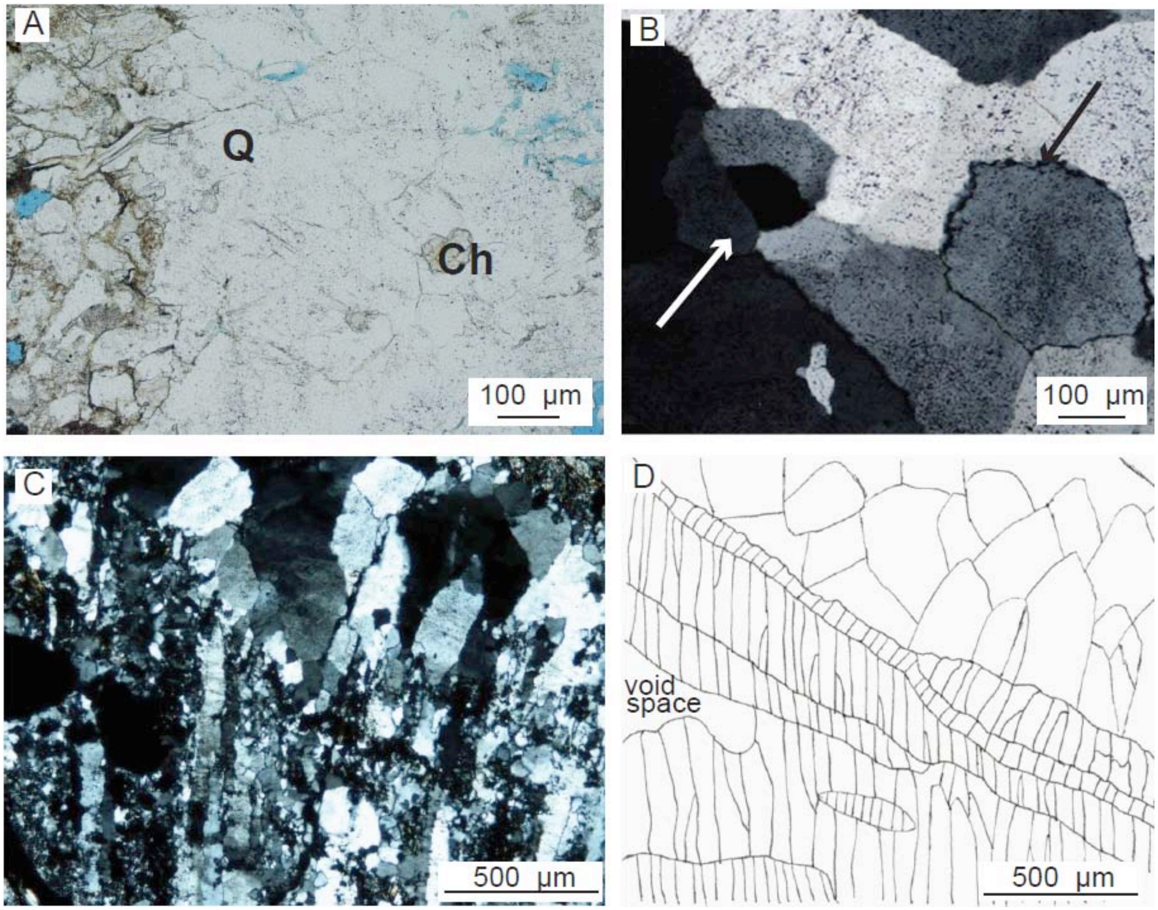

Figure 19. Different styles of quartz vein growth. (A) Sample OP28, plane polars, 10x. Blocky quartz vein, featuring fluid inclusions densest in the vicinity of Q label, and a chlorite book, labeled Ch. (B) Sample OP3, crossed polars, 10x. Blocky quartz vein, showing roughly hexagonal basal quartz section (black arrow) and a basal section cut obliquely so the facets of the hexagon are visible (white arrow). (C) Sample OP3, crossed polars, 5x. Multi-generation fibrous quartz vein. (D) Sketch, showing different vein generations and growth styles from (C).

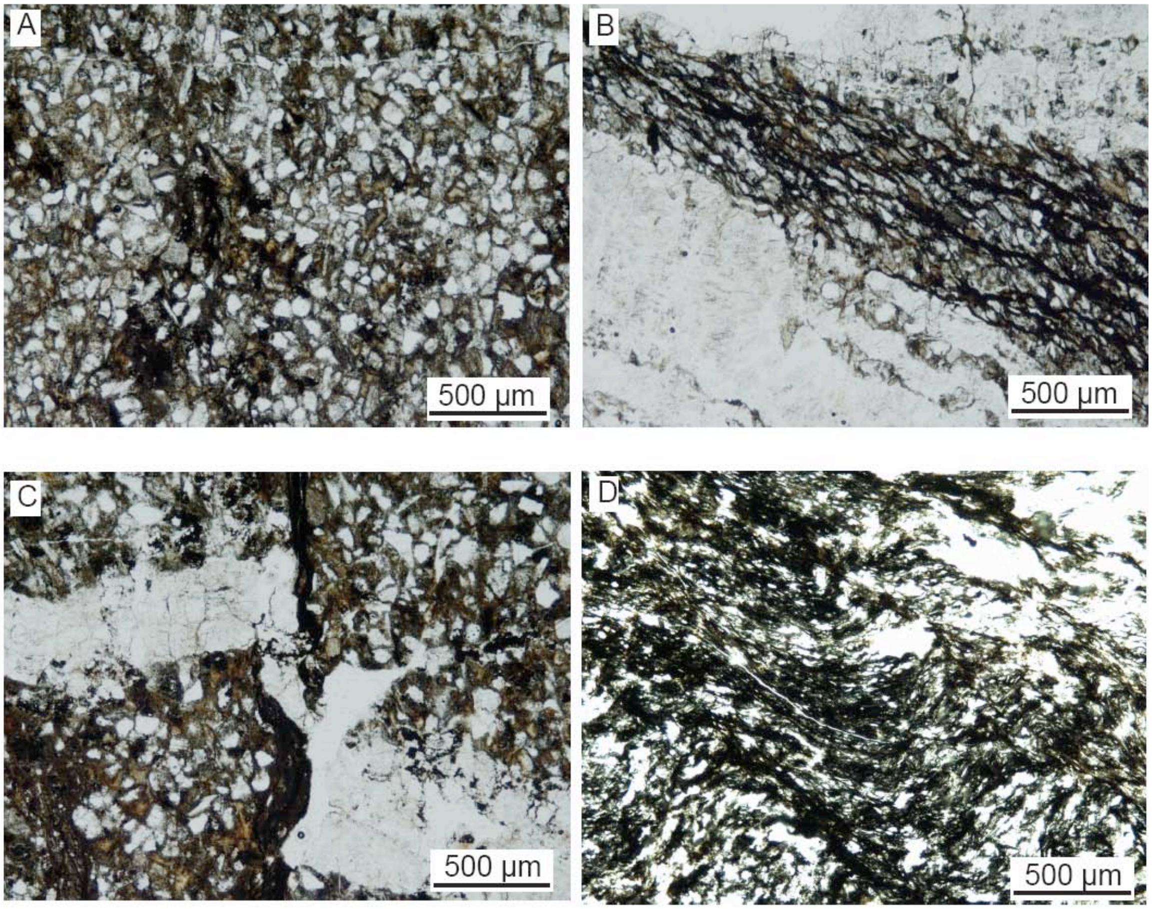

Figure 20. Deformation at Obstruction Peak. (A) Sample OP3, plane polars, 5x. No deformation is visible, although there is some pressure solution (dark). (B) Sample OP3, plane polars, 5x. Pressure solution, apparent as dark strings, is abundant, and the rock has fractured to form quartz veins, bottom left and top right (colorless). Photograph taken ~2 cm from (A). (C) Sample OP3, plane polars, 5x. Blocky quartz vein (colorless) offset by microfault with ~.75 mm offset. This quartz vein is fibrous along parts of its length, which may imply substantial fluid pressure changes during formation. (D) Sample RWT-235-64, plane polars, 5x. Crenulation cleavage, emphasized by graphite or pressure solution (black) and quartz and muscovite microlithons (colorless). Section courtesy R.W. Tabor.

Whole Rock Geochemistry

I had XRF analyses performed on nine sandstones, five mudrocks, three basalts and two conglomerates from eight different localities and four lithologic units of Tabor and Cady (1978a) along my 52.5 km transect. Major elements and LOI are reported for selected samples and examples from literature in Tables 5, 6, and 7. Complete XRF results are in Appendix C.

Several trends are visible in the major element data (Fig. 21–25), dependent on rock type, but overall the samples are fairly similar geochemically across my study transect (see below). All the sandstones (with one CaO and volatile-rich exception) contain ≥67 wt% SiO_2 (Appendix C). Total Fe content is 3–6 wt%, and MgO is less abundant, at 1–3 wt%. CaO content is generally <1.5wt% except at the eastern sampling sites. Na_2O and K_2O may be ~2 wt% each, but if this is not the case K_2O is depleted relative to Na_2O. The mudrocks can also be grouped according to major element data. SiO_2 content is ~60 wt% (Appendix C), which is lower than the sandstones. Total Fe is 6–8 wt%, and MgO is 2–4 wt%. With one exception, mudrock CaO content is similar to the sandstones at <1.5 wt%, even when adjacent to CaO-enriched sandstone. The mudrocks display similar behavior to the sandstones in Na_2O and K_2O abundances. The inverse correlation between Na_2O (enriched) and K_2O (depleted), where present, is more pronounced in the mudrocks than sandstones, especially in two of the mudrocks (see below), but excluding those samples mudrocks are more enriched in K_2O than the sandstones. Al_2O_3 content is 13–18 wt%, enriched by comparison to the sandstones. Enrichment in K_2O and Al_2O_3 in the mudrocks over the sandstones is explained by a review of phyllosilicate chemical formulae, which commonly contain K and Al.

Major element data can be used to identify the provenance and type of sandstone and mudrock. The Olympic Peninsula rocks chemically plot in active margin and arc

TABLE 5. X-RAY FLUORESCENCE RESULTS OF SELECTED* SANDSTONES

Oxide (wt%)	OP37 Sore Thumb	OP7 Elwha-East	OP11 Hurricane R.	OP31 Obstruction P.	OP23 Obstruction P.
SiO_2	70.96	74.53	75.11	73.23	68.67
TiO_2	0.70	0.50	0.44	0.40	0.76
Al_2O_3	12.46	12.85	11.98	11.94	13.11
$FeO^{\dagger}$	5.66	2.87	3.07	2.27	3.32
MnO	0.09	0.04	0.03	0.05	0.06
MgO	2.67	1.14	1.10	1.03	1.16
CaO	0.96	0.45	0.93	2.08	3.26
Na_2O	2.23	2.88	2.99	3.05	4.02
K_2O	1.18	2.26	1.36	2.06	1.23
P_2O_5	0.15	0.11	0.09	0.08	0.17
LOI	3.41	2.41	2.82	3.38	4.34
Total	100.47	100.03	99.93	99.56	100.1

*The samples given here are representative. See Appendix C for full data.
†Total Fe.

TABLE 6. X-RAY FLUORESCENCE RESULTS OF MUDROCKS

Oxide (wt%)	OP40 Sore Thumb	OP35 Elwha-West	OP34 Elwha-East	OP18 Steeple Rock	OP24 Obstruction P.
SiO_2	58.27	60.55	57.88	50.39	61.42
TiO_2	0.86	0.98	0.87	0.71	0.88
Al_2O_3	17.40	16.87	18.02	15.26	17.08
FeO*	8.32	7.98	7.35	6.58	6.47
MnO	0.12	0.10	0.31	0.09	0.02
MgO	2.87	3.66	2.99	2.36	1.94
CaO	0.30	0.38	1.57	9.29	0.92
Na_2O	2.44	2.49	7.86	4.76	2.56
K_2O	2.17	1.81	0.22	1.29	2.47
P_2O_5	0.13	0.20	0.30	0.11	0.69
LOI	6.17	4.50	2.57	9.15	5.65
Total	99.05	99.52	99.95	99.98	100.1

*Total Fe.

TABLE 7. LITERATURE VALUES, SEDIMENTARY ACCRETIONARY PRISM CHEMISTRY

Oxide (wt%)	Otago Schist* (average)	Clastic turbidite[†] (Aleutians)	Terrigeneous[§] (Aleutians)	Pelagic clay[#] (Nankai)
SiO_2	65.4	57.86	61.30	59.72
TiO_2	0.6	0.77	0.72	0.61
Al_2O_3	15.3	15.37	14.52	15.00
FeO**	4.8	5.91	5.28	5.23
MnO	0.1	0.12	0.11	0.59
MgO	1.8	2.96	3.01	2.22
CaO	2.6	2.41	4.77	3.92
Na_2O	3.5	2.85	3.66	1.40
K_2O	2.5	2.40	1.62	3.24
P_2O_5	0.2	0.16	0.11	0.27
LOI	2.5	9.18	4.91	6.25
Total	99.3	99.99	100.01	98.45

*From Breeding and Ague (2002).
[†] Ocean Drilling Project core 183. From Plank and Langmuir (1998).
[§] Ocean Drilling Project core 178. From Plank and Langmuir (1998).
[#] Ocean Drilling Project core 808. From Plank and Langmuir (1998).
**Total Fe.

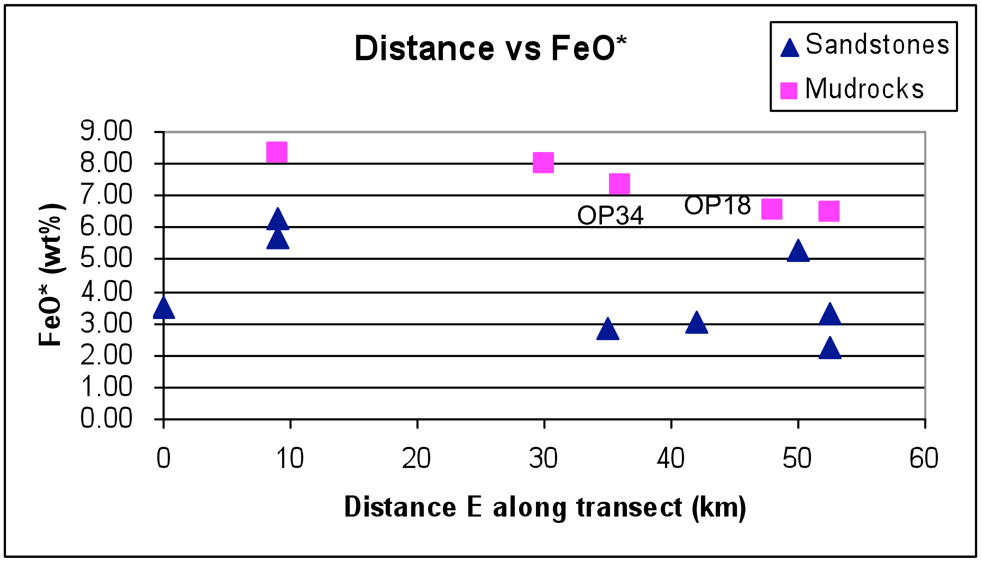

Figure 21. FeO content, sandstones and mudrocks. Compositional outliers OP34 and OP18 are discussed in the text. FeO* is total Fe.

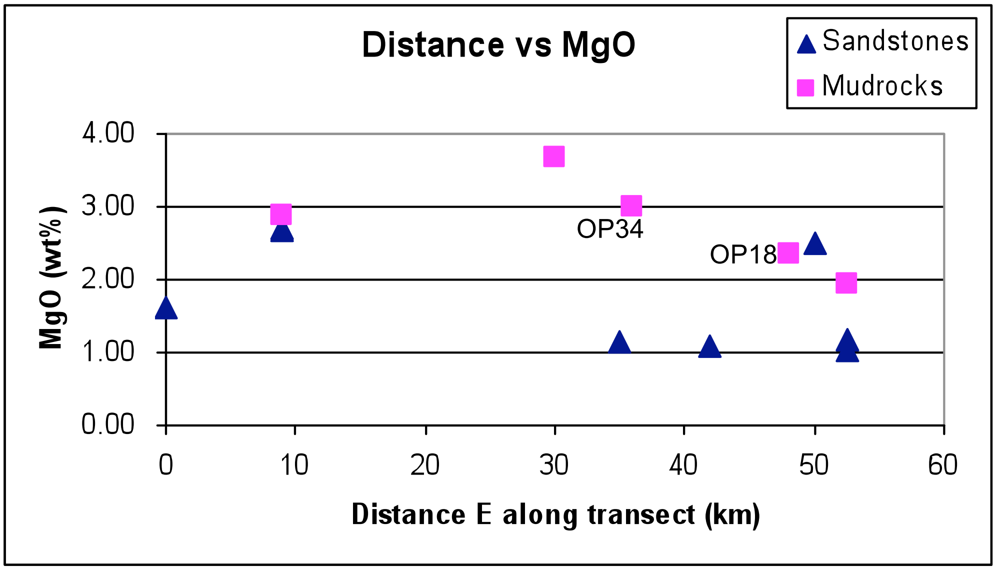

Figure 22. MgO content, sandstones and mudrocks. Compositional outliers OP34 and OP18 are discussed in the text.

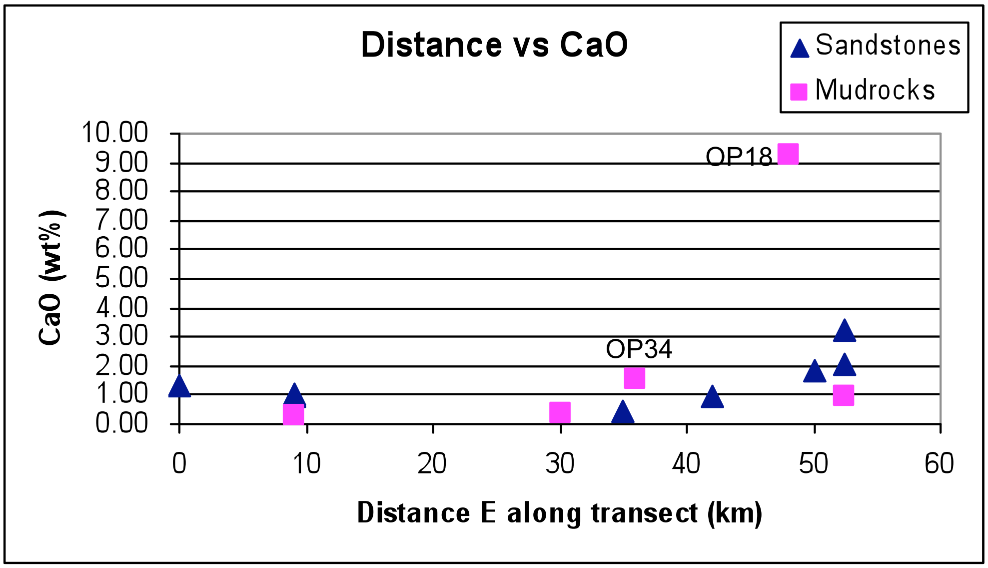

Figure 23. CaO content, sandstones and mudrocks. Compositional outliers OP34 and OP18 are discussed in the text.

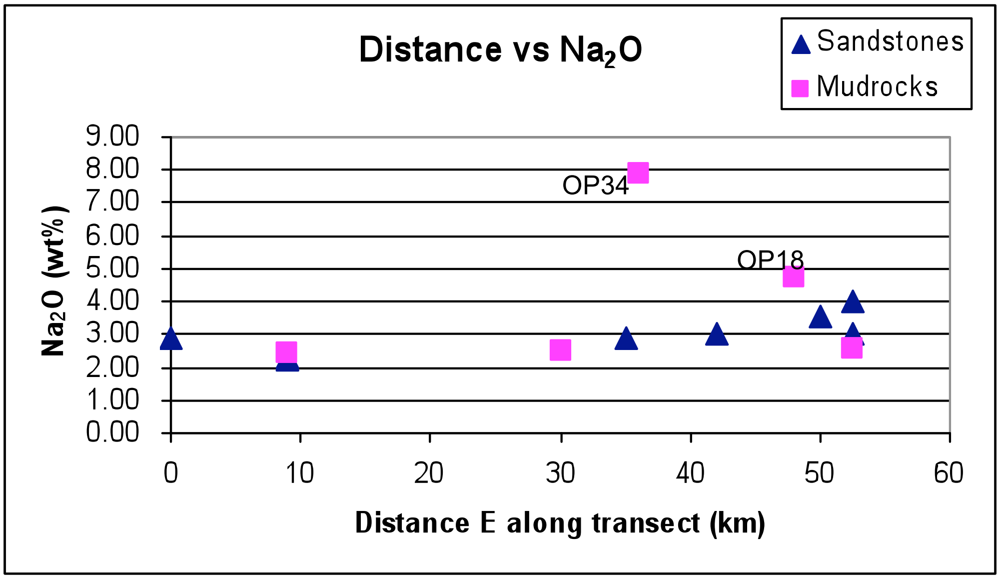

Figure 24. Na_2O content, sandstones and mudrocks. Compositional outliers OP34 and OP18 are discussed in the text.

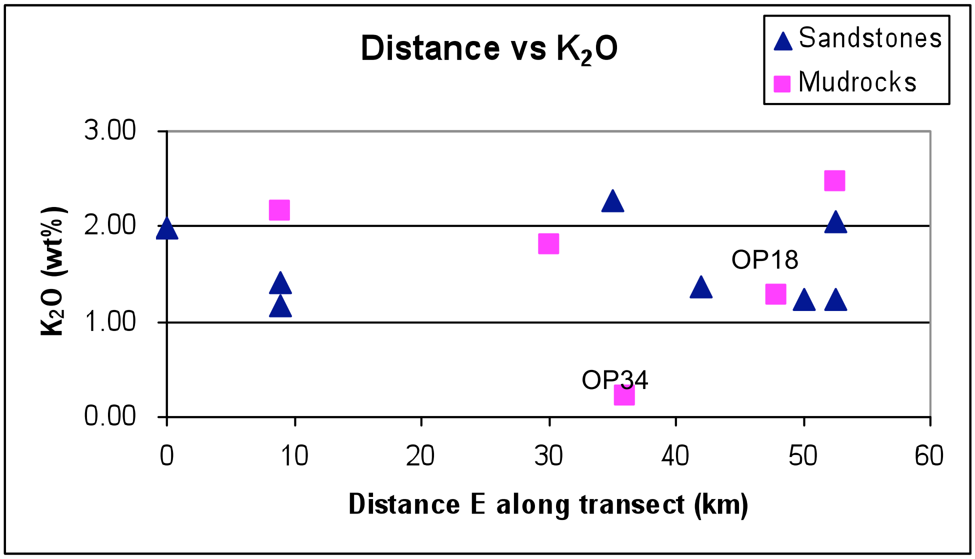

Figure 25. K_2O content, sandstones and mudrocks. Compositional outliers OP34 and OP18 are discussed in the text.

setting fields (Fig. 26A). This is expected for metasedimentary accretionary prism rocks of the Cascadia subduction zone, which is an active margin with a volcanic arc. According to the methodology of Herron (1988), Olympic Peninsula rocks are clustered close to each other in the arkose, wacke, and Fe-shale rock type fields (Fig. 26B), except for slate OP34 (discussed below).

Loss on ignition measurements for use in H_2O budget calculations were also made for all 19 samples analyzed by XRF. However, some samples contain sufficient calcite, usually identified in XRF data via relatively high CaO content, that loss on ignition is not equivalent to H_2O content for all samples. For this reason, H_2O content in sandstones is based on petrographic observations rather than the loss on ignition values presented in Table 5. Most mudrocks contain less CaO than sandstones and the loss on ignition value

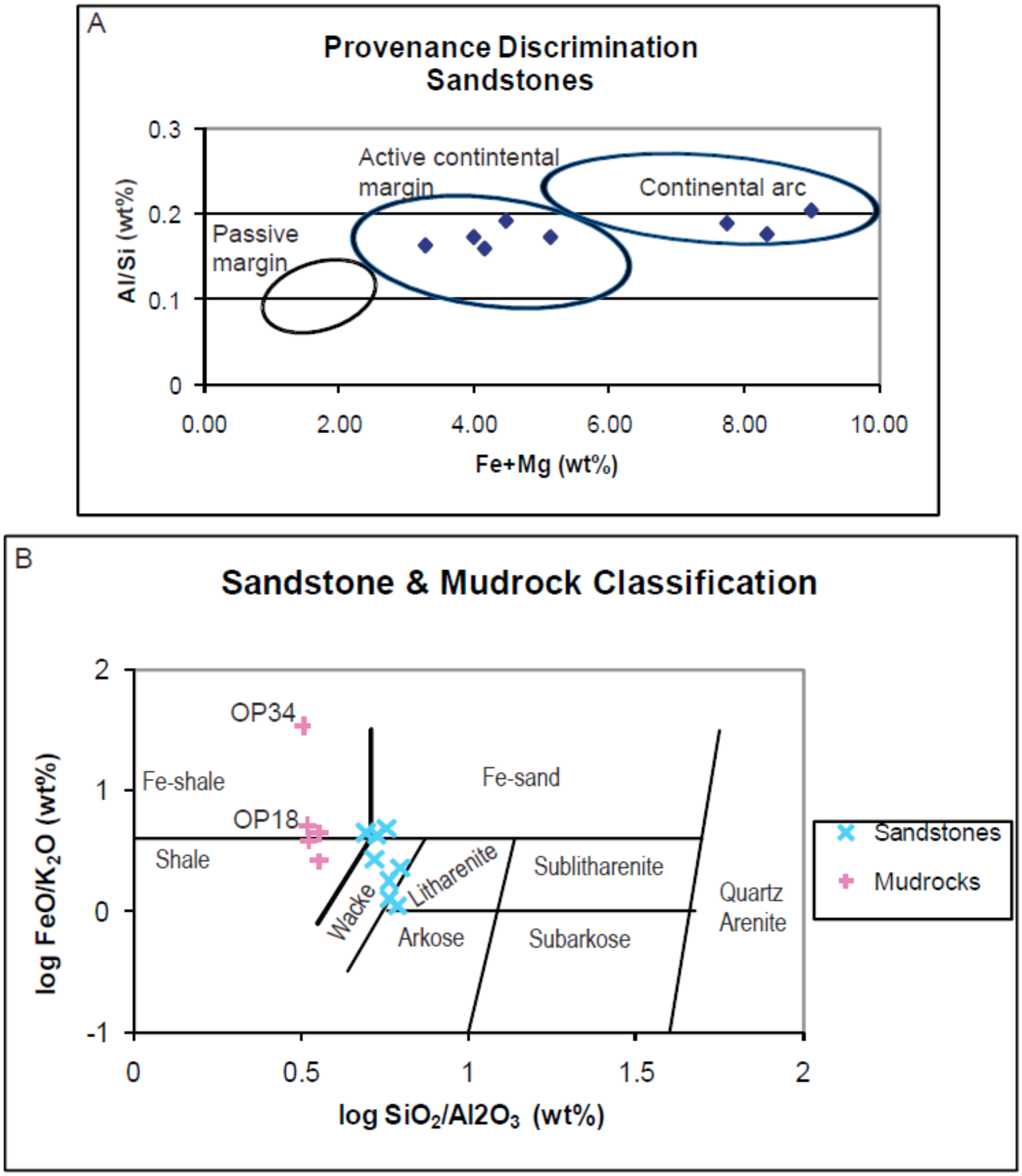

Figure 26. Sandstone provenance and sandstone and shale classification. (A) Provenance discrimination after Bhatia (1983). The oceanic arc field (no samples plotted in this field) is off the graph, to the right of the continental arc field. (B) Sandstone and shale classification after Herron (1988). Four of the five mudrocks plot very close to one another, and all sandstones plot close to one another in the Fe-sand-Wacke-Litharenite fields. Compositional outliers OP34 and OP18 are discussed in the text.

is used as a proxy for H_2O content in the absence of abnormal mineralogy or major element chemistry, as is the case with the exceptions explained below.

Samples Excluded from H_2O Calculations

Sandstone OP41 from Kugel Creek (Fig. 8, Tables 2 & 3) is from a fault-bounded block of the Needles-Gray Wolf lithic assemblage (Tabor & Cady, 1978a), bounded by the Crescent terrane and Western Olympic lithic assemblage. In thin section, OP41 is nearly identical to OP7 from Elwha East in mineralogy and modal abundance of minerals. The LOI value of OP41, 3.37 wt%, and H_2O by petrography, 2.6 wt%, are both intermediate between OP37 at Sore Thumb and OP7 at Elwha East (see Tables 4, 5). Based on these observations, it is possible OP41 was buried to a greater maximum depth than adjacent rocks outside the fault-bounded block. Kugel Creek also lacks a mudrock sample, which is an important component of H_2O content. Therefore, discussion of dehydration in Chapter V will begin at the Sore Thumb site (Fig. 8) on my study transect.

During XRF pellet preparation, the slate sample OP24 from Obstruction Peak (Fig. 8, Tables 2 & 3) was fused a third time because the lab technician ascertained (due to bubbling of pellet) OP24 had a high organic component that did not undergo 100% ignition during the standard 45 min in the muffle oven. The LOI method (Chapter III) used here incorporates ignition of organics and H_2O loss from minerals hydrated by alteration <15 m from the Earth's surface. Consequently, LOI may not accurately reflect the H_2O content of the rock sample. The sample OP24 has normal mineralogy as far as can be ascertained with a standard microscope, but has a higher LOI value than expected for its location on my study transect, possibly due to the high organic content noted by the lab technician. Therefore, the LOI value of OP24 given in Table 6 is not used in calculating the H_2O budget of my study transect.

Slate, basalt, and conglomerate samples from Steeple Rock (Fig. 8, Tables 2 & 3) with post-depositional mineral growth (e.g., chlorite, calcite) in abundances in excess of other samples (Appendix B) on my study transect have abnormal major element chemistry and loss on ignition values (Appendix C). In particular the samples all have very high volatile content compared to samples to the east and west, possibly attributable to the presence of calcite I observed in thin section. The Steeple Rock slate OP18 has high Ca content and shows Na_2O enrichment and K_2O depletion relative to other samples (Fig. 23–25); since K behaves as a large ion lithophile and becomes easily mobile, this may be due to fluid that passed through the rock at some indeterminate point in its history and altered the rock's bulk chemistry. Because of these combined factors from field observations, petrography, and geochemical data, and because Steeple Rock contains basalt thought by previous workers (e.g., Tabor & Cady, 1978b) to have been included in the metasedimentary accretionary prism via faults, the dehydration history of Steeple Rock is suspect and the LOI value of OP18 (Table 6) is not used in calculating the H_2O budget of my study transect.

Slate and basalt samples from Elwha East (Fig. 8, Tables 2 & 3) with abnormal appearance in thin section or post-depositional mineral growth (e.g., chlorite, calcite) in abundances in excess of other samples (Appendix B) on my study transect have abnormal major element chemistry (Appendix C). The slate OP34 from Elwha East is the only slate I examined that contains no identifiable minerals; that is, it is too fine-grained for even 40x magnification to show any minerals. Chemically, OP34 has a high Ca content (except by comparison to OP18) and has the most extreme Na_2O enrichment and K_2O depletion (Fig. 24–25) of any of my samples. Because of these combined factors from field observations, petrography, and geochemical data, and because Elwha East contains basalt thought by previous workers (e.g., Tabor & Cady, 1978b) to have been included in the metasedimentary accretionary prism via faults, the dehydration history of Elwha East is suspect and the LOI value of OP34 (Table 6) is not used in calculating the H_2O budget of my study transect.

Oxygen Isotope Values

In February 2010 I performed replicate analyses of $\delta^{18}O$ on seven samples of vein quartz and one sample of detrital quartz. The primary objective was to distinguish the origin of vein-forming H_2O. Three quartz samples are from the same vein in sample OP28 to test changes in $\delta^{18}O$ as a function of distance from the sandstone host rock and generations of vein growth. Sample OP21 is from a quartz-calcite vein to utilize the geothermometer of quartz and calcite. All samples are from the Obstruction Peak site except for OP12, which is from Hurricane Ridge (Table 2). The vein order of formation represented by OP28 (blocky fill more distal from host rock than fibrous fill) and multi-generation veins were also observed during fieldwork, in other veins in OP3, and other samples (e.g., OP26) for which $\delta^{18}O$ values were not determined due to time constraints.

The results presented in Table 8 are the $\delta^{18}O$ values normalized to a UWG-2 value of +5.8‰ (Valley, 1995). Overall, blocky quartz has a higher $\delta^{18}O$ value than fibrous quartz. The $\delta^{18}O$ values of unknowns range from +11.8 to +15.2‰, with an average standard deviation of ±.7‰ between replicate analyses. Raw values and calibration graphs are presented in Appendix D.

TABLE 8. $\delta^{18}O$ VALUES OF QUARTZ

Site	Sample	Vein Fill	$\delta^{18}O$, Run 1	$\delta^{18}O$, Run 2
Hurricane Ridge	OP12	Blocky	14.9	15.2
Obstruction Peak	OP3	Fibrous	11.6	12.3
	OP20	Fibrous	12.9	11.7
	OP21*	Blocky	14.1	14.5
	OP23-Detrital	N/A	12.6	11.0
	OP28-1†	Fibrous	12.1	13.0
	OP28-2†	Fibrous	13.1	14.4
	OP28-Blo†	Blocky	12.5§	14.4

Note: All values are ‰ and positive relative to standard mean ocean water.
*Sample with quartz-calcite vein, awaiting calcite values.
†Signifies multi-generation vein; 1 is closer to the host rock and blocky is most distal from the host rock.
§Run after extra pumping on line; atmospheric contamination possible.

CHAPTER V

DISCUSSION

In this section I will expand on my results and discuss the broader implications of the H_2O contained in rocks and recorded in quartz veins along my study transect. I address the implications of my $\delta^{18}O$ results, and then explain the structural H_2O content in my study transect and the limitations therein. I discuss the quantity of H_2O likely recorded by the quartz veins at Obstruction Peak, and the conditions influencing that H_2O quantity, before explaining the significance of the H_2O quantity that passed through the rocks as it relates to seismicity. I include comparisons with models and a brief explanation of the factors influencing fluid overpressure. I conclude the section with a comparison between observations of Olympic Peninsula rocks and rocks at megathrust earthquake depths, study limitations, and potential future work.

Significance of $\delta^{18}O$ Values

As a tracer of source and type of fluid movement, my $\delta^{18}O$ results (Table 8) have several possible implications, but the most significant implication of my $\delta^{18}O$ quartz vein values is that the veins have no trace of meteoric or ocean H_2O, and therefore originated at depth, as seen by comparison with the literature values in Table 9. The ranges in reference values are too broad to clearly place the quartz vein fluid origin in a single rock type, but the values are consistent with metamorphic fluid (Taylor, 1967, p. 122). Furthermore, the fibrous vein values, especially OP28-1 (Table 8), are close to the detrital quartz values of OP23, suggesting that early fibrous vein fluid may have originated locally. Relatively late fibrous veins such as OP28-2, which is distal from the host rock

TABLE 9. $\delta^{18}O$ VALUES FROM LITERATURE

Source	$\delta^{18}O$ (‰)
Igneous quartz	9–10
Arkosic sandstone	12–16
Quartz arenite	11–16
Shale	14–19
Basalt/gabbro	6–7
Metamorphic H_2O	10–14
Ocean H_2O*	−.5–.5
Fresh (lake) H_2O*	−10–−4
Meteoric H_2O*	−20–−5
Volcanic H_2O	~7

Note: Values from Taylor (1967, p. 111, 133). All positive relative to standard mean ocean water unless indicated otherwise.

*At surface temperature, not equilibrated with rock.

of OP28 compared to OP28-1, and blocky vein quartz, have slightly higher $\delta^{18}O$ values than earlier or single-generation fibrous veins. Blocky vein quartz $\delta^{18}O$ values are also more homogeneous between runs (Table 8) than fibrous vein quartz. The value of $\delta^{18}O$ is inversely correlated with temperature (O’Neil, 1979, p. 237; Taylor, 1967, p. 220) and oxygen isotopes are known to exchange between 200–300°C (O’Neil, 1979, p. 254). Therefore, temperature may have decreased over the time of vein formation and if an equilibrium mineral pair (e.g., quartz-calcite, quartz-illite) is established the veins of the

Olympic Peninsula could serve as a geothermometer. Regardless of the temperature of vein formation, the vein-forming H_2O originated at depth from rocks and does not have substantial amounts of surface H_2O.

There are several possible interpretations of the change in $\delta^{18}O$ as a function of distance from the host rock and the variation in fibrous vein values in the replicate analyses (Table 8), although heterogeneity of replicates may be an artifact of analysis (see Chapter III). Sandstones, mudrocks, and basalts all have different $\delta^{18}O$ values, so the changes may be a result of changes in input from those three likely sources. Heterogeneous $\delta^{18}O$ values indicate the fluid fractionated by leaving the source rock on expulsion, and homogeneous $\delta^{18}O$ values indicate the fluid infiltrated the rock (Valley, 1986, p. 448). The type of fluid fractionation can also suggest pervasive or channelized fluid flow (Valley, 1986, p. 445). The heterogeneity in my replicates may indicate fibrous $\delta^{18}O$ values are from at least two vein generations instead of one. Determining which of these additional interpretations are correct requires more analytical certainty, as discussed later in this chapter.

Dehydration on the Study Transect

Determination of change in H_2O content along my study transect (Fig. 8) is a key objective of my project. As can be seen in Tables 4, 5, and 6 in Chapter IV, LOI in mudrocks and H_2O content in sandstones varies across the transect in a manner indicative of dehydration, likely with increasing depth (Fig. 27). As discussed in Chapter IV, not all sites are equally reliable. Furthermore, the faulted nature of accretionary prisms means my metasedimentary rock units are likely to be out of sequence. However, once

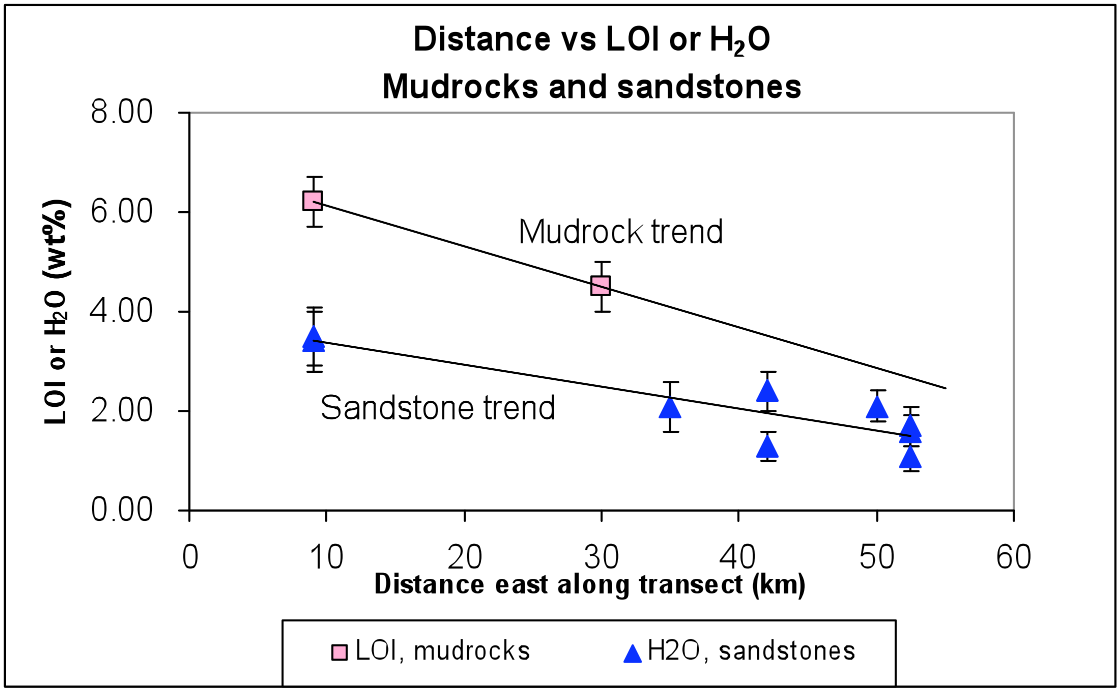

Figure 27. Distance vs. H_2O and LOI, mudrocks and sandstones. Both mudrock and sandstones dehydrate from Sore Thumb at a depth of ~6 km (west end of transect) to Obstruction Peak at a depth of ~14 km (east end of transect).

carbonate and weathering contaminations are taken into account, my study transect demonstrates west to east dehydration.

Extrapolation and Interpolation of H_2O Values

As explained in Chapter IV, the LOI values of slates collected from Elwha East, Steeple Rock, and Obstruction Peak are unreliable as indicators of H_2O content. These sites represent ~40% of the length of my study transect and mudrocks are an important component of the H_2O budget, so I must use a reasonable estimate. A dehydration trend is present between Sore Thumb and Elwha West, so I extrapolate from that trend. Therefore, by extrapolating from the mudrocks in Figure 27, the estimated H_2O contents are 4.0 wt% for OP34 at Elwha East, 3.1 wt% for OP18 at Steeple Rock, and 2.7 wt% for OP24 at Obstruction Peak.

Based on observations of modern sedimentary accretionary prisms (e.g., Rowe & Screaton, 2009) and the observations of Tabor and Cady (1978a) in Table 1, I assume that at depth sandstone and mudrock were each ~50% of rock volume, and the observed dominance of sandstone over mudrocks is due to weathering and study locations. Additionally, where I analyzed sandstones in replicate for a given site (e.g., Obstruction Peak), I incorporated all H_2O values from thin section observations so my results are representative of the entire site.

Quantity of H_2O in Study Transect

Because of the gap in my study transect between Sore Thumb and Elwha West, the unreliability of some samples (see Chapter IV), and other constraints discussed later this chapter, I focus on dehydration between Sore Thumb (west end of transect) and Obstruction Peak (east end of transect). These two sites bracket the ~10 km upper limit of ETS events (Kao et al., 2005). Potential investigations to refine dehydration along my study transect are discussed later this chapter.

To summarize, 1 km^3 at Sore Thumb contains ~10^{11} kg H_2O and 1 km^3 at Obstruction Peak contains ~6×10^{10} kg H_2O (Table 10; Fig. 28). The H_2O remaining at Obstruction Peak depth is available for dehydration at depths >14 km. Note that the quantity of H_2O remaining at Obstruction Peak is approximately half the H_2O at Sore Thumb. Between Sore Thumb, estimated at 6 km depth (Snavely & Kvenvolden, 1989)

TABLE 10. WATER BUDGET

Site	kg H_2O/m^3*	10^{11}kg H_2O/km^3	Loss from 6–14 km depth, 10^{11}kg H_2O/km^3
Sore Thumb	130 ± 22	1.3 ± 0.2	
Obstruction Peak	59 ± 8	.6 ± 0.1	.7 ± 0.1

*This value is based on LOI in Table 6 and Figure 27 and H_2O in Table 4, Figure 27, and Appendix B, assuming rock density of 2700 kg/m^3 and that rock is 50% sandstone, 50% mudrock.

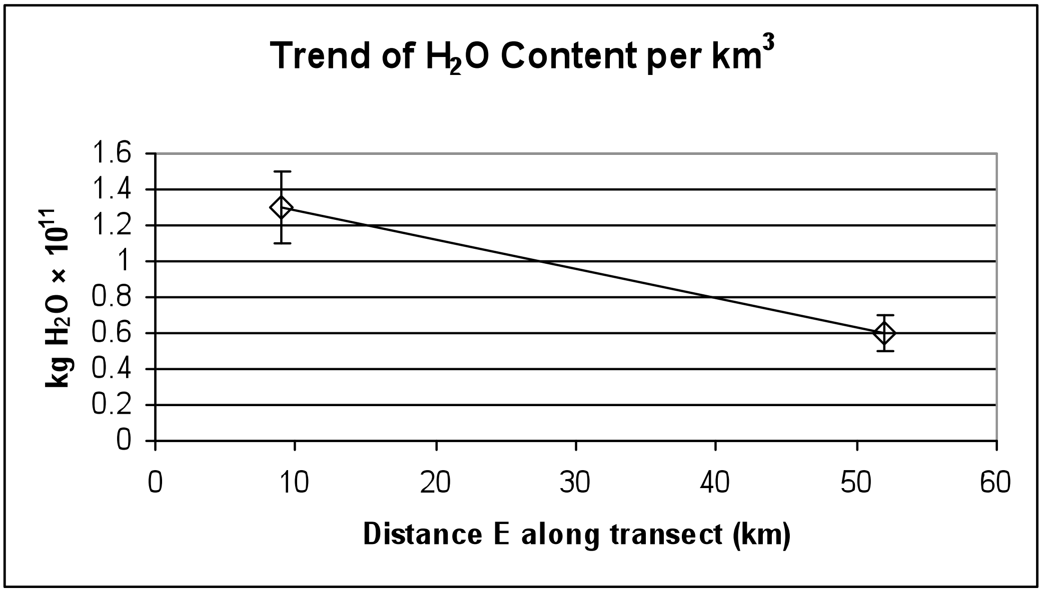

Figure 28. Graphical representation of the total H_2O column in Table 10. The graph is oriented as with all previous graphs, wherein the left end is the western end of the transect and the right end is the eastern end of the transect.

and Obstruction Peak, estimated at 14 km depth (Brandon et al., 1998), ~7 × 10^{10} kg H_2O per km^3 has been expelled from my metasedimentary accretionary prism rocks.

Based on these results, and using a convergence rate of ~40 mm/yr (Wilson, 1988) and a slab dip of ~8° (Davis & Hyndman, 1989), I calculate the burial rate and

H_2O release rate. The convergence rate and slab dip yield a maximum burial rate of 5.6 mm/yr, or 5.6 km/m.y. Based on the maximum burial of ~14 km, the metasedimentary accretionary prism rocks along my study transect were buried for ~2.5 m.y., and were buried from 6–14 km depth in at least 1.5 m.y. Faulting, folding, and other factors may have slowed the burial time by up to a factor of two, to 3 m.y. The rate of H_2O dehydrating from 6–14 km is ~$2 \times 10^4 – 5 \times 10^4$ kg per km of trench per year from sedimentary accretionary prism rocks. This number represents the H_2O dehydrated between Sore Thumb and Obstruction Peak depths, all divided by the burial time range of 1.5–3 m.y. For comparison, Jarrard (2003) estimates a total of 6.46×10^6 kg H_2O per km of trench per year for a depth of 0–50 km for the Cascadia subduction zone. Between 60% and 90% (Vrolijk, 1990; Schact et al., 2008) of dehydration occurs at depths <6 km, which would leave $6.5 \times 10^5 – 2.6 \times 10^6$ kg H_2O per km of trench per year at depths ≥6 km relevant to my study. Based on Bebout (1995), oceanic crust contributes 50–60% of H_2O in subduction zones, so metasedimentary rocks such as those on my study transect, if buried from 6–50 km, might contribute $3.2 \times 10^5 – 1.3 \times 10^6$ kg H_2O per km of trench per year. This range is ~5–25 times greater over a greater depth range than my values given above. Given the limited sample suite I used to determine H_2O content in metasedimentary accretionary prism rocks from the Cascadia subduction zone, my results compare favorably to those expected from Jarrard (2003).

Veins and Fluid Movement

As explained in Chapter IV, quartz ± calcite ± chlorite veins are present at Hurricane Ridge and Obstruction Peak sites as a minor outcrop component, although abundance was only measured at Obstruction Peak. At Obstruction Peak, quartz veins compose 0.5–1% of outcrop and are primarily present in sandstone (Fig. 10, 11, Appendix A), and several implications arise from these data and observations. Using experimentally established quartz solubility values for SiO_2-H_2O and SiO_2-H_2O-CO_2-NaCl mixtures and density of H_2O at varying temperature and pressure conditions (Halbach & Chatterjee, 1982; Manning, 1994; Akinfiev & Diamond, 2009), I determined the solubility of quartz and quantity of H_2O required to deposit the observed vein volume at estimated conditions of 250°C and ~5 kbar (Brandon et al., 1998). Quartz solubility is relatively insensitive to changes in pressure, so the main control is temperature (Manning, 1994). Figures and graphs relevant to my solubility calculations are provided in Appendix E.

An important consideration is that quartz is sufficiently soluble at conditions of 250°C and ~5 kbar that not all quartz will precipitate out of solution. For every 100°C change, quartz solubility changes by as much as a factor of 3–4. For example, at 250°C and ~5 kbar, quartz solubility is 0.08 wt% in a SiO_2-H_2O mixture, but at 150°C and 1.5 kbar, quartz solubility is 0.02 wt% in a SiO_2-H_2O mixture. Furthermore, adding NaCl and CO_2 to the SiO_2-H_2O mixture reduces quartz solubility by a factor of 2–3. For example, at 250°C and ~5 kbar, quartz solubility decreases from 0.08 wt% for a SiO_2-H_2O mixture to 0.03 wt% for a SiO_2-H_2O-CO_2-NaCl mixture.

Using my observations of vein abundance as discussed in Chapter IV and literature values of quartz solubility, I calculate multiple scenarios for the quantity of H_2O recorded by quartz veins at Obstruction Peak. Components used in my calculations, and the results given below, are summarized in Table 11. Quartz is more soluble in a SiO_2-H_2O mixture, so that scenario will represent a minimum estimate of H_2O required to form the vein abundance I observed at Obstruction Peak, and since quartz solubility is lower in a SiO_2-H_2O-CO_2-NaCl mixture that scenario represents an approximate maximum quantity of H_2O required. The simplest scenario is a SiO_2-H_2O mix at 250°C and ~5 kbar where all the quartz precipitated out of solution (Scenario A in Table 11). From a SiO_2-H_2O mixture, 1 m^3 rock containing 0.5–1% quartz veins records the passage of $\sim 3 \times 10^4$ kg H_2O. Based on my results as discussed in Chapter IV, it is reasonable that the mixture was SiO_2-H_2O-CO_2-NaCl. Calcareous cement is fairly abundant in sandstones and I observed calcite in veins at Obstruction Peak, so I assume CO_2 is more abundant in the mixture than NaCl, and therefore I estimate component fractions are 0.9 H_2O, 0.08 CO_2, and 0.02 NaCl. Based on Akinfiev and Diamond (2009), quartz solubility is more sensitive to the presence of the added components than their exact fraction in the mixture.

TABLE 11. COMPONENTS FOR VEIN H_2O CALCULATIONS

Component	SiO_2-H_2O, A	SiO_2-H_2O, B	SiO_2-H_2O-CO_2-NaCl, A	SiO_2-H_2O-CO_2-NaCl, B
Temperature (°C)	250	400–200	250	400–200
Solubility (wt% SiO_2)	0.08	0.16	0.03	0.02
$Solubility^{-1}$	1250	625	3333	5000
kg H_2O flow /m^3 rock	$2.5 \pm 0.8 \times 10^4$	$1.3 \pm 0.5 \times 10^4$	$6.7 \pm 2.3 \times 10^4$	$1 \pm 0.3 \times 10^5$

Note: Constants for all calculations are rock density of 2700 kg/m^3, and 20 ± 7 kg quartz per m^3 rock. See text and Appendix E. In scenarios involving a temperature change, the difference in solubility is given. Temperature established, the relevant calculation to determine line 4 is $20 \pm 7 \times Solubility^{-1}$.

From the SiO_2-H_2O-CO_2-NaCl mixture, 1 m^3 rock containing 0.5–1% quartz veins records the passage of 7×10^4 kg H_2O if all the quartz precipitated out of solution.

What quantity of H_2O is recorded in the quartz veins if not all the quartz precipitated out of solution during vein formation? This is Scenario B in Table 11. If the source H_2O for the veins flowed updip from release at ~400°C, where many dehydration reactions are likely to occur (Hacker, 2008) and all the quartz has precipitated by ~200°C, which is the minimum temperature I expect at Obstruction Peak based on Brandon et al. (1998), then in a SiO_2-H_2O mixture 1 m^3 rock containing 0.5–1% quartz veins records the passage of ~1.3×10^4 kg H_2O. Under the same conditions for the SiO_2-H_2O-CO_2-NaCl mixture, 1 m^3 rock containing 0.5–1% quartz veins records the passage of up to ~10^5 kg H_2O.

My results mean that over the time of vein formation, H_2O to rock ratios were well in excess of 1:1 (Fig. 29). If there was 1 km^3 (2.7×10^{12} kg) of rock with 0.5–1% quartz vein at Obstruction Peak prior to erosion, which is a reasonable estimate based on field observations, ~10^{13} – 10^{14} kg H_2O flowed through the 1 km^3 to form quartz veins. Carbonate cement and calcite veins are also present at Obstruction Peak, so I estimate the minimum H_2O required to form the veins is likely an intermediate value of ~8×10^{13} kg in 1 km^3, even if all quartz precipitated out of solution during vein formation. The assumption that all quartz precipitated from solution is simplistic and means all the H_2O flow estimates presented here are minimum to intermediate.

Therefore, far more H_2O flowed through 1 km^3 at Obstruction Peak than has been forced out of hydrous minerals in 1 km^3 between Sore Thumb and Obstruction Peak

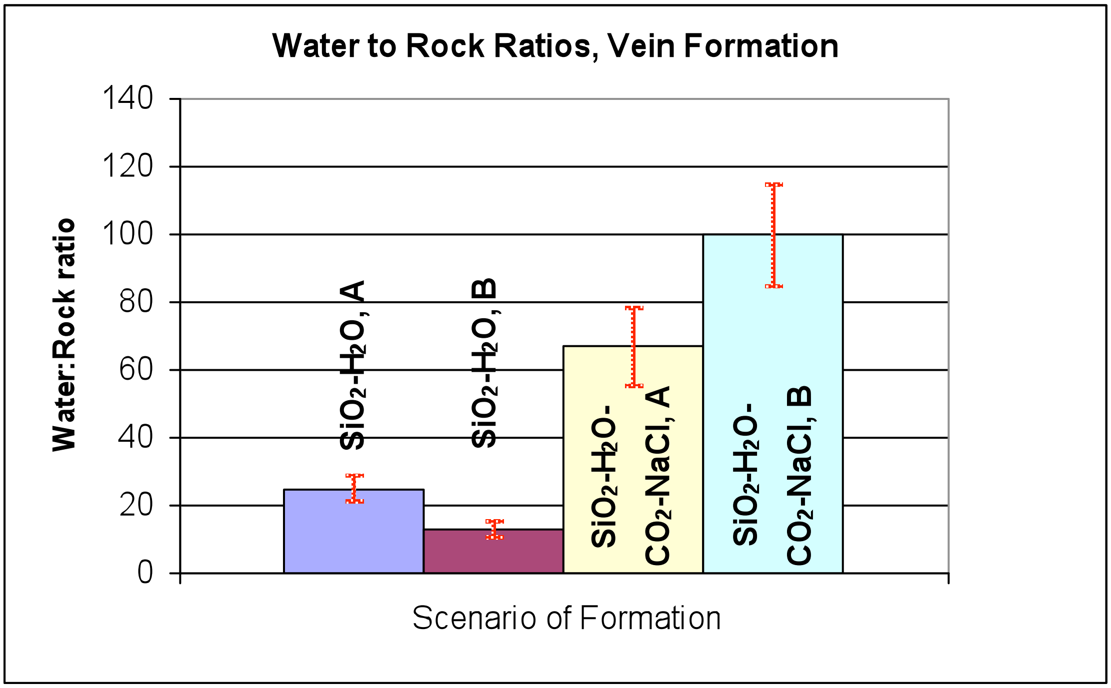

Figure 29. Representation of the volume of water to rock ratios during vein formation. Scenarios are the same as for Table 11 and the text. Relative volume refers to the volume of H_2O passing through 1 m^3 rock, so the SiO_2-H_2O Scenario A mixture equals a ~25:1 water:rock ratio by volume.

depths, so it is very likely large quantities of fluid are being generated at depths >15 km and moving updip. For example, 1 m^3 rock at Obstruction Peak contains 59 ± 8 kg structural H_2O (Table 10), so I calculate ~200–1900 m^3 of Obstruction Peak or equivalent rock needed to completely dehydrate to produce 1 m^3 of rock with 0.5–1% quartz veins at Obstruction Peak. This range in rock volume excludes contributions from oceanic crust dehydration. The quantity of rock required to dehydrate to produce the observed quantity of veins suggests a strong degree of channelization.

Alternative to or in combination with large quantities of H_2O release at depths >14 km, it is likely based on Screaton et al. (1990) that some of the H_2O released at depths <14 km is unable to escape updip and is transported to a depth greater than where it was released. This is due to relatively low flow velocities in sedimentary accretionary prisms (see below) and therefore a somewhat smaller volume of rock would need to dehydrate to produce the observed vein abundance. For example, 1 m^3 of rock at Sore Thumb contains 130 ± 22 kg H_2O (Table 10), so I calculate ~100–900 m^3 of Sore Thumb or equivalent rock needed to completely dehydrate to produce 1 m^3 of rock with 0.5–1% quartz veins at Obstruction Peak. Because the rocks may not dehydrate entirely before reaching depths at which released H_2O no longer flows updip, I estimate the volume of rock required to dehydrate and produce 1 m^3 rock with 0.5–1% quartz veins to be an intermediate range of 400–900 m^3. Therefore, it seems likely pervasive fluid carried down with the rocks and channelized fluid flow played a role in vein formation, and/or oceanic crust dehydration is an important component of H_2O flowing updip to form quartz veins such as those at Obstruction Peak (Fig. 30).

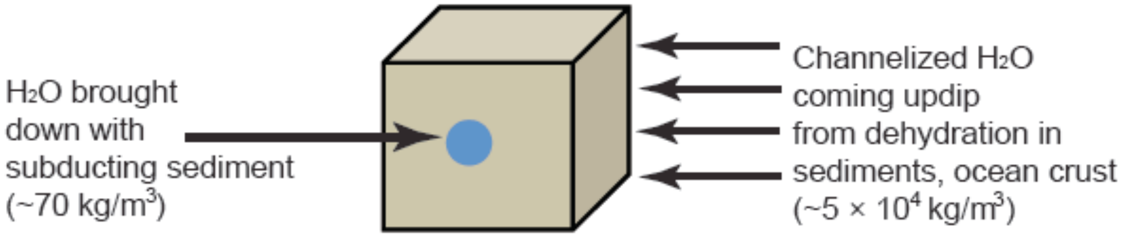

Figure 30. Schematic of H_2O input, Obstruction Peak veins. Relatively little H_2O (blue dot) is carried down with the rock (see text for rock volume requirements), so channelized H_2O from downdip dehydration reactions in the sedimentary rock and/or oceanic crust must play a substantial role.

Fluid Overpressure and Seismicity

Fluids present in great enough quantities to produce fluid overpressure and reduce friction along fault planes can result in earthquakes (e.g., Shelly et al., 2006), so the rate of fluid release and permeability of surrounding rock are important quantities to constrain. Fluids preferentially concentrate in relatively high-permeability sandstones (e.g., Rowe & Screaton, 2009) where flow is easier than in low-permeability mudrocks. Sandstones can still achieve fluid overpressure due to permeability contrasts with surrounding rock, which is a major control on the generation of fluid overpressure (e.g., Saffer & Bekins, 1998).

However, field observations at Obstruction Peak may indicate favorable conditions for generating fluid overpressure: sandstone and mudrocks are interbedded on the scale of mm to m, and fibrous crack-seal veins concentrated almost exclusively in sandstones are the main type of quartz vein. Interbedding effectively traps the fluid by limiting directions for pervasive flow, increasing the likelihood of fluid overpressure and channelized flow. To review from Chapter II, fibrous veins are common at relatively deep conditions not favorable to maintaining void space, but where rock will, at fluid overpressure conditions, fracture long enough for fluid to rush in and deposit fibrous quartz, closing the fracture until sufficient fluid and therefore pressure builds up again (Fig. 7).

Is the quantity of vein fluid recorded at the Obstruction Peak site then sufficient to generate fluid overpressure based on experimental and modeling data of sedimentary accretionary prisms, and is the structural H_2O released across my study transect sufficient to generate fluid overpressure on its own? This depends on the burial rate of Olympic Peninsula rocks and the time it took the accretionary prism material to reach the maximum depth of ~14 km (Brandon et al., 1998). The Olympic Peninsula rocks took 2.5–5 m.y. to be buried from 0–15 km depth, and ~1.5–3 m.y. to travel 6–14 km depth; see earlier this chapter for explanation. To review from earlier this chapter, structural H_2O dehydrated at ~$2 \times 10^4 - 5 \times 10^4$ kg H_2O per km of trench per year from 6–14 km depth. If veins were formed over 1.5 m.y., H_2O recorded in veins at Obstruction Peak flowed at ~$10^6 - 10^7$ kg H_2O per km of trench per year. This range likely represents minimum to intermediate flow rate values rather than maximum flow rates, since vein formation was probably restricted to the deeper levels of the prism.

There are no modeled or measured values of fluid flow at depth in the Cascadia sedimentary accretionary prism to which I can compare my results, but there are models from the Barbados and Nankai sedimentary accretionary prisms (Screaton et al., 1990; Saffer & Bekins, 1998) for H_2O flow and expected conditions for fluid overpressure in sedimentary accretionary prisms. These studies focused on H_2O flow and fluid overpressure at shallower depths (and therefore higher permeability) in the sedimentary accretionary prism than my project, but since H_2O dehydrated from or flowing through my rocks flowed updip to shallower levels (Jarrard, 2003), they are still relevant. Of the two studies, drill core data indicate the composition of the Nankai sedimentary accretionary prism is more equivalent to the Cascadia sedimentary accretionary prism (Plank & Langmuir, 1998; Normark & Reid, 2003). In the Barbados sedimentary accretionary prism, H_2O flow is modeled at 9.24×10^6 kg per km of trench per year

(Screaton et al., 1990), assuming a model boundary at <2 km depth. In the Nankai sedimentary accretionary prism, H_2O flow is modeled at $2 \times 10^7 - 2 \times 10^8$ kg per km of trench per year (Saffer & Bekins, 1998), assuming a model boundary at ~7 km maximum depth. The Saffer and Bekins (1998) results are more relevant due to the greater depth limit of their model and the compositional similarity of the Nankai sedimentary accretionary prism to the Cascadia sedimentary accretionary prism. However, because my observations are at depths up to ~14 km, the model of Saffer and Bekins (1998) should be regarded as providing an upper limit to the quantity of H_2O required to generate fluid overpressure.

Fluid flow velocities in sedimentary accretionary prisms are quite slow, only 0.03–30 mm/yr, and in most of the sedimentary accretionary prism velocities are ~0.3 mm/yr; only in the décollement and underthrust parts of the sedimentary accretionary prism does H_2O flow faster (Screaton et al., 1990). This means that in 1.5–3 m.y. it is likely H_2O released from 6 km depth would move <1 km toward the toe of the sedimentary accretionary prism as the sedimentary accretionary prism rocks move 4–8 km downward, and therefore structural H_2O released at 6 km depth could contribute to fluid overpressure at greater depths such as ~14 km depth at Obstruction Peak. However, fluid flow velocities in the Olympic Peninsula metasedimentary accretionary prism rocks may have been somewhat faster and drained H_2O more rapidly before fluid overpressure could develop.

Based on these results, there are strong indicators Olympic Peninsula rocks achieved fluid overpressure conditions, particularly at sites such as Obstruction Peak.

The existence of fibrous quartz veins, the formation and existence of which was described in Chapters II and IV, demonstrates fluid overpressure was achieved (van der Pluijm & Marshak, 2004, p. 160). Furthermore, my results and the results of Saffer and Bekins (1998) compare favorably with each other, so fluid overpressure was definitely achieved at Obstruction Peak.

Is there sufficient fluid release in Olympic Peninsula rocks to trigger seismicity? Fluid overpressures result in a decrease in shear strength of the rock, and this leads to weakening and easier deformation of the rock (Byrne & Fisher, 1990; Shelly et al., 2006; Moore et al., 2007). Large quantities of fluid moving through rock can also generate seismic signals, as has been documented at volcanic systems (McNutt, p. 1019, 2000). The characteristics of the fluid, fluid conduit, and the surrounding rock, such as conduit length, mass and stiffness of the rock, and velocity and viscosity of the fluid all determine whether tremor can be generated by fluid (Julian, 1994). The fluid moving through rock scenario is similar to ETS events, where high V_p/V_s ratios and therefore areas of high fluid pressure have been documented (e.g., Shelly et al., 2006). ETS events could also be generated when rock is more easily deformed by lowering of shear stress (excess fluid), though this scenario is also what generates ‘common’ earthquakes such as megathrust ruptures (Moore et al., 2007). Field and petrographic evidence of crack-seal veins and multiple generations of vein formation strongly indicate the rocks of Obstruction Peak were subjected to sufficiently high fluid pressure to result in favorable conditions for seismicity.

Olympic Peninsula as a Record of Megathrust Earthquakes?

As addressed briefly in Chapter II, it is likely the Olympic Peninsula represents a metasedimentary accretionary prism exhumed from megathrust depths: (1) temperatures are within the 150–350°C (Snavely & Kvenvolden, 1989; Brandon et al., 1998) range at which megathrust earthquakes occur (Moore et al., 2007); (2) samples from Obstruction Peak exhibit both brittle and ductile deformation characteristic of the upper temperature range for megathrust earthquakes (see Chapter IV; Moore et al., 2007); (3) outcrop at Obstruction Peak contains a combination of carbonate cement (rock-strengthening) and quartz veins (record of rock-weakening H_2O movement) with the potential to produce megathrust earthquakes (see Chapter IV; Moore et al., 2007); and (4) fault rocks in the Nobeoka Thrust in Japan and in Kodiak Island, Alaska that reached megathrust conditions (Kondo et al., 2005; Rowe et al., 2009; Meneghini et al., 2010) resemble rocks at equivalent conditions on the Olympic Peninsula (Fig. 31).

I address some of the above observations and their implications in more detail in the following paragraphs, since they have substantial implications for the pre-exhumation history of the Olympic Peninsula and serve as an impetus to some of the future work proposed at the end of this chapter.

Carbonate cement, which I observed to be fairly common in sandstones at Obstruction Peak and localized at some other sites (e.g., Elwha East, Kugel Creek), increases rock strength and decreases porosity. The implication that carbonate cementation increases a rock's ability to produce earthquakes by strengthening the rock (Moore et al., 2007) is not entirely intuitive, but rocks not easily deformed are essential

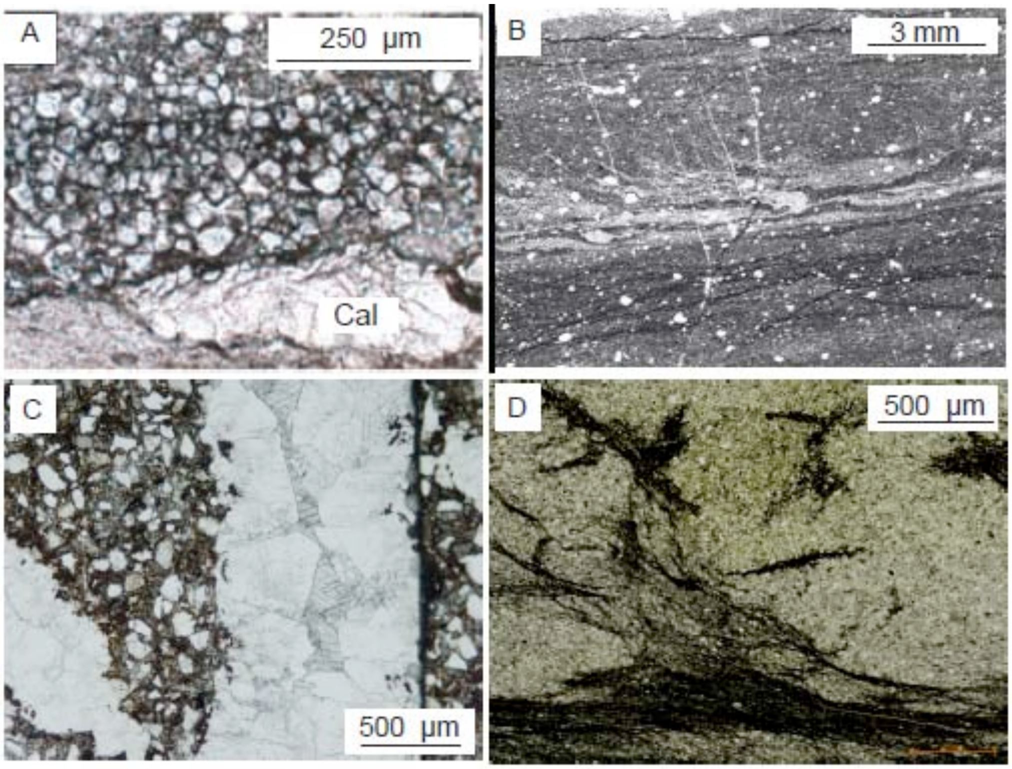

Figure 31. Comparison of seismogenic zone rocks. (A) Microphotograph, plane polars, cataclastic quartz grains (upper two-thirds of photo) and carbonate deposition (Cal) from Hyuga Group at ~250°C, Nobeoka Thrust, Japan. After Kondo et al. (2005). (B) Microphotograph, plane polars, showing laminations, granular quartz, and flow banding, fault rocks, Kodiak Island, Alaska. After Meneghini et al. (2010). (C) Microphotograph, plane polars, 5x, sample OP21, Obstruction Peak. Quartz grains (colorless) in carbonate cement and matrix (brown to red) have a similar appearance to quartz grains in (A). (D) Microphotograph, plane polars, 5x, sample RWT-174-64, 7 km E of Obstruction Peak, with laminations, pressure solution, and possible flow structure. Section courtesy R.W. Tabor.

for large earthquakes. Only strong rocks will fail brittlely and catastrophically enough to produce megathrust events. Furthermore, decreasing a rock's porosity increases its fluid overpressure potential, again leading to earthquakes.

Quartz veins and dissolution and recrystallization of quartz also have implications for rock behavior. At ~200–300°C, quartz is velocity weakening, and has stick-slip behavior (Moore et al., 2007; Schwartz & Rokosky, 2007). This means that any sliding within the rock is unstable, and elastic strength may be stored until the rock fails, similar to the implications of carbonate cementation. Dissolution and recrystallization of quartz may magnify stick-slip behavior (Moore et al., 2007). Fluid overpressure and fluid movement, which I observed via quartz veins (e.g., Obstruction Peak site), contribute to earthquake generation by causing fractures and/or decreasing shear strength locally (Fisher & Brantley, 1992; van der Pluijm & Marshak, p. 160, 2004; Shelly et al., 2006), which may propagate to a large-scale failure (hundreds of km) of the megathrust fault system.

Brittle and ductile deformation can usually be distinguished straightforwardly in rocks. Ductile deformation takes place via pressure solution, especially at megathrust earthquake conditions (e.g., Moore et al., 2007) relevant to my rocks. Some Obstruction Peak samples show pressure solution (ductile), as in Figure 20B. The fault plane in Figure 20C is indicative of brittle deformation, so sample OP3 at Obstruction Peak records brittle and ductile deformation on the mm scale. Moore et al. (2007) note that this combination is relatively common in rocks from the middle and upper seismogenic temperatures at 200–300°C.

Study Limitations

As with any study, my project has limitations that are evident in the field and in sample analysis. I address some specific limitations in Chapter IV. Overall, the limitations are linked to rock type, to petrography, and to the nature of this study as a reconnaissance investigation.

Basalt is a very minor component of Olympic Peninsula outcrop, but it was a potential rock of interest. However, the basalts record fluid infiltration events, potentially prior to incorporation into the metasedimentary accretionary prism, that greatly alter their mineralogy and chemistry. Because of these events, the basalts are not used to determine metamorphic grade or in the dehydration trends.

Two main limitations are observed from thin section observations. The two sandstones from Sore Thumb are rich in lithics and polycrystalline quartz and depleted in phyllosilicates relative to the other sandstones on my study transect. This difference increases the uncertainty of the sandstone dehydration trend, since it is based on the assumption that the rocks are fairly similar, which is the case geochemically but not petrographically. An additional concern for all sandstones is that many fine-grained minerals are present that cannot be identified by standard methods, and due to time and budgetary constraints these fine-grained minerals were not identified via X-Ray diffraction or electron microprobe. Therefore, I increased the uncertainties in mineral abundance estimates (see Table 4) to account for the lack of fine-grained mineral assemblage for my samples.

The program timeline and budgetary constraints also reduced the number of samples I could analyze. There are replicate sandstones from some sites, but not all, and no replicate mudrock samples. Collection of additional samples would reduce the uncertainty of the dehydration trends in mudrocks and sandstones.

Future Work

Additional studies of exhumed sedimentary accretionary prisms are important because the sedimentary accretionary prism rocks may span the megathrust and ETS depths of the subduction zone depending on depth of burial prior to exhumation. As ETS events are a relatively recently discovered process that has an impact on the better known megathrust earthquake potential in subduction zones (Rogers & Dragert, 2003), ETS conditions of occurrence have the potential to help us better understand subduction zone processes.

Shallowly buried sedimentary accretionary prisms are useful for future studies as well because they may have recorded megathrust events during burial prior to exhumation. Olympic Peninsula temperature and depth constraints are within the zone of megathrust earthquakes (Moore et al., 2007; Meneghini et al., 2010), and field and petrographic observations from my project are not dissimilar (Fig. 31) to those from studies of megathrust zone rocks in Japan and Alaska (Kondo et al., 2005; Meneghini et al., 2010). It is therefore possible the rocks of the Olympic Peninsula represent a unique window into past megathrust earthquakes of the Cascadia subduction zone.

Additional studies connecting H_2O in sedimentary accretionary prisms to seismicity are therefore worth pursuing. The approach and site selection for any such study would depend on whether the target seismicity was megathrust earthquakes or ETS events. However, an exhumed sedimentary accretionary prism that is better mapped (or has the potential to be well-mapped) and well exposed compared to the Olympic Peninsula would make a more ideal location for future work. Choosing an exhumed sedimentary accretionary prism with already established isobars and isotherms would increase the efficiency of the study and accuracy of potential results. An ideal future study of the connections between sedimentary accretionary prism dehydration, H_2O movement, and earthquakes would involve an exhumed margin with (1) exposed burial depths of 5–30 km (greater than this study); (2) a high (>15%) proportion of outcrop per square km; (3) well-documented geologic units and thermal and pressure constraints; and (4) subaerial exposure of the subducting plate, so the interface between accretionary prism and oceanic plate, where subduction zone seismicity is concentrated, can be examined.

If the Olympic Peninsula is studied again, there are many possibilities for projects, from a direct continuation of my project to structural studies. There are options for projects focused on either lab or field work, and for approximately 12 undergraduate and graduate students interested in stable isotopes, petrography, geochemistry, and structural geology. Project budgets range from ~$500 to ~$3000, based on 2009 costs. Potential projects are summarized in Table 12. Project 1 is the next logical step, but beyond that the order of projects are not dependent upon one another, and some may be conducted simultaneously.

An important consideration for future work on the Olympic Peninsula is that the last known published structural study of the entire Olympic Peninsula took place from 1961–1972 (Tabor & Cady, 1978b), which overlaps with the acceptance of plate tectonics in the geologic community. Consequently, although the final publications accept the existence of the Cascadia subduction zone and accept the Olympic Peninsula as an

TABLE 12. POTENTIAL FUTURE PROJECTS, OLYMPIC PENINSULA

Project	Objectives	Methods	Timeline	Budget	Potential advisor(s)
1*	Fill 20-km gap in transect of this study Collect 10 – 15 samples Determine H_2O content of mudrocks	Fieldwork: Hike from Boulder Creek Trailhead to Sol Duc Trailhead via Appleton Pass, also via Bogachiel Peak if needed (16 – 24 miles) XRF & standard petrography of new samples Electron microprobe (EMP) of existing, new samples X-Ray diffraction of existing, new samples	Two-year M.S.: Year 1: Analyze existing samples OR fieldwork prior to arrival at CWU Year 2: Analysis of new samples Alternative: Two or more undergraduate projects	Fieldwork: 2 people at $25/day, 5 days Mileage: $.50/mi, 860 miles for fieldwork & lab analysis travel XRF: $100 ($10/sample) Thin sections:~$150 (~$17/sample) EMP: $1000 - $1500 (2 – 3 days) X-Ray diffraction: $0	Mattinson
2	Determine $\delta^{18}O$ for detrital quartz, other minerals Determine $\delta^{18}O$ for quartz veins, this study, plus additional quartz veins, this study Determine $\delta^{18}O$ of detrital, vein samples from Project	Mineral separation & treatment for detrital minerals Preparation of vein quartz from Project 1 Oxygen isotope vacuum line (silicate), gas bench (calcite)	Two-year M.S.: Year 1: Sample preparation Year 2: Analyze samples in summer Alternative: Undergraduate project A to run replicates, this study Undergraduate project B to run detrital, Project 1 samples	Mileage: $.50/mi, 360 miles $\delta^{18}O$ analysis: ~$500 (~5 days analysis)	Gazis

TABLE 12, CONTINUED

Project	Objectives	Methods	Timeline	Budget	Potential advisor(s)
3a*	Look for evidence of megathrust earthquakes (see Meneghini et al., 2010) Locations: Hurricane Ridge & Obstruction Peak sites, this study	Structural observations: D1, S1 deformation & fabric, etc. Bedding & vein measurements (Brunton compass) Petrographic observations of deformational indicators (M.S.) Scanning electron microscope (SEM)	Undergraduate: Discuss with advisor in spring, find field partner, fieldwork over summer Two-year M.S.: Similar timeline, to be adjusted according to field experience	Fieldwork: 2 people at $25/day, 5 – 7 days Mileage: $.50/mi, ~500 miles Thin sections: ~$200 (~$17/sample) SEM: ~$1000 (2 days)	Rubin or Lee
3b*	Look for evidence of megathrust earthquakes (see Meneghini et al., 2010) Locations: Follow Hurricane Ridge and Gray Wolf faults along strike, going east from Hurricane Hill area	Structural observations: D1, S1 deformation & fabric, etc. Bedding & vein measurements (Brunton compass) Petrographic observations of deformational indicators SEM	Two-year M.S.: Year 1: If 3a completed first, review findings Year 2: ~4 weeks of fieldwork, sampling in summer, petrography in fall	Fieldwork: 2 people at $25/day, 28 days Mileage: $.50/mi, ~500 miles Thin sections: $300 – $600 (~$17/sample) SEM: ~$1000 (2 days)	Rubin or Lee

TABLE 12, CONTINUED

Project	Objectives	Methods	Timeline	Budget	Potential advisor(s)
4a*	Map and sample east-west transect through Mount Olympus vicinity, parallel to transect this study Map units of Olympic core in greater detail than Tabor & Cady (1978a)	Structural observations and measurements as in Projects 3a & 3b Collect representative sample suite (~60 samples)	Two-year M.S.: Year 1: prepare for fieldwork, and/or some fieldwork prior to 1st quarter at CWU Year 2: 8 – 12 weeks fieldwork in summer, compilation of map & observations in fall	Fieldwork: 2 – 3 people at $25/day, 56 – 84 days Mileage: $.50/mi, ~500 – 1000 miles	Mattinson/Rubin or Mattinson/Lee
4b	Utilize samples from Project 4a to find H_2O content as with this study and Project 1	XRF, as with this study Petrography, as with this study EMP, as with Project 1 X-Ray diffraction, as with Project 1 Stable isotope analysis, as with this study, Project 2	Two-year M.S.: Year 1: Cut thin sections, prepare samples for other analyses Year 2: Beginning in summer, conduct petrographic observations, conduct microprobe & other analyses Undergraduate option/supplement: Conduction stable isotope analysis (including detrital)	Mileage: $.50/mi, 360 – 800 miles for lab analysis travel Thin sections: $500 (~$17/sample) XRF: $300 ($10/sample) EMP: $1500 (3 days) X-Ray diffraction: $0 $\delta^{18}O$ analysis: $400	Mattinson/Rubin or Mattinson/Lee

TABLE 12, CONTINUED

Project	Objectives	Methods	Timeline	Budget	Potential advisor(s)
5*	Determine connection between basalt in Olympic core & Crescent Formation, if and how basalt was included via faults Target basalt pockets in Olympic core Examine basalt from selected sites in the Crescent Formation	Structural observations to find fault indicators XRF, as with this study Petrography, as with this study, plus emphasis on minerals outside standard basalt suite EMP, as with Project 1	Two-year M.S.: Year 1: Background, discuss project with Western Wash. faculty) Year 2: Fieldwork, collection in summer, sample preparation & analysis summer through winter Alternative: Undergraduate project A for fieldwork, collection Undergraduate project B to prepare and analyze samples	Fieldwork: 2 – 3 people at $25/day, 7 – 14 days Mileage: $.50/mi, 500 – 900 mi for lab analysis and travel to field Thin sections: $300 (~$17/sample) XRF: $150 ($10/sample) EMP: ~$1000 - $1500 (2 – 3 days)	Bohrson or Mattinson and D. Hirsch or S. Babcock
6	Determine vein-forming fluid composition Determine pressure, temperature of vein formation (e.g., Vrolijk, 1987)	Sample vein fluid inclusions from this study, Project 1, and any samples available Cut thick doubly polished sections & analyze on fluid inclusion stage Possible cathodoluminescence to identify zoning	Undergraduate: limited suite, (only samples from this study) Two-year M.S.: Year 1: Select samples Year 2: Beginning in summer, analyze veins	Travel: ~$400 – $800 for flight/lodging Thin sections: $175 – $600 ($35/section) Analysis time: ~$500 – $1500	To be determined

*Project requiring sample permit from the National Park Service.

exhumed metasedimentary accretionary prism, implications of some structures observed by Tabor and Cady (1978a, b) may not have been fully realized. Furthermore, the work of Tabor and Cady took place long before the Cascadia subduction zone was recognized as seismogenic (Atwater, 1987), so the potential of the Olympic Peninsula to record seismogenic behavior may not have been recognized until now.

CHAPTER VI

SUMMARY AND OUTLOOK

The metasedimentary accretionary prism rocks of the Olympic Peninsula show evidence of dehydration consistent with increasing burial depth from west to east and locally contain quartz veins that record quantities of fluid flow adequate to generate fluid overpressure. Quartz veins record total H_2O flow of $10^{13} – 10^{14}$ kg/km^3, and total structural H_2O dehydrated from the rocks is $\sim 7 \times 10^{10}$ kg/km^3 from 6–14 km burial depth. The rate of structural H_2O subduction in Olympic Peninsula rocks, assuming a 1.5–3 m.y. burial time, is $\sim 2 \times 10^4 – 5 \times 10^4$ kg per km of trench per year. The model of Jarrard (2003) yields $3.2 \times 10^5 – 1.3 \times 10^6$ kg structural H_2O per km of trench per year from 6–50 km depth, so my estimate of H_2O dehydration from 6–14 km depth is within two orders of magnitude of modeled H_2O flux. Vein H_2O flowed at $\sim 10^6 – 10^7$ kg per km of trench per year over a period of ~1.5 m.y. at Obstruction Peak, which was buried to 14 km. Saffer and Bekins (1998) modeled H_2O flow of $2 \times 10^7 – 2 \times 10^8$ kg per km of trench per year, sufficient to result in fluid overpressure, in a model to ~7 km maximum depth at the compositionally similar Nankai sedimentary accretionary prism. Therefore, H_2O flow recorded by quartz veins is more than sufficient to result in fluid overpressures during burial of my Olympic Peninsula rocks, as is indicated by the existence of fibrous quartz veins at Obstruction Peak.

There is $\sim 6 \times 10^{10}$ kg structural H_2O remaining in 1 km^3 at Obstruction Peak, which is available to dehydrate at greater depths and flow updip, perhaps to create the fluid overpressure that resulted in vein formation at Obstruction Peak. Note that the structural H_2O at Obstruction Peak is 1000 times less than the minimum H_2O recorded by veins at Obstruction Peak. However, as explained in Chapter V, fluid flow velocities in sedimentary accretionary prism rocks mean it is likely H_2O dehydrated from shallower levels (e.g., 6 km) within the sedimentary accretionary prism can be transported to greater depth and contribute to fluid overpressure at depths ~14 km. Therefore, H_2O in sedimentary accretionary prisms can be released at different depths at quantities and rates sufficient to generate fluid overpressure conditions and contribute to weakening of rock. This is consistent with the hypothesis, based on experimental, modeling, and observational data, that fluid release and movement in rocks contributes to seismicity.

Future studies are needed to more precisely constrain the temperature conditions of the Olympic Peninsula and, more importantly, the extent of dehydration with depth in the exhumed metasedimentary accretionary prism rocks. It is important to understand the role of H_2O and fluid overpressure in seismicity and H_2O release as a function of depth and therefore changes in rock strength. Sedimentary accretionary prisms span the locked to creeping section of megathrust faults, as explained in Chapter II, and therefore exhumed sedimentary accretionary prisms are an ideal location in which to understand H_2O and subduction zone seismicity. Connections between H_2O and seismicity established in the Olympic Peninsula rocks of the Cascadia subduction zone could also be applied to other subduction zones and/or other types of fault systems.

REFERENCES

Akinfiev, N.N., and Diamond, L.W., 2009, A simple predictive model of quartz solubility in water-salt-CO_2 systems at temperatures up to 1000°C and pressures up to 1000 MPa: Geochimica et Cosmochimca Acta, v. 73, p. 1597-1608.

Atwater, B.F., 1987, Evidence for great Holocene earthquakes along the outer coast of Washington State: Science, v. 236, p. 942-944.

Atwater, B.F., and Hemphill-Haley, E., 1997, Recurrence intervals for great earthquakes of the past 3500 years at northeastern Willapa Bay, Washington: U.S. Geological Survey Professional Paper 1576, 108 p.

Babcock, R.S., Burmeister, R.F., Engbretson, D.C., Warnock, A., and Clark, K.P., 1992, A rifted margin origin for the Crescent basalts and related rocks in the northern Coast Range volcanic province, Washington and British Columbia: Journal of Geophysical Research, v. 97, p. 6799-6821.

Bebout, G.E., 1995, The impact of subduction-zone metamorphism on mantle-ocean chemical cycling: Chemical Geology, v. 126, p. 191-218.

Bhatia, M.R., 1983, Plate tectonics and geochemical composition of sandstones: Journal of Geology, v. 91, p. 611-627.

Bird, P., 1984, Hydration-phase diagrams and friction of montmorillonite under laboratory and geologic conditions, with implications for shale compaction, slope stability, and strength of fault gouge: Tectonophysics, v. 107, p. 235-260.

Bostock, M.G., Hyndman, R.D., Rondenay, S., and Peacock, S.M., 2002, An inverted continental Moho and serpentinization of the forearc mantle: Nature, v. 417, p. 536-538.

Brandon, M.T., and Calderwood, A.R., 1990, High-pressure metamorphism and uplift of the Olympic subduction complex: Geology, v. 18, p. 1252-1255.

Brandon, M.T., and Vance, J.A., 1992, Tectonic evolution of the Cenozoic Olympic subduction complex, Washington state, as deduced from fission track ages for detrital zircons: American Journal of Science, v. 292, p. 565-636.

Brandon, M.T., Roden-Tice, M.K., and Garver, J.I., 1998. Late Cenozoic exhumation of the Cascadia accretionary wedge in the Olympic Mountains, northwest Washington State: Geological Society of America Bulletin, v. 110, p. 985-1009.

Breeding, C.M., and Ague, J.J., 2002, Slab-derived fluids and quartz-vein formation in an accretionary prism, Otago Schist, New Zealand: Geology, v. 30, p. 499-502.

Byrne, T., and Fisher, D., 1990, Evidence for a weak and overpressured décollement beneath sediment-dominated accretionary prisms: Journal of Geophysical Research, v. 95, p. 9081-9097.

Chapman, J.S., and Melbourne, T.I., 2009, Future Cascadia megathrust rupture delineated by episodic tremor and slip: Geophysical Research Letters, v. 36, doi:10.1029/2009GL040465.

Conrey, R., 2010, personal communication, May.

Davis, E.E., and Hyndman, R.D., 1989, Accretion and recent deformation of sediments along the northern Cascadia subduction zone: Geological Society of America Bulletin, v. 101, p. 1465-1480.

DeIvigne, J.E., 1998, Atlas of micromorphology of mineral alteration and weathering: Ottawa, Mineralogical Association of Canada, Special Publication 3, 494 p.

Fisher, D.M., and Brantley, S.L., 1992, Models of quartz overgrowth and vein formation: Deformation and episodic fluid flow in an ancient subduction zone: Journal of Geophysical Research, v. 97, p. 20043-20061.

Geological Survey of Canada, Geodynamics-Episodic Tremor and Slip, accessed at http://gsc.nrcan.gc.ca/geodyn/ets_e.php

Gutscher, M.-A., Klaeschen, D., Flueh, E., and Malavieille, J., 2001, Non-Coulomb wedges, wrong-way thrusting, and natural hazards in Cascadia: Geology, v. 29, p. 379-382.

Hacker, B.R., Abers, G.A., and Peacock, S.M., 2003a, Subduction factory 1. Theoretical mineralogy, densities, seismic wave speeds, and H_2O contents: Journal of Geophysical Research, v. 108, doi:10.1029/2001JB001127.

Hacker, B.R., Peacock, S.M., Abers, G.A., and Holloway, S.D. 2003b, Subduction factory 2. Are intermediate-depth earthquakes in subducting slabs linked to metamorphic dehydration reactions?: Journal of Geophysical Research, v. 108, doi:10.1029/2001JB001129.

Hacker, B.R. 2008. H_2O subduction beyond arcs: Geochemistry, Geophysics, Geosystems, v. 9, doi:10.1029/2007GC001707.

Halbach, H., and Chatterjee, N.D., 1982, An empirical Redlich-Kwong-type equation of state for water to 1000°C and 200 kbar: Contributions to Mineralogy and Petrology, v. 79, p. 337-345.

Hawkins, J.W., Jr., 1967, Prehnite-pumpellyite facies metamorphism of a greywacke-shale series, Mount Olympus, Washington: American Journal of Science, v. 265, p. 798-818.

Herron, M.M., 1988, Geochemical classification of terrigenous sands and shales from core or log data: Journal of Sedimentary Petrology, v. 58, p. 820-829.

Hirsch, D.M, and Babcock, R.S., 2009, Spatially heterogeneous burial and high-P/T metamorphism in the Crescent Formation, Olympic Peninsula, Washington: American Mineralogist, v. 94, p. 1103-1110.

Holcombe, R.J., 2009, GEOrient, version 9.4.4, accessed http://www.holcombe.net.au/software/

Hyndman, R.D., Wang, K., Yuan, T., and Spence, G.D., 1993, Tectonic sediment thickening, fluid expulsion, and the thermal regime of subduction zone accretionary prisms: the Cascadia margin off Vancouver Island: Journal of Geophysical Research, v. 98, p. 21865-21876.

Jarrard, R. D. 2003. Subduction fluxes of water, carbon dioxide, chlorine, and potassium: Geochemistry, Geophysics, Geosystems, v. 4, doi:10.1029/2002GC000392.

Johnson, D.M., Hooper, P.R., and Conrey, R.M., 1999, XRF analysis of rocks and minerals for major and trace elements on a single low dilution Li-tetraborate fused bead, in Proceedings, Advances in X-ray Analysis, 41st, Denver: Colorado, International Center for Diffraction Data, p. 843-867.

Julian, B.R., 1994, Volcanic tremor: nonlinear excitation by fluid flow: Journal of Geophysical Research, v. 99, p. 11859-11877.

Kao, H., Shan, S.-J., Dragert, H., Rogers, G., Cassidy, J.F., and Ramachandran, K., 2005, A wide depth distribution of seismic tremors along with northern Cascadia margin: Nature, v. 436, p. 841-844.

Kondo, H., Kimura, G., Masago, H., Ohmori-Ikehara, K., Kitamura, Y., Ikesawa, E., Sakaguchi, A., Yamaguchi, A., and Okamoto, S., 2005, Deformation and fluid flow of a major out-of-sequence thrust located at seismogenic depth in an accretionary complex: Nobeoka Thrust in the Shimanto Belt, Kyushu, Japan: Tectonics, v. 24, doi:10.1029/2004TC001655

Manning, C.E., 1994, The solubility of quartz in H2O in the lower crust and upper mantle: Geochimica et Cosmochimica Acta, v. 58, p. 4831-4839.

McNutt, S.R., 2000, Volcanic seismicity, *in* Sigurdsson, H., ed., Encyclopedia of volcanoes: San Diego, Academic Press, p. 1015-1033.

Meneghini, F., Di Toro, G., Rowe, C.D., Moore, J.C., Tsutsumi, A., and Yamaguchi, A., 2010, Record of mega-earthquakes in subduction thrusts: the black fault rocks of Pasagshak Point (Kodiak Island, Alaska): Geological Society of America Bulletin, v. 122, p. 1280-1297.

Miller, S.A., Ben-Zion, Y., and Burg, J.-P., 1999, A three-dimensional fluid-controlled earthquake model: behavior and implications: Journal of Geophysical Research, v. 104, p. 10621-10638.

Moore, J.C, and Vrolijk, P., 1992, Fluids in accretionary prisms: Reviews of Geophysics, v. 30, p. 113-135.

Moore, J.C., Rowe, C., and Meneghini, F., 2007, How accretionary prisms elucidate subduction zone seismogenesis, *in* Tim Dixon, ed., Proceedings from the Seismogenic Zone Theoretical Institute, Snowbird, Utah, March 2003, Columbia University Press, p. 288-315.

Normark, W.R, and Reid, J.A., 2003, Extensive deposits on the Pacific plate from late Pleistocene North American glacial lake outbursts: Journal of Geology, v. 111.

O'Neil, J.R., 1979, Stable isotope geochemistry of rocks and minerals, *in* Jäger, H., and Hunziker, J.C., eds., Lectures in isotope geology: Berlin, Springer-Verlag, p. 235-263.

Orange, D.L, McAdoo, B.G., Moore, J.C., Tobin, H., Screaton, E., Chezar, H., Lee, H., Reid, M., and Vail., M., 1997, Headless submarine canyons and fluid flow on the toe of the Cascadia accretionary complex: Basin Research, v. 9, p. 303-312.

Plank, T., and Langmuir, C.H., 1998, The chemical composition of subducting sediment and its consequences for the crust and mantle: Chemical Geology v. 145 p. 325-394.

Rogers, G., and Dragert, H., 2003, Episodic tremor and slip on the Cascadia subduction zone: The chatter of silent slip: Science, v. 300, p. 1942-1943.

Rotman, H.M.M., and Mattinson, C.G., 2009, Field observations on fluid budget of the Cascadia episodic tremor and slip system, Olympic Peninsula, Washington: Geological Society of America Abstracts with Programs, v. 41 no. 7, p. 635.

Rowe, C.D., Meneghini, F., and Moore, J.C., 2009; Fluid-rich damage zone of an ancient out-of-sequence-thrust, Kodiak Islands, Alaska: Tectonics, v. 28, TC1006 doi:10.1029/2007TC002126

Rowe, K.T., and Screaton, E., 2009, Permeabilities of Core Samples from Integrated Ocean Drilling Program Expedition 316 and Implications for Shallow Fluid Flow due to Megasplay Fault Movement: Eos Transactions, American Geophysical Union, v. 90, no. 52, Fall Meeting Supplement, Abstract T21C-1839.

Saffer, D.M., and Bekins, B.A., 1998, Episodic fluid flow in the Nankai accretionary complex: Timescale, geochemistry, flow rates, and fluid budget: Journal of Geophysical Research, v. 103, p. 30351-30370.

Saffer, D.M., and Bekins, B.A., 1999, Fluid budgets at convergent plate margins: Implications for the extent and duration of fault-zone dilation: Geology, v. 27, p. 1095-1098.

Sample, J.C., Reid, M.R., Tobin, H.J., and Moore, J.C., 1993, Carbonate cements indicate channeled fluid flow along a zone of vertical faults at the deformation front of the Cascadia accretionary wedge (northwest U.S. coast): Geology, v. 21, p. 507-510.

Satake, K., Shimazaki, K., Tsuji, Y., and Ueda, K., 1996, Time and size of a giant earthquake in Cascadia inferred from Japanese tsunami records of January 1700: Nature, v. 379, p. 246-249.

Schacht, U., Wallmann, K., Kutterolf, S., and Schmidt, M., 2008, Volcanogenic sediment-seawater interactions and the geochemistry of pore waters: Chemical Geology, v. 249, p. 321-338.

Schwartz, S.Y., and Rokosky, J.M., 2007, Slow slip events and seismic tremor at circum-Pacific subduction zones: Reviews of Geophysics, v. 45, doi:10.1029/2006RG000208.

Screaton, E.J., Wuthrich, D.R., and Dreiss, S.J., 1990, Permeabilities, fluid pressures, and flow rates in the Barbados Ridge complex: Journal of Geophysical Research, v. 95, p. 8997-9007.

Shelly, D.R., Beroza, G.C., Ide, S., and Nakamula, S., 2006, Low-frequency earthquakes in Shikoku, Japan, and their relationship to episodic tremor and slip: Nature, v. 442, p. 188-191.

Sisson, V.B., and Hollister, L.S., 1988, Low-pressure facies series metamorphism in an accretionary sedimentary prism, southern Alaska: Geology, v. 16, p. 358-361.

Snavely, P.D., Jr., and Kvenvolden, K.A. 1989. Preliminary evaluation of the petroleum potential of the Tertiary accretionary terrane, west side of the Olympic Peninsula, Washington: A. Geology and hydrocarbon potential: U.S. Geological Survey Bulletin 1892, p. 1-17.

Speed, R., 1990, Volume loss and defluidization history of Barbados: Journal of Geophysical Research, v. 95, p. 8983-8996.

Stewart, R.J., and Brandon, M.T., 2004, Detrital-zircon fission-track ages for the “Hoh Formation”: implications for late Cenozoic evolution of the Cascadia subduction wedge: Geological Society of America Bulletin, v. 116, p. 60-75.

Tabor, R.W., Yeats, R.S., and Sorensen, M.L., 1972, Geologic map of the Mount Angeles Quadrangle, Clallam and Jefferson counties, Washington: U.S. Geological Survey Map GQ-958, scale 1:64 000, 1 sheet.

Tabor, R.W., and Cady, W.M. 1978a, Geologic map of the Olympic Peninsula: U.S. Geological Survey Miscellaneous Investigations Series Map I-994, scale 1:125 000, 2 sheets.

Tabor, R.W., and Cady, W.M., 1978b, The structure of the Olympic Mountains, Washington – analysis of a subduction zone: U.S. Geological Survey Professional Paper 1033, 38 p.

Taylor, H.P., Jr., 1967, Oxygen isotope studies of hydrothermal mineral deposits, *in* Barnes, H.L., ed., Geochemistry of hydrothermal ore deposits: New York, Holt, Rinehart and Winston, p. 109-142.

Valley, J.W., 1986, Stable isotope geochemistry of metamorphic rocks, *in* Valley, J.W., Taylor, H.P., Jr., and O’Neil, J.R., eds., Stable isotopes in high temperature geological processes: Washington, D.C., Mineralogical Society of America (and BookCrafters, Inc., Chelsea, MI), Reviews in Mineralogy v. 16, p. 445-489.

Valley, J.W., 1995, UWG-2, a garnet standard for oxygen isotope ratios: Strategies for high precision and accuracy with laser heating: Geochimica et Cosmochimica Acta, v. 59, p. 5223-5231.

Valley, J.W., 2001, Stable isotope thermometry at high temperatures, *in* Valley, J.W., and Cole, D.R., eds., Stable isotope geochemistry: Washington, D.C., Mineralogical Society of America, Reviews in Mineralogy and Geochemistry, v. 43, p. 365-412.

van der Pluijm, B.A., and Marshak, S., 2004, Earth Structure: An introduction to structural geology and tectonics: New York, W.W. Norton and Company, 656 p.

Vrolijk, P., 1987, Tectonically driven fluid flow in the Kodiak accretionary complex, Alaska: Geology, v. 15, p. 466-469.

Vrolijk, P., 1990, On the mechanical role of smectite in subduction zones: Geology, v. 18, p. 703-707.

White, J.E., 1976, Elastic dilatancy, fluid saturation, and earthquake dynamics: Geophysical Research Letters, v. 3, p. 747-750.

Wilson, D.S., 1988, Tectonic history of the Juan de Fuca ridge over the last 40 million years: Journal of Geophysical Research, v. 93, p. 11863-11876.

APPENDIXES

Appendix A

Field Data

TABLE A1. VEIN ORIENTATIONS,
HURRICANE HILL TRAIL

Strike (°)	Dip(°)
100	25N
58	16W
50	26SE
62	83W
41	22E
110	29N
151	24NE
54	13NW
134	24SE
175	10E
11	43W
25	37W
153	54SW

TABLE A2. BEDDING, OBSTRUCTION PEAK

Strike (°)	Dip(°)
130	63S
140	37S
148	78S
141	53S
139	66S
130	59S
135	64S
134	52S
140	75S
146	74S

TABLE A3. VEIN ORIENTATIONS, OBSTRUCTION PEAK

Strike (°)	Dip(°)
43	51W
44	55W
55	58W
32	49W
55	64W
168	50W
50	73W
96	60N
100	40N
95	35N
94	59N
90	46N
56	57N
80	55N
80	57N
68	60N
96	20N
14	39E
70	54N
74	37W
68	28N
80	53N
66	48N

TABLE A3, CONTINUED

Strike (°)	Dip(°)
84	37N
62	38N
58	42N

TABLE A4. ESTIMATE OF PERCENT VEINS AT OUTCROP, OBSTRUCTION PEAK

Outcrop thickness (m)	Thickness of veins (cm)	Vein (vol%)
5	25	2
3	20	5
7	40	10
6	30	5
6	30	5
6	100	10
8	0	0
8	0	0
15	100	7
10	30	5

TABLE A5. VEIN COUNT AND THICKNESS, SELECTED OUTCROPS, OBSTRUCTION PEAK

Site A, 2 m	Site B, 1 m	Site C, 3 m	Site D, 40 cm
3 mm	3.5 mm	3 mm	3 mm
1.5 mm	6.5 mm	1 mm	1.5 mm
1 mm	2 mm	4 mm	1.5 mm
<1 mm	5 mm	3 mm	2 mm
<1 mm	4 mm		2 mm
<1 mm	3 mm		1 mm
1 mm	3 mm		1 mm
4 mm	1.5 mm		1 mm
5 mm			2.5 mm
5 mm			3 mm
5 mm			4 mm
2 mm			3 mm
2 mm			1 mm
1.5 mm			1.5 mm
1.5 mm			6 mm
1.5 mm			7 mm
1.5 mm			12 mm
1 mm			3 mm
1 mm			2 mm
4 mm			
5 mm			
2 mm			
2 mm			

Appendix B

Petrography

TABLE B1. THIN SECTION DESCRIPTION, OP3

Component	Modal abundance (%)	Notes
Chlorite	1	Yellow-blue in XPL, pale yellow and slightly pleochroic PPL, basal cleavage may be visible
Sericite	3	Colorless in PPL, scruffy, fine-grained, matrix to sandstone
Muscovite	3	Basal cleavage may be visible, colorless in PPL, birdseye extinction & birefringence up to 2nd order yellow in XPL
Kaolinitized mica	12	Bulging grains & cleavage, cleavage difficult to identify, yellow-brown in PPL & XPL
Biotite	N/A	
Lithics	7	Preferential orientation if flattened, fine-grained (shale), cut by quartz veins
Matrix	N/A	
Epidote	1	Subrounded to rounded, <.1mm, patchy birefringence in XPL, colorless & high relief in PPL
Quartz	16 (vein) 34 (detrital)	In vein and wallrock, subangular in wallrock, fibrous and rarely blocky in vein, colorless in PPL
Iron oxide	12	Hematite, reddish-orange, cementing grains
Opaques	10	Possibly pressure solution or graphite; may also be Fe-Ti oxides
Plagioclase	1	Polysynthetic twins, colorless in PPL

Note: For this and all tables in this Appendix, hydrous components are listed first in the same order as Table 4, followed by anhydrous components in decreasing order of abundance. PPL refers to plane polarized light and XPL refers to cross-polarized light.

TABLE B2. THIN SECTION DESCRIPTION, OP7

Component	Modal abundance (%)	Notes
Chlorite	1	Single cleavage may be visible, blue or yellow in XPL, greenish in PPL
Sericite	20	White, yellow, or brown in XPL, fine-grained and very scruffy appearance
Muscovite	8	May be altered or kinked, .1–.5 mm long, colorless in PPL, birds-eye in XPL unless altered
Kaolinitized mica	10	Visibly bulging, or swollen cleavage. Pleochroic. Brown in PPL & XPL, may show minor birdseye in XPL
Biotite	3	Altered to opaques and muscovite, cleavage relict even where altered to opaque mineral
Lithics	2	Composed of siltstone or mudrock, may be flattened and show preferential orientation
Matrix	N/A	
Epidote	trace	Very high relief, nearly colorless in PPL
Quartz	47	Subrounded to angular, some grains may have inclusion trails, colorless in PPL
Plagioclase	5	Multiple twins common, many grains have sericite alteration and possible sericite/chlorite alteration, colorless PPL unless altered
Opaques	2	Black, randomly distributed Fe-Ti oxides
Iron oxide	1	Reddish, marks bedding & lithologic change
Pumpellyite	trace	Fine-grained, green pleochroism darkest oriented E-W on stage, bluish in XPL

TABLE B3. THIN SECTION DESCRIPTION, OP12

Component	Modal abundance (%)	Notes
Chlorite	trace	Bluish in XPL, yellow in PPL, single cleavage may be visible, grains <.5 mm long
Sericite	20	See Table B2
Muscovite	12	Grains up to 2 mm long, see Table B1
Kaolinitized mica	10	See Table B2
Biotite	N/A	
Lithics	8	Fine-grained, likely shale composition, dark PPL & XPL, grains up 1.2 mm long
Matrix	4	Reddish, likely heavy iron oxide component
Epidote	N/A	
Quartz	40	Subrounded to subangular, some microcrystalline grains, monocrystalline grains may have fluid inclusion trails, colorless in PPL
Plagioclase	3	Multiple twins common, almost all grains show sericite alteration, colorless in PPL except for alteration
Iron oxide	3	Reddish, randomly distributed grains, <.5 mm, subrounded to subangular

TABLE B4. THIN SECTION DESCRIPTION, OP13

Component	Modal abundance (%)	Notes
Chlorite	N/A	
Sericite	17	See Table B2
Muscovite	3	All grains <.5 mm long, cleavage planes may be separated but grains are not kinked around rigid grains, see also Table B1
Kaolinitized mica	5	See Table B2
Biotite	N/A	
Lithics	3	Flattened, commonly fine-grained, shale composition, dark XPL & PPL
Matrix	N/A	
Epidote	N/A	
Calcite	33	Mainly present in lens/vein, twin lamellae, relief changes with stage rotation
Quartz	32	Rounded to subangular, some grains polycrystalline, few grains with inclusion trails, colorless in PPL
Plagioclase	3	See Table B2
Opaques	2	Occur in aggregates, grains <.2 mm in diameter
Iron oxide	2	Most grains in calcite lens along calcite grain boundaries

TABLE B5. THIN SECTION DESCRIPTON, OP20

Component	Modal abundance (%)	Notes
Chlorite	N/A	
Sericite	10	See Table B2
Muscovite	9	All <.2 mm, many .05–.1 mm, kinking uncommon, preferential orientation, see also Table B1
Kaolinitized mica	10	See Table B2
Biotite	N/A	
Lithics	N/A	
Matrix	15	Fine-grained layers, shale composition, likely quartz + muscovite + graphite, but too fine to fully identify
Epidote	N/A	
Quartz	35	Subangular to subrounded, .04–.2 mm, most .075–.125 mm, colorless in PPL
Opaques	16	Strung out grains that may be either graphite or pressure solution
Plagioclase	1	All grains <.15 mm, multiple twins, colorless in PPL
Iron oxide	4	Scruffy reddish-brown grains, often adjacent to quartz grains

TABLE B6. THIN SECTION DESCRIPTION, OP23

Component	Modal abundance (%)	Notes
Chlorite	N/A	
Sericite	22	Includes sericite composing matrix, see Table B2.
Muscovite	7	Colorless PPL, birdseye extinction & 2nd order birefringence XPL, basal cleavage visible, many grains distorted or kinked, .1–.5 mm long
Kaolinitized mica	5	See Table B2
Biotite	5	Commonly distorted, grains .1–.9 mm long, pale brown & pleochroic PPL
Lithics	N/A	
Matrix	N/A	
Epidote	1	Very high relief, colorless to pale yellow PPL, patchy birefringence XPL
Quartz	35	Subrounded to subangular, .1–.25 mm, colorless in PPL
Iron oxide	8	Possibly hematite, subhedral to euhedral, reddish brown in PPL
Plagioclase	7	Grains <.25 mm, polysynthetic twinning, grains may have sericite overgrowth, colorless in PPL unless altered
Opaques	5	Subhedral Fe-Ti oxides, grains <.2 mm
Calcite	3	Acting as cement or matrix, rare grains with twin lamellae visible
Sphene	2	Brown aggregates <.1 mm, high birefringence of creamy pink-green

TABLE B7. THIN SECTION DESCRIPTION, OP31

Component	Modal abundance (%)	Notes
Chlorite	trace	See Table B3
Sericite	25	Composes matrix. See Table B2
Muscovite	7	Up to .6 mm long, no preferential orientation, grains may be kinked, colorless in PPL, see Table B1
Kaolinitized mica	6	See Table B2
Biotite	3	Mostly altered to opaques & muscovite
Lithics	8	Some are volcaniclastic with many plagioclase laths in fine-grained matrix, grains may be up to .6 mm, dark in PPL & XPL
Matrix	N/A	
Epidote	N/A	
Quartz	46	Subrounded to subangular, inclusion trails rare, up to 1.2 mm but most grains .2–.6 mm, colorless in PPL
Plagioclase	5	Polysynthetic twinning, many grains have little sericite alteration, few have substantial sericite alteration, colorless in PPL unless altered

TABLE B8. THIN SECTION DESCRIPTION, OP37

Component	Modal abundance (%)	Notes
Chlorite	2	One or two grains ~.5 mm, remainder filling in old pore space, may be growing with a book-like appearance on other minerals such as plagioclase
Sericite	4	See Table B2, very fine
Muscovite	1	A few grains <.1 mm, colorless in PPL, yellow-pink-green birefringence (2nd order) in XPL
Kaolinitized mica	4	See Table B2
Biotite	N/A	
Lithics	30	Up to 2 mm long, fine grained (e.g., shale), dark in XPL & PPL
Matrix	15	Too fine to identify, but likely a mix of fine-grained phyllosilicates and graphite
Epidote	trace	A few grains <.12 mm, high relief & near colorless in PPL, patchy yellow-pink-orange birefringence in XPL
Quartz	40	Includes microcrystalline quartz, monocrystalline quartz may have brownish randomly distributed inclusions, inclusion trails are rare, colorless in PPL
Opaques	4	Possibly aggregates of matrix, or Fe-Ti oxides
Plagioclase	trace	Colorless in PPL, may have polysynthetic twins, sericite alteration

TABLE B9. THIN SECTION DESCRIPTION, OP38

Component	Modal abundance (%)	Notes
Chlorite	2	Single cleavage may be visible, yellow in PPL, slightly pleochroic
Sericite	18	See Table B2, fine-grained
Muscovite	6	Grains <.2 mm, colorless in PPL, commonly yellow in XPL, see Table B1
Kaolinitized mica	N/A	
Biotite	1	Isolated grains, altered to opaques + muscovite
Lithics	15	Fine grained (shale) + volcaniclastics, subrounded to subangular depending on composition
Matrix	20	Too fine to identify, likely fine-grained phyllosilicates and graphite
Epidote	trace	High relief, nearly colorless in PPL
Quartz	35	Detrital monocrystalline and polycrystalline plus rare veins <.2 mm across, few grains have inclusion trails, most grains smaller than OP37, colorless in PPL
Plagioclase	2	Polysynthetic twins usually preserved, sericite alteration common, colorless in PPL unless altered
Opaques	1	Fe-Ti oxides, anhedral or rounded

TABLE B10. THIN SECTION DESCRIPTION, OP41

Component	Modal abundance (%)	Notes
Chlorite	2	Blue to purple in XPL, green, pleochroic in PPL, grains <1 mm, single cleavage may be visible
Sericite	18	See Table B2, fine, acting as matrix
Muscovite	8	Some grains have preferential orientation, green to blue birefringence + birdseye extinction in XPL, colorless in PPL, most grains <.2 mm long, longer grains commonly kinked but cleavage planes not separated
Kaolinitized mica	6	<.4 mm, See Table B2
Biotite	N/A	
Lithics	10	Most fine-grained (shale), <.4 mm
Matrix	N/A	
Epidote	trace	Colorless in PPL, high relief, yellow to blue 3rd order birefringence in XPL
Quartz	43	Grains <.7 mm, subrounded to subangular, few grains with inclusion trails, colorless in PPL
Calcite	7	Twin lamellae visible, relief changes with stage rotation, acting as matrix
Plagioclase	4	Polysynthetic twins commonly preserved, sericite alteration common, possible additional stage of alteration since some grains brownish in XPL, colorless in PPL unless altered
Opaques	2	<.25 mm, Fe-Ti oxides

Appendix C

Unabridged X-Ray Fluorescence Results

TABLE C1. MAJOR ELEMENT DATA, NORMALIZED

Oxide (wt%)	OP7	OP11	OP16	OP17	OP18	OP19	OP22	OP23	OP24	OP31
SiO_2	76.34	77.35	46.12	46.76	55.48	47.65	46.79	71.71	65.03	76.14
TiO_2	0.512	0.452	1.934	1.100	0.779	1.729	0.482	0.796	0.827	0.416
Al_2O_3	13.16	12.33	17.23	14.42	16.80	16.92	10.96	13.69	18.08	12.41
FeO^*	2.94	3.16	10.69	12.08	7.24	11.38	4.51	3.47	6.85	2.36
MnO	0.040	0.034	0.189	0.241	0.099	0.177	0.187	0.064	0.025	0.049
MgO	1.17	1.13	7.62	14.79	2.49	9.45	11.77	1.22	2.05	1.07
CaO	0.46	0.96	12.11	8.61	10.22	8.65	21.30	3.40	0.998	2.16
Na_2O	2.95	3.08	3.42	1.77	5.24	3.15	1.46	4.20	2.71	3.17
K_2O	2.32	1.40	0.28	0.08	1.42	0.68	2.31	1.29	2.62	2.14
P_2O_5	0.112	0.097	0.412	0.149	0.124	0.211	0.242	0.173	0.732	0.083
Sum	100.00	100.00	100.00	100.00	100.00	100.00	100.00	100.00	100.00	100.00
LOI	2.41	2.82	6.25	11.81	9.15	4.90	24.49	4.34	5.65	3.38

TABLE C1, CONTINUED

Oxide (wt%)	OP32	OP33	OP34	OP35	OP36	OP37	OP38	OP40	OP41
SiO_2	70.99	48.56	59.44	63.72	73.61	73.11	70.40	62.74	74.57
TiO_2	0.551	1.375	0.896	1.036	0.748	0.717	0.810	0.922	0.668
Al_2O_3	13.35	18.73	18.51	17.75	12.07	12.84	14.25	18.74	12.85
FeO*	5.45	11.20	7.55	8.39	5.67	5.84	6.59	8.96	3.65
MnO	0.065	0.140	0.317	0.109	0.116	0.087	0.089	0.131	0.050
MgO	2.57	10.33	3.07	3.85	2.76	2.76	2.82	3.09	1.67
CaO	1.94	4.24	1.62	0.40	1.67	0.98	1.04	0.32	1.35
Na_2O	3.67	5.16	8.07	2.62	2.47	2.30	2.38	2.63	3.01
K_2O	1.28	0.18	0.22	1.91	0.75	1.21	1.48	2.33	2.05
P_2O_5	0.130	0.187	0.304	0.208	0.135	0.158	0.144	0.145	0.131
Sum	100.00	100.00	100.00	100.00	100.00	100.00	100.00	100.00	100.00
LOI	3.45	7.88	2.57	4.50	3.58	3.41	4.09	6.17	3.37

*Total Fe.

TABLE C2. TRACE ELEMENT DATA

Element (ppm)	OP7	OP11	OP16	OP17	OP18	OP19	OP22	OP23	OP24	OP31
Ni	16	17	140	645	89	154	11	19	22	13
Cr	43	43	192	777	81	172	24	46	60	29
Sc	8	8	22	27	17	31	7	12	20	7
V	56	59	215	210	171	264	53	72	153	47
Ba	593	338	90	48	273	297	387	319	603	570
Rb	81	49	9	4	52	25	63	43	90	67
Sr	139	155	191	175	232	476	408	211	116	255
Zr	232	149	141	83	114	116	203	294	272	126
Y	23	15	28	22	30	28	15	22	46	14
Nb	12.5	9.5	24.5	8.6	9.5	11.1	7.6	14.9	16.5	10.0
Ga	16	14	16	15	19	17	9	14	23	14
Cu	9	10	65	70	262	81	13	21	35	1
Zn	54	53	72	81	158	78	39	62	80	41
Pb	15	10	0	4	17	0	6	11	13	12
La	34	20	17	11	27	8	13	35	35	18
Ce	67	43	38	23	50	24	27	62	77	39
Th	11	6	2	2	7	1	5	10	9	6
Nd	28	20	20	13	27	14	12	28	36	17
U	3	2	1	3	3	1	1	3	2	2

TABLE C2, CONTINUED

Element (ppm)	OP32	OP33	OP34	OP35	OP36	OP37	OP38	OP40	OP41
Ni	19	237	126	79	42	60	56	75	18
Cr	42	327	69	141	94	113	128	97	58
Sc	11	40	23	24	18	18	18	20	9
V	95	270	141	198	143	138	154	207	73
Ba	448	293	209	643	255	479	503	789	569
Rb	43	6	7	61	23	36	43	82	73
Sr	276	345	278	95	145	127	129	95	186
Zr	140	99	177	136	86	96	124	137	423
Y	17	26	53	24	17	21	20	26	31
Nb	10.9	9.6	13.2	9.1	5.3	6.3	7.5	12.4	16.4
Ga	15	15	21	18	13	14	16	22	15
Cu	18	136	157	78	33	30	43	131	11
Zn	58	70	169	136	70	86	90	145	55
Pb	11	0	8	10	5	4	5	14	14
La	22	9	43	20	12	15	13	25	46
Ce	43	15	75	35	19	28	25	53	89
Th	5	2	8	5	2	3	3	8	16
Nd	18	7	47	21	11	13	14	27	35
U	1	0	1	1	0	1	2	2	4

Appendix D

Oxygen Isotope Values and Corrections

TABLE D1. $\delta^{18}O$ VALUES, DAY ONE*

Sample	$\delta^{18}O$ (‰)
MM-1[†]	4.67
MM-1	12.01
UWG-2[§]	5.82
UWG-2	5.77
OP28-Fib2	13.14
OP28-Fib2	14.37
UWG-2[#]	9.68

Note: All values positive relative to standard mean ocean water for this and all tables in this Appendix. Fib is fibrous and blo is blocky quartz vein for all tables in this Appendix.

*No corrections were required on this day.

[†] Internal standard with known value of 12.8‰.

[§] Known value of 5.8‰ (Valley, 1995).

[#] Error in valve open-close sequence caused contamination with previous sample.

TABLE D2. $\delta^{18}O$ VALUES,
DAY TWO

Sample	$\delta^{18}O$ (‰)
MM-1	1.98
UWG-2	5.92
OP3-Fib	12.08
OP3-Fib	15.08
OP20-Fib	14.1
UWG-2*	7.31
OP20-Fib	13.02
OP21-Blo	14.39
OP21-Blo	14.85
UWG-2	6.42
OP28-Fib1	13.29
OP21-Fib1	14.71
UWG-2	7.86

*Pumped to vacuum for 25 min after this sample due to inter-sample contamination concerns.

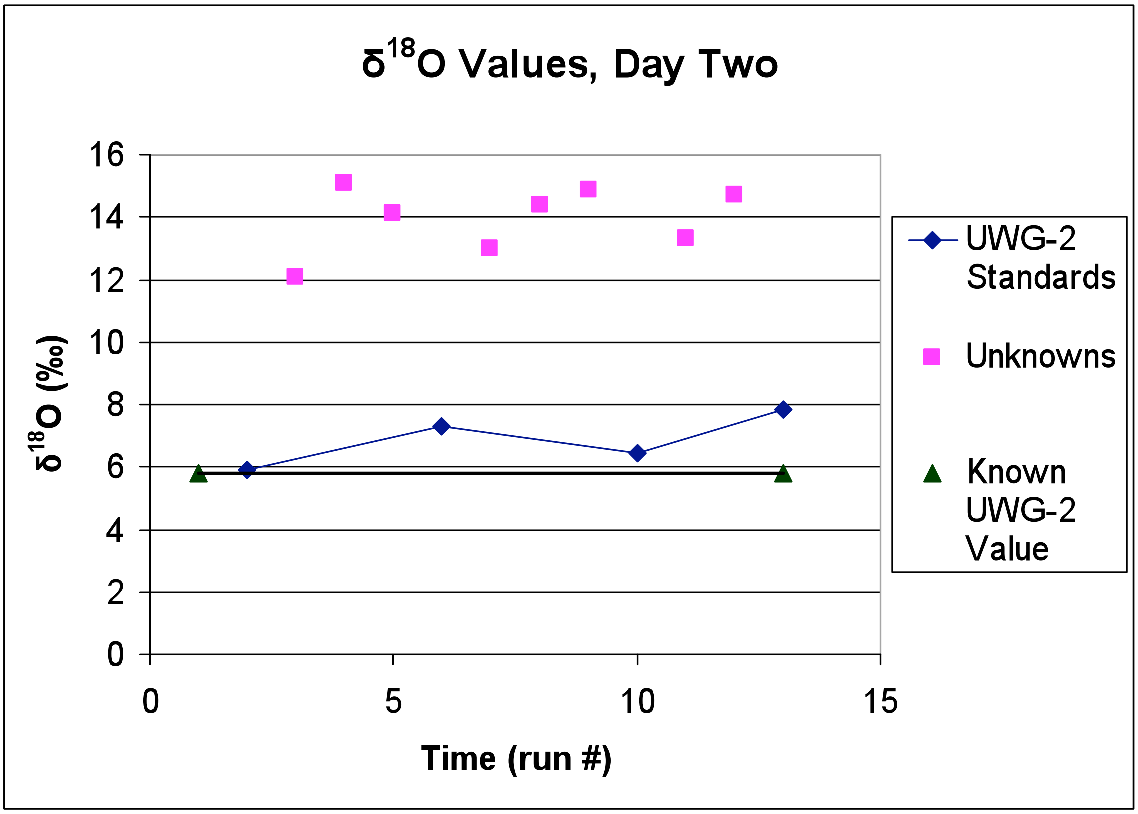

Figure D1. Calibration of unknowns against the established UWG-2 value, day two. Unknowns are pink squares and the UWG-2 standards run are blue connected diamonds. The black line with triangles represents the 5.8‰ established value of UWG-2. I used this graph to correct the raw δ^{18}O values from Table D2 into the values presented in Table 8 by correcting the unknowns against the UWG-2 runs with time.

TABLE D3. $\delta^{18}O$ VALUES,
DAY THREE

Sample	$\delta^{18}O$ (‰)
MM-1	1.17
UWG-2*	4.8
OP28-Blo	11.81
OP28-Blo	13.97
OP23-Det†	12.35
UWG-2	5.74
OP23-Det	11.44
OP12-Blo	15.88
OP12-Blo	16.58
UWG-2	7.64
OP3-Fib	13.95
UWG-2	7.46

*Pumped to vacuum for 60 min after this sample due to atmospheric contamination concerns.

†Det stands for detrital quartz.

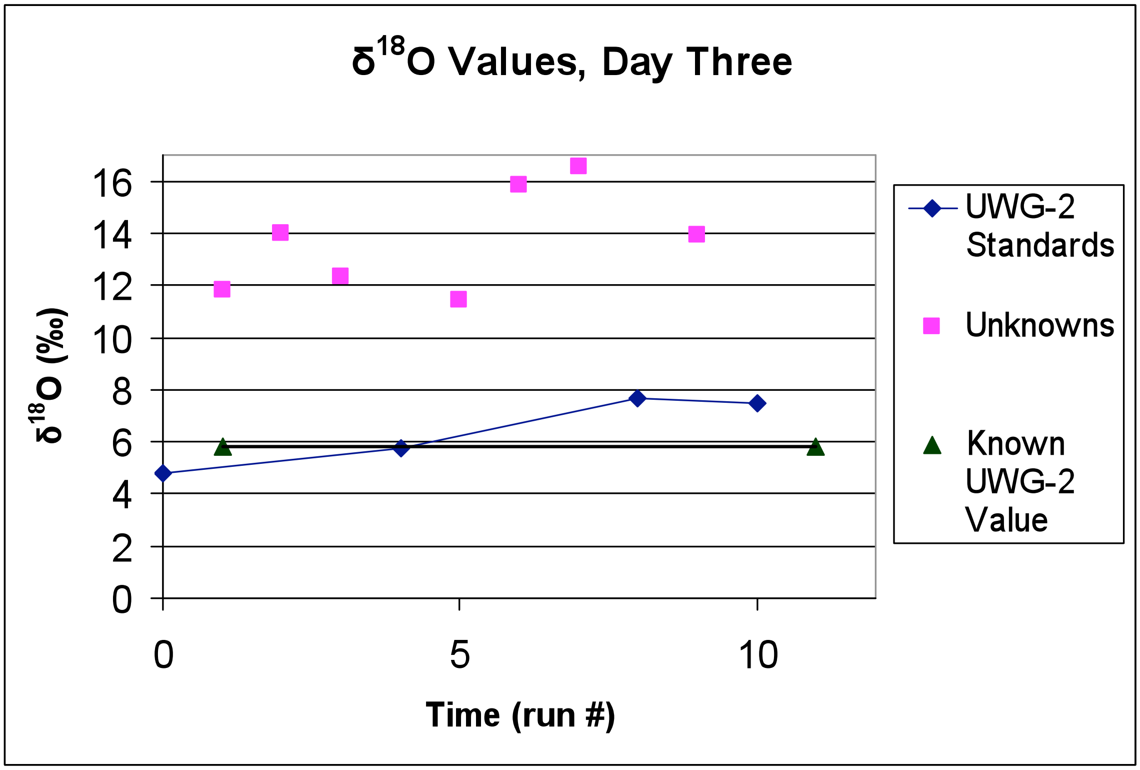

Figure D2. Calibration of unknowns against the established UWG-2 value, day three. Unknowns are pink squares and the UWG-2 standards run are blue connected diamonds. The black line with triangles represents the 5.8‰ established value of UWG-2. I used this graph to correct the raw $\delta^{18}O$ values from Table D2 into the values presented in Table 8 by correcting the unknowns against the UWG-2 runs with time.

Appendix E

Quartz Solubility and Molar Volume of H_2O

Quartz Solubility Equations

H_2O-SiO_2 mixture:

$$\log K = 4.2620 - 5764.2/T + (1.7513 \times 10^6)/T^2 - (2.2869 \times 10^8)/T^3$$
$$+ [2.8454 - 1006.9/T + (3.5689 \times 10^5)/T^2] \times \log \rho_{H2O}$$

Where:

$\log K = \log m_{SiO2}$

T = Temperature, Kelvin

ρ_{H2O} = density of H_2O, g/cc

All other values are experimentally determined constants (Manning, 1994).

H_2O-SiO_2-CO_2-NaCl mixture:

$$\log K = A(T) + B(T) \times \log (18.0152/V^*_{H2O}) + 2 \log x_{H2O}$$

Where:

$\log K = \log m_{SiO2}$

$A(T)$ = First polynomial term of Manning's (1994) equation for the relevant temperature.

$B(T)$ = Second polynomial term of Manning's (1994) equation for the relevant temperature.

V^*_{H2O} = Effective partial molar volume, H_2O

x_{H2O} = mole fraction, H_2O

Experimentally determined by Akinfiev and Diamond (2009).

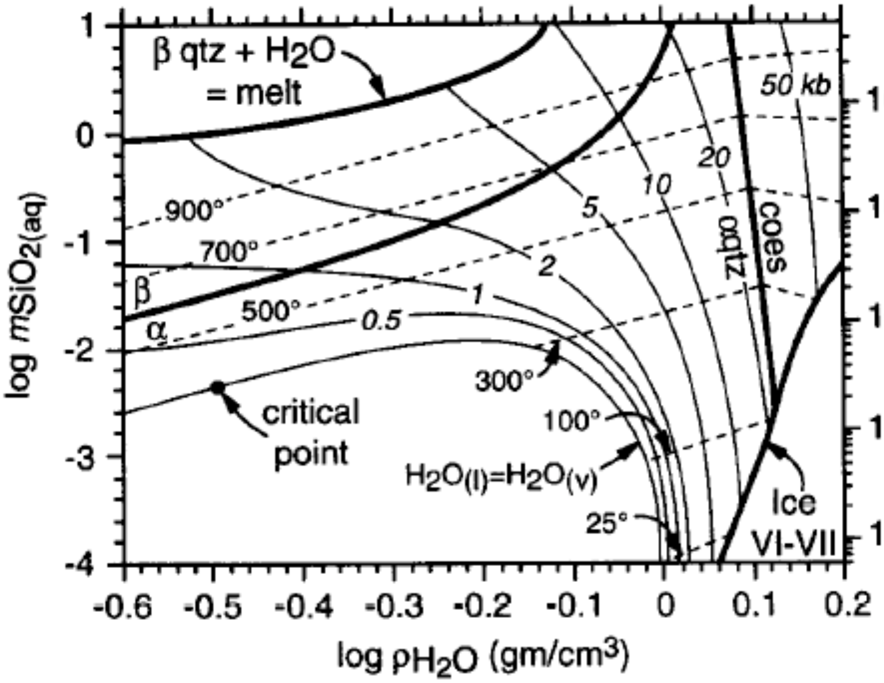

Figure E1. Phase diagram for SiO_2-H_2O, for determining quartz solubility. The y-axes are used in conjunction to obtain the kg of H_2O recorded per kg quartz vein as discussed in the text. After Manning (1994).

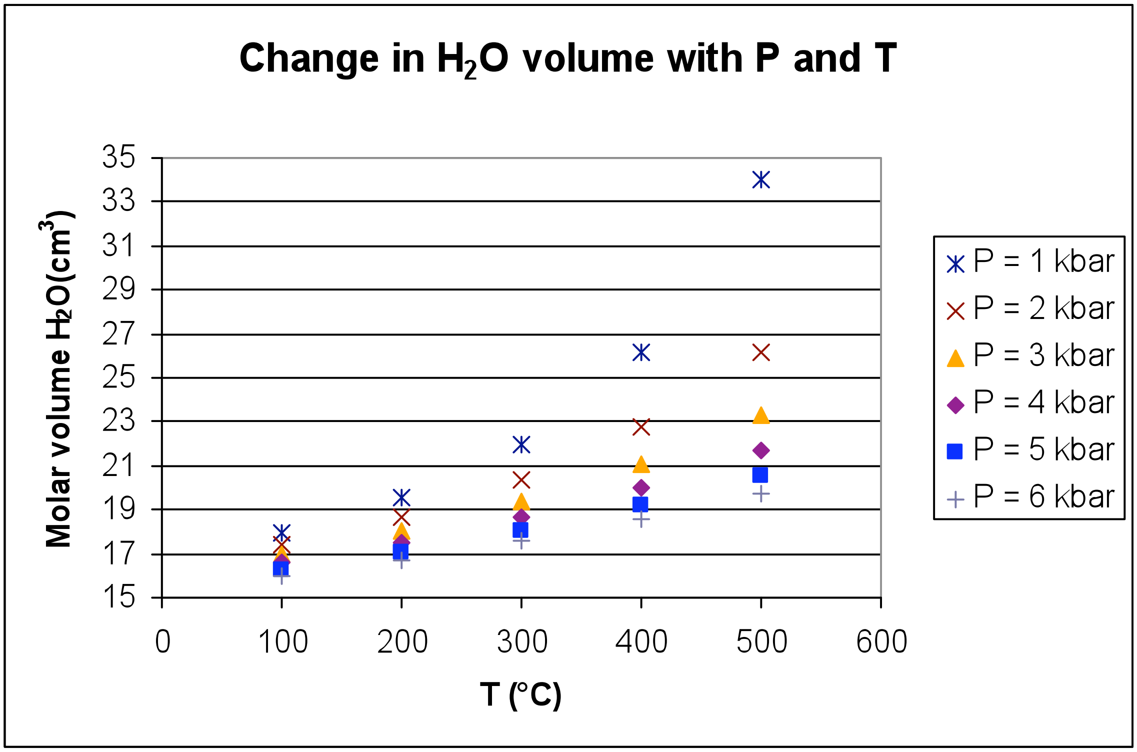

Figure E2. Changes in H_2O molar volume due to pressure and temperature changes. Changes in H_2O molar volume also equal changes in density, which is used in the above equations. In this graph, the pressures most relevant to Olympic Peninsula rocks are solid symbols. Recall that temperature conditions reached ~150–290°C. Data from Halbach and Chatterjee (1982).